Integrated Nanoemitters on Glass-based Waveguides by Photopolymerization

Xiaolun Xu

Thèse
de doctorat
de l'UTT

Xiaolun XU

Integrated Nanoemitters on Glass-based Waveguides by Photopolymerization

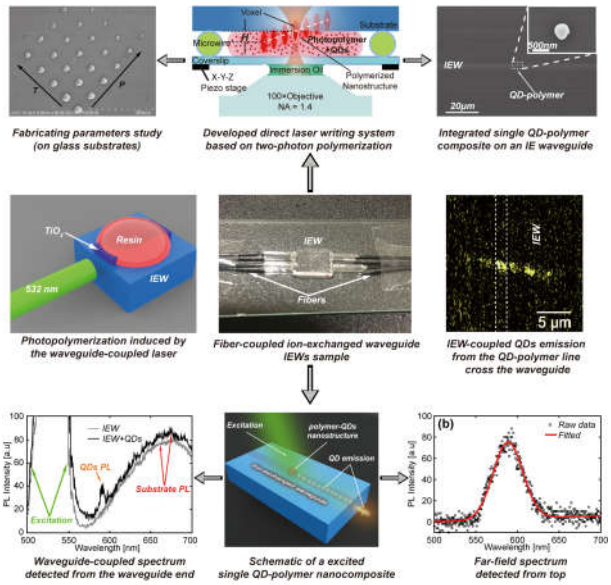

Champ disciplinaire :
Sciences pour l'Ingénieur

2020TROY0026

Année 2020

utt
UNIVERSITÉ DE TECHNOLOGIE
TROYES

THESE

pour l'obtention du grade de

DOCTEUR
de l'UNIVERSITE DE TECHNOLOGIE DE TROYES

EN SCIENCES POUR L'INGENIEUR

Spécialité : MATERIAUX, MECANIQUE, OPTIQUE, NANOTECHNOLOGIE

présentée et soutenue par

Xiaolun XU

le 15 décembre 2020

Integrated Nanoemitters on Glass-based Waveguides by Photopolymerization

JURY

Mme Delphine MARRIS-MORINI	PROFESSEURE DES UNIVERSITES	Présidente
Mme Stéphanie BUIL	MAITRE DE CONFERENCES - HDR	Rapporteure
M. Ngoc Diep LAI	MAITRE DE CONFERENCES - HDR	Rapporteur
M. Renaud BACHELOT	PROFESSEUR DES UNIVERSITES	Examinateur

Personnalités invitées

M. Sylvain BLAIZE	MAITRE DE CONFERENCES	Directeur de thèse
M. Christophe COUTEAU	PROFESSEUR ASSOCIE UTT - HDR	Directeur de thèse

General introduction

Nanoemitters and nanosources of light are crucial elements for many photonic devices for application in biology imaging, optical lasing, sensing and quantum technologies [1–4]. Luminescent colloidal semiconductor quantum dots (QDs) have already proven to be promising solid-state nanoemitters in the fields of nanophotonics and quantum optics [5–7]. For the practical realization of scalable photonic devices, one of the key requirements is the ability to integrate QDs onto specific optical chip locations. Many approaches have been explored, including electron beam lithography (EBL) [8,9], optical trapping [10,11], and atomic force microscopy (AFM) transfer methods [12,13]. However, these methods have some limitations such as complicated operations, high manufacturing costs, and multiple fabricating steps.

Spatially controlled photopolymerization represents an interesting tool for the micro and nanopatterning of polymeric structures [14]. Direct laser writing (DLW) based on two-photon polymerization (TPP) has been employed for producing three-dimensional (3D) arbitrary microscale and even nanoscale polymeric structures in a fast and simple manner with high positioning and laser writing accuracy [15]. Recently, embedding semiconductor quantum dots into a photopolymer host matrix has been exploited to produce QD-polymer composites by photo-polymerization, which joins the active light-emitting property of QDs together with the technological feasibilities of the polymer matrix [26–29]. however, integrating these QD-polymer nanocomposites onto the pre-existing or preselected waveguides is still a challenge.

This thesis aims to explore the feasibility of integrating nanoemitters based on QD-polymer nanocomposites onto the glass-based optical waveguides. The final goal of the

project is to realization of integrated nanoemitters on hybrid plasmonic-photonic waveguides. My doctoral work is mainly focused on the preliminary exploration including building the experimental setup, optimizing the polymerization process, characterizing the polymerized nanoemitters and analysing the QD-waveguides coupling.

This work was realised in collaboration with the Teem Photonics Company, and was funded by H2020 Marie Skłodowska-Curie Actions Innovative Training Networks (MSCA-ITN) LIMQUET (Light-Matter Interfaces for Quantum Enhanced Technology, 765075); FEDER (Fonds Européen de développement régional); Agence Nationale de la Recherche (ANR-17-EURE-0002); China Scholarship Council (CSC).

This thesis is structured as follows:

Chapter 1: We firstly review the existing main integrating method for creating nanoemitters onto/into photonic devices. Secondly, we describe the QDs contained polymer matrix and the mechanism of photopolymerization. Thirdly, we introduce the several examples of plasmon-based photopolymerization which were realised by our research group. Finally, we propose the platform of ion-exchanged waveguides (IEWs) where we desire to integrate the nanoemitters based on QD-polymer composites.

Chapter 2: We characterized the light propagation of IEWs and optimize the stability of the experimental set-up for photopolymerization. We describe two main experiments of evanescent wave induced photopolymerization for IEW substrates with and without a top-deposited dielectric layer (TiO_2). We present the results of fabricated QD-polymer composite and PL measurements.

Chapter 3: In this chapter, we present a developed direct laser writing technique based on two photon polymerization method for integrating the QD-polymer nanocomposites on IEWs. We describe the laser printing parameters study for showing the ability of controlling the sizes and positions of QD-polymer composites. We show an example of an integrated single QD-polymer nanocomposite on an IEW substrate,

and the light coupling between QDs and the waveguide was measured by our home-built PL measurement setup.

Chapter 4: This chapter presents additional experiments for further developments in the future regarding the integrated nanoemitters on more elaborate IEW-based hybrid substrates. We describe several methods for solving the problems such as the noise fluorescence from the IEWs and low coupling efficiency from QDs to waveguides. We present the preliminary exploration results about integrating QDs attached polymeric structures on IEWs and the photopolymerization induce by the gold antennas on glass substrates.

At the end, a general conclusion and perspectives are given.

Acknowledgements

First of all, I would like to thank to all the members of my defence committee for taking the time to review my manuscript and for their constructive remarks and comments on my PhD work.

To my supervisors Dr Sylvain Blaize and Dr Christophe Couteau for their delighting guidance, encouragements and friendship throughout the 4 year of PhD working in Laboratoire Lumière, nanomatériaux et nanotechnologies of the University of Technology of Troyes (UTT). I am extremely grateful for having been given the great opportunities to attend international conferences and workshops which inspired my work and broadened my perspectives.

I would like to thank Dr Renaud Bachelot, Dr Safi Jradi, Dr Josslyn Beltran Madrigal and Dr Tiziana Ritacco for their help and insightful suggestions during my PhD works. I thank the PhD students (Ge Dandan, Chen Hongshi, Mackrine Nahra, Muhammad Ahmed), Dr Ali Issa, Dr Aurélie Broussier, Dr Ying Peng, Dr Stefano Pierini, Dr Giuseppe Emanuele Lio and other members in our research group for the help during my experiments and the knowledge sharing.

I would like also thank Régis Deturche, Jéremie Béal and Sergei Kostcheev for their technical assistance that helped me learn important skills during my experiments. Thanks to all my Chinese colleges in L2n for their encouragement and friendships. I would particularly like to thank Dr Wang Binbin, Dr Zhang feifei, Dr Wang Shijian for being with me discussion and helping me. Thanks to all the members of the Laboratoire Lumière, nanomatériaux et nanotechnologies (L2n) of the UTT for their great help.

Thanks to my family for all your love. To my father and mother for their endless understanding and support. To my sister and my nephew for their laughing. Thanks to my love for all the time we have experienced together in this small and beautiful city.

Finally, I would like to thank this experience of studying in Troyes, France. I love this city and country. Allez France!

Table of contents

Chapter 1 Integrated nano-emitters on glass-based waveguides

This chapter firstly reviews the existing main methods for integrating nanoemitters onto/into photonics devices (section 1.1). Secondly, considering the complexity, time consuming and the feasibility of these methods, we describe our proposed method which a chemical method based on photopolymerization. Section 1.2 then introduces the basic concepts of photopolymerization based on one-photon absorption (OPA) and two-photon absorption (TPA), which are the main principles used for the experiments in Chapter 2 and Chapter 3, respectively. By mixing luminescent semiconductor colloidal nanocrystals with photopolymer solutions, nanocrystals can be integrated into microscale/nanoscale polymeric structures during the photopolymerization process. These composites can then be used as nanoemitters for different photonic channels and circuits. In our case, we work with glass-based ion-exchanged waveguides (IEWs), presented in section 1.3.3. Finally, we stress the objective of our research which is integrating nanoemitters onto IEWs-based photonic waveguides and realising light nano-sources.

1.1 State of the art and challenges

Colloidal nanostructures such as semiconductor nanocrystals and quantum dots with precisely controlled sizes in the range of 1 to 50 nm are promising building blocks for photonic devices. This promise will not be fulfilled, however, unless methods of integrating and positioning these emitters can be developed and optimized. In the last decade or so, the integration of single emitters into/onto photonic chips has gained a lot

of attention. Reliable fabrication methods require the controlled deposition of nanoparticles/nanoemitters on arbitrary photonic substrates with high precision. Many approaches have been explored, including electron beam lithography [1–3], optical force trap [4–7], interfacial capillary forces [8–11], epitaxial growth [12–16] and pick-and-place techniques [17,18]. We now quickly review these various methods.

e-beam lithography:

The most popular method used in this context is electron beam lithography (EBL) which utilizes a high-energy focused electron beam, to generate contrast on photo-resist, such as PMMA, thus forming patterns as small as several tens of nanometers. Two different strategies are used for introducing nanocrystals into photonic structures. The first one is to spin-coat a layer of nanocrystals in advance, and then create patterns near the preselected nanocrystals, as shown in **Figure 1-1**(a). This method is usually used for studying the interaction between nanocrystals with metal nanocubes, nanospheres, nanodisks and bow-tie nanostructures [6,19–23]. However, in this situation, the distribution of nanocrystals on the substrate surface cannot be controlled, and the key challenge is to address the proper nanocrystals which can be quite time-consuming. Besides, during the second step of the fabrication, the high-energy focused electron beam may damage the nanocrystals resulting in less the fluorescence.

The second option is to drop-cast nanocrystals on a prepared pattern fabricated by EBL method which is described in **Figure 1-1**(b). By combining the ligand exchange method, Mentzel *et al.*, created a thin film of nanocrystals with fine feature sizes of 30 nm or so. Xie *et al.* used EBL on ZEP 520A resist, also achieving nanoscale (≈ 30 nm) patterns and single-dot positioning [24,25]. Both of these examples only realised a layer of nanocrystals on a flat substrate. However, for most photonic structures, additional EBL processes need to be conducted in order to place nanocrystals at desired positions which increases the operating complexity of the method. In contrast, focused ion beam (FIB) milling is also not suitable to directly pattern QD films, as severe damages on the

QDs by the focused ion beam can yield to a photoluminescence reduction up to 71% [26].

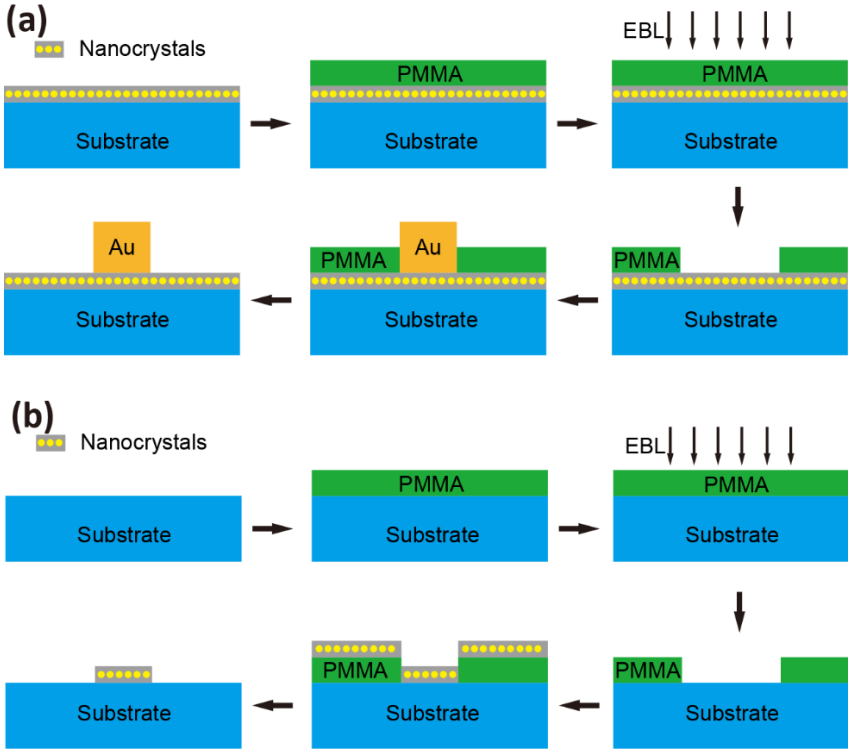

Figure 1-1 The overview of the process for fabricating nanoscale patterns of nanocrystals by electron beam lithography. Nanocrystals deposition before (a) and after (b) the creation of patterns.

Optical force trap:

Optical forces have been widely used for trapping and manipulating nanoparticles. In 1986, Ashkin *et al.* used a focused laser beam to realize the stable trapping of nanoparticles, even down to single molecules. This technique is called optical tweezers [6]. The basic principle can be explained by the conservation of momentum. When in contact with a strong laser field, particles absorb or scatter photons and then impart momentum. This results in particles being attracted along the gradient of the strongest electric optical field. **Figure 1-2**(a) shows an example in which two optical fibers are used to trap and rotate a human muscle cell. This technique is called dual fiber 'tweezers' [27]. When combined with plasmonic structures (such as nanoscale antennas and plasmonic cavities) the near-filed optical forces arising from localized

surface plasmons can be used to attract and manipulate nanoparticles toward the hotspots with lower power than what is used for free space optical trapping. As shown in an example in **Figure 1-2**(b), a 30 nm polystyrene nanoparticle is trapped in a 10 nm gap resonant coaxial nanoaperture [15]. However, as smaller particles require higher confined optical fields for trapping efficiently, such tight 'hotspot' can create a large power density and thus damage the trapped nanoparticles, especially for luminescent nanoemitters, such as quantum dots due to quenching from the nearby metal. In order to avoid this problem, Huang *et al.* coated QDs with silica shell to mitigate quenching and increase the trapping efficiency [5].

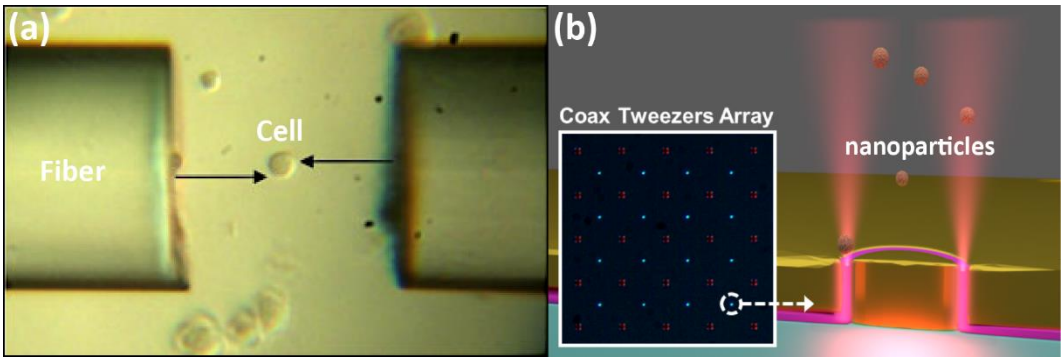

Figure 1-2 (a) Human muscle cell captured by two optical fibers; (b) Optical trapping of nanoparticles with resonant nano-apertures of 10 nm gap. (Image taken from [15,27])

Interfacial capillary forces:

The interfacial capillary interaction in a solution has been demonstrated to play an important role in controlling micrometer or millimetre 2D or 3D particles. However, for nanoparticles with diameter below 50 nm and even 10 nm, the capillary force is not an efficient approach to drive them because the capillary interaction strength decreases with decreasing object dimension and the thermal effects become more significant. Cui *et al.* used an approach which is called three phase vapor-suspension-substrate contact line to drive quantum dots [8]. The basic process is shown in **Figure 1-3**(a). A flat substrate patterned with a hole fabricated by electron beam lithography is inserted

vertically into the solution dispersed with quantum dots. The evaporation of the solvent leads to the contact line moving slowly across the substrate surface. When the solution film thickness on the substrate is less than the diameter of the nanoparticles, the interfacial capillary force deforms and drives the nanoparticles towards the hole. **Figure 1-3**(b) shows the captured nanoparticles inside the gap of nanoatennas. This method can be also applied to other types of nanocavities with narrow gaps and metal nanoparticles. An example is shown in **Figure 1-3**(c) where Au nanoparticles are forced into the gap of prefabricated electrode pairs.

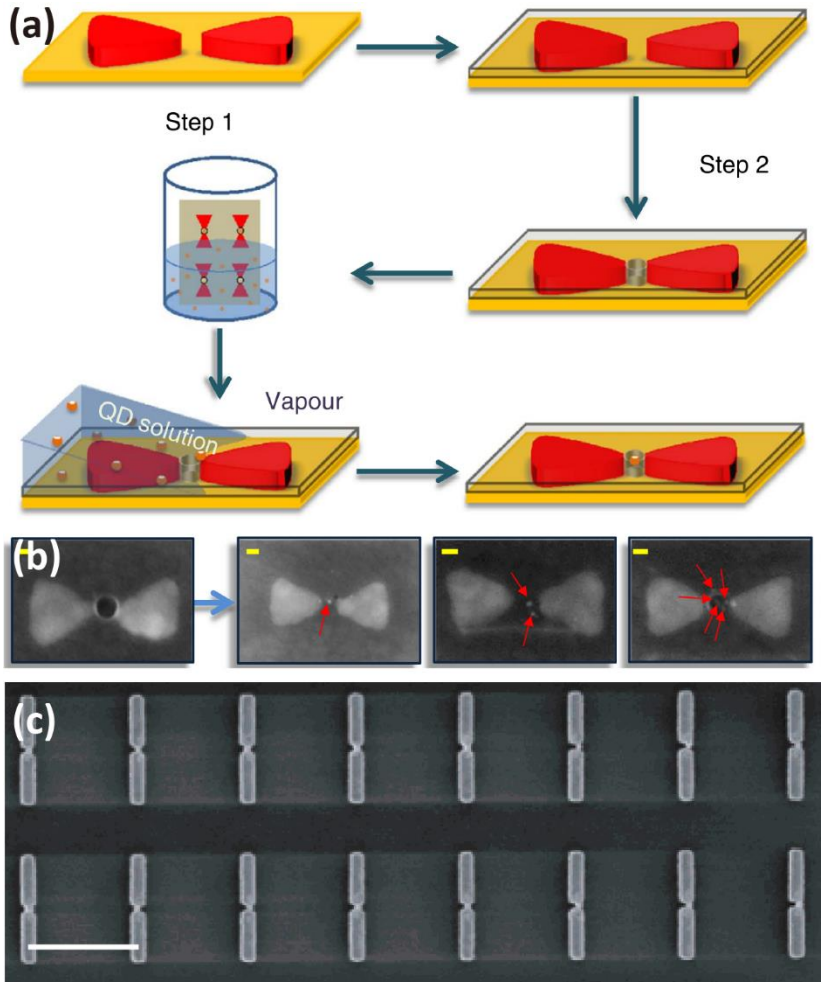

Figure 1-3 (a) Schematic illustrating the interfacial capillary force mechanism at the vapour-suspension-substrate three phase contact line; (b) Scanning electron microscope images of bowties with one, two, and multiple quantum dots in their gaps, the positions of the QDs are marked with red arrows. Scale bar: (b) 20 nm, (c) 1 μm. (Image taken from [8,11])

Epitaxial growth:

Epitaxial growth is a well-known method in the semiconductor industry, where semiconductor films are grown epitaxially on substrate wafers. The epitaxial growth for quantum dot preparation has been demonstrated where both lattice matched and lattice mismatched materials can be used for QD fabrication [15]. Combined with electron beam lithography and luminescence spectroscopy, one can deterministically create hybrid integrated quantum photonic devices containing preselected individual quantum dots. Davanco *et al.* fabricated a hybrid on-chip quantum photonic circuit with single quantum dots by heterogeneous integrating method based on epitaxial growth, as shown in **Figure 1-4**(a) and (b). Although this method has high fabricating precision which is helpful for controlling the position at nanoscale, the complicated manufacturing process remains a big issue in terms of integration. Besides, a single quantum dot embedded inside a circuit still needs to be preselected, which limits the application for many types of quantum photonic devices. As mentioned above, the electron beam might damage the QDs during the waveguide fabricating process.

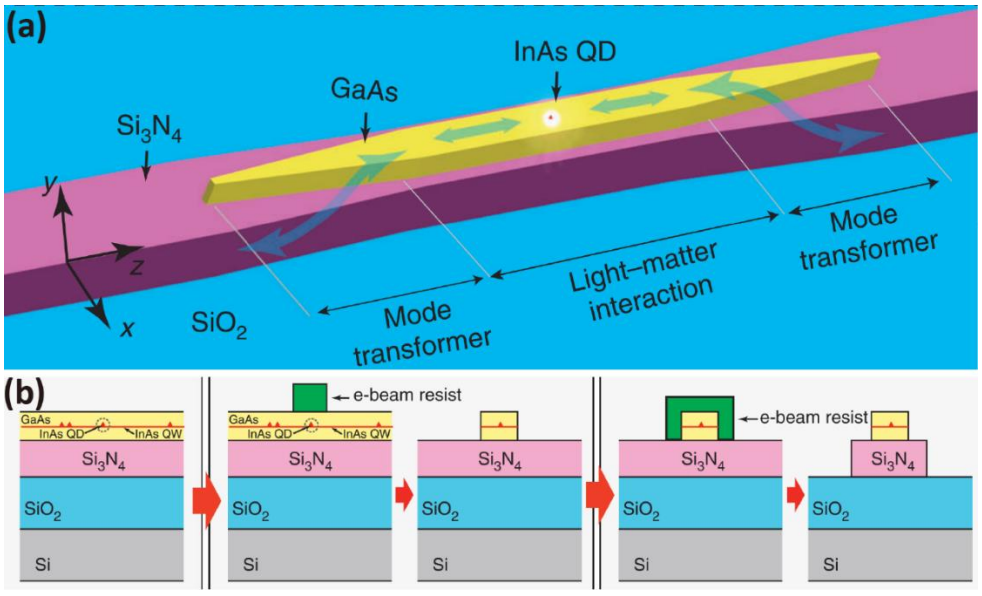

Figure 1-4 (a) Conceptual quantum photonic circuit containing a single quantum dot integrated by epitaxial growth; (b) Schematic of the basic

fabricating process of an GaAs waveguide containing self-assembled InAs QDs. (Image taken from [16])

Pick-and-place technique:

Junno *et al.* demonstrated for the first time the controlled driving of nanometer-sized objects on a surface through the AFM tip due to electrostatic forces [28]. A sketch of the basic pick-and-place procedure is given in **Figure 1-5**(a). Picking up metallic nanoparticles is also achieved after chemical treatment of the AFM tip [29]. In principle, it is possible to extend it to nanocrystals as it only relies on surface adhesion. For example, Kim *et al.* integrated a single quantum emitter on a silicon photonic chip by picking a tapered structure containing quantum dots on top of a Si waveguide, shown in **Figure 1-5**(b) [18]. Although this method can be applied for picking and placing arbitrary particles with nanoscale precision, there are still several disadvantages. The experimental setup usually consists of a scanning electron microscope which makes it impossible to apply to epitaxial quantum dots, one can observe the surface by the AFM tip, which makes the whole process time consuming. In contrast to the picking up process, the placing is not always successful which limits its applications on complex surfaces with sharp edges [30].

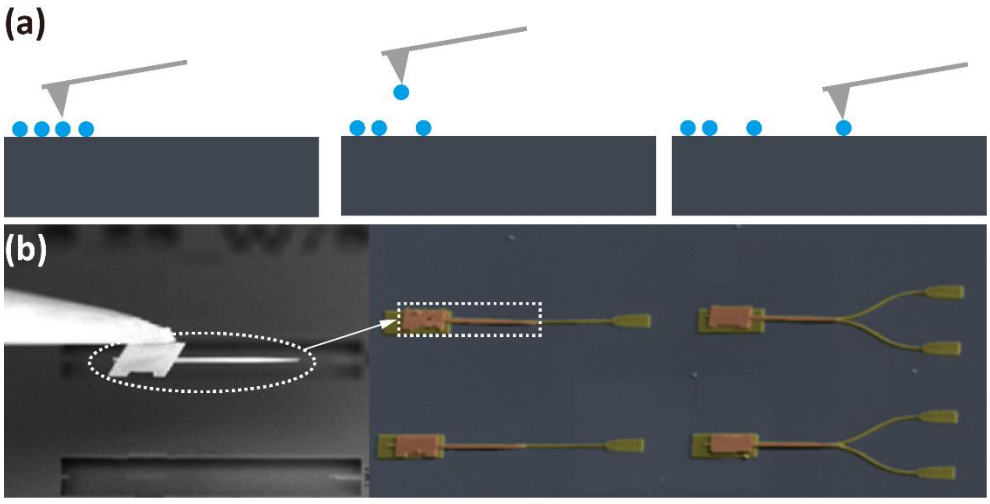

Figure 1-5 (a) Scheme of the nanoparticle pick-and-place procedure, Left: the AFM tip is scanned across the focal region of the microscope to identify the chosen nanoparticle; Middle: the nanoparticle sticks to the tip;

Right: the nanoparticle is positioned at the desired position; (b) Pick-and-place procedure of the fabricated tapered structure containing InAs quantum dots. (Image taken from [18])

Electrohydrodynamic (EHD) printing:

Unlike those fabrication techniques discussed above, this technique uses the solution processability of QDs by spin-coating of thin solid films. Recently, a similar solution-based high resolution printing approach, termed electrohydrodynamic (EHD) or NanoDrip printing has been developed [31,32]. **Figure 1-6**(a) shows the schematic of an EHD setup. The colloidal quantum dots dispersion is printed from the apex of the nozzle with a controlled bias voltage [33]. By controlling printing parameters such as bias voltage, scanning speed of the nozzle, the volume and fluorescence intensity could be manipulated [32]. The main difference with ink-jet printing technique with typical resolutions of 10 - 50 μm [34,35], EHD uses a jet with a much smaller orifice (about 1-5 μm) and the DC bias between the nozzle and the substrate surface generates droplets 10 times smaller than the opening. SEM and fluorescence images of printed spots confirmed sub-micro resolution, ranging from 200 to 100 nm, as shown in **Figure 1-6**(b) and (c). This method is useful to place QDs on pre-existing nanostructures with high precision. Kress *et al.* transferred QDs on top of a golden wedge waveguide, coupling the integrated QDs with plasmonic resonators as shown in **Figure 1-6**(d-f) [36].

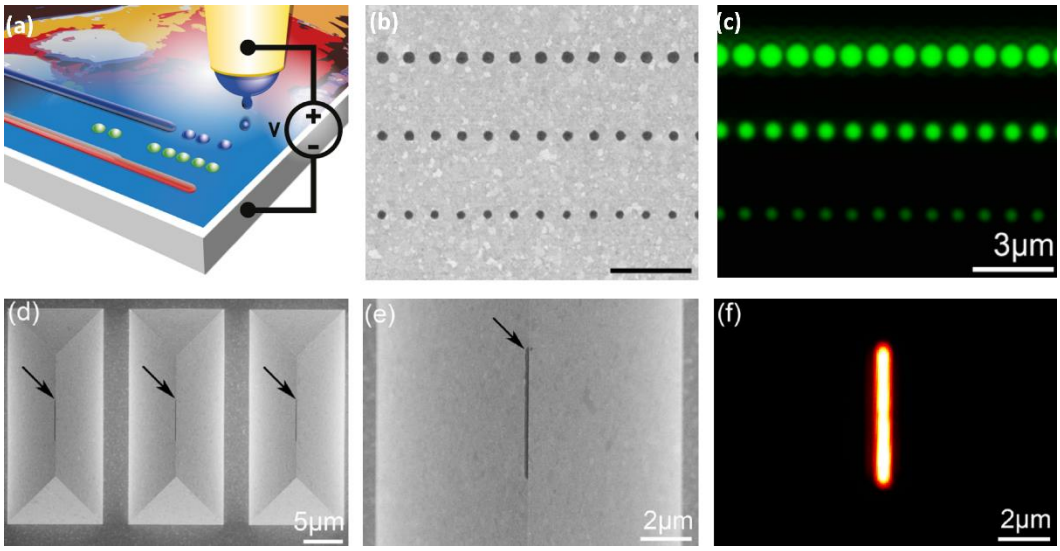

Figure 1-6 (a) Schematic of EHD printing setup; (b, c) Fluorescence and electron micrographs of printed spots; (d-f) SEM and false-color fluorescence images of the printed quantum dot lines along the apex of the Au wedges. (Image taken from [32,33])

1.2 Basic concept of photopolymerization

Photopolymerization is a special form of free-radical polymerization where light is used to initiate polymerization. By the term photopolymerization we mean the initiation by light of a chain polymerization process. In the more general sense, photopolymerization implies the increase of molecular weight caused by light and includes the photocrosslinking of pre-existing macromolecules. This method has many advantages over conventional fabrication methods in terms of less energy consumption, reduced waste, higher productivity (fast cure) and lower reaction temperature.

1.2.1 Principle of photopolymerization

Photopolymers or light-activated resin are light sensitive polymer materials which change their properties when exposed to light. Usually photopolymers are kept in a liquid state for general use and only curable with light sources (UV laser, lamp, light-emitting diodes (LEDs) etc.). The light from these sources initiate chemical reactions which modifies their chemical and mechanical properties, these changes are often manifested structurally, finally change their state from liquid substance to solid

substances. Only the area exposed to UV-light hardens, whereas unexposed parts will still remain like liquid [37,38]. Photopolymers are eco-friendly and therefore popular in recent history since they can work without any volatile solvent in most of the industrial process.

While a photopolymer may include a number of ingredients, such as plasticizers and colorants, the key elements necessary for the photo-polymerization process are photoinitiators, oligomers and/or monomers. Other additives may also be used to change the unique properties of each photopolymer.

- Oligomers/Binders: The material is a molecular complex of chemicals that consists of a few repeating units, in contrast to a polymer, where the number of monomers is, in principle, infinite. The oligomers are a major determinant of the properties of the photopolymer. For instance, they influence how durable and heat resistant it is. Oligomers make up for more than half of the photopolymer's weight.

- Monomers: These are made up of tinier molecules that can undergo polymerization thereby contributing constitutional units to the essential structure of a macromolecule. Large numbers of monomers combine to form polymers in a process called polymerization. Monomers make about a tenth of the weight of the final product. But, they can be as much as 40 % of the total weight. In our work, pentaerythritol triacrylate (PETA) is the main monomer used as the polymer matrix for nanocomposites due to its high optical transparency, chemical inertness, and mechanical flexibility. And the synthesis of QDs and their dispersion in PETA monomer were reported [39,40]. In addition, the PETA contains irradiation time are compatible with the diffusion parameters of Oxygen within the acrylate matrix [41].

- Photoinitiators: Photoinitiators are tiny molecules that create reactive species (free radicals, cations or anions) when exposed to radiation (UV or visible). Parts of reactive species help binders and monomers to react. The reaction links them, thus forming the final polymeric structures. All photoinitiators work at specific light wavelengths, some of them will only work under UV light. methyl diethanolamine

(MDEA) is a popular co-initiator used in polymer formulations and used in this project [42]. Other photoinitiators will work with visible light. They tend to make up a minuscule percentage of the final product. Irgacure819 is another photoinitiator used in our works which is sensitive in UV range (commercialized by BASF). As a reference, the formulation mixed with PETA and Irgacure819 has been demonstrated to be suitable for nanofabrication [43]. Besides, in order to increase the sensitivity of the polymer on green light, we can also put the EosinY into the solutions. EosinY is a xanthenic dye photoinitiator. Due to the presence of EosinY, the photopolymer is particularly sensitive to visible wavelength (spectral range from 450 to 550 nm), and thus it fits well with the the green laser in our laser coupling system (532 nm), more details are described in Chapter 2.

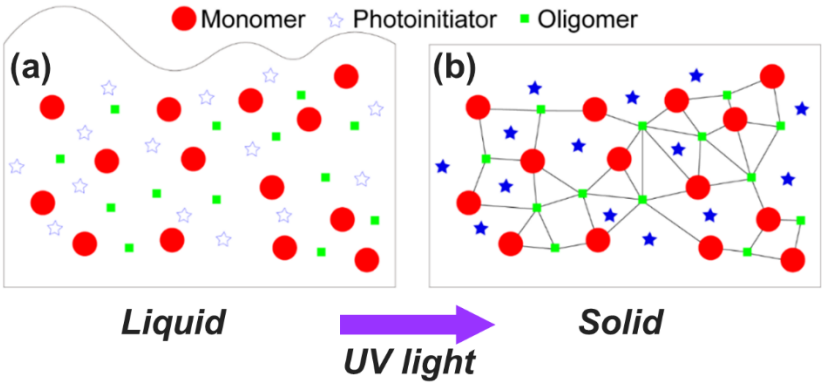

Figure 1-7 (a) Photopolymer solution containing monomer, photoinitiator and oligomer; (b) UV energy hits the photoinitiator molecules which become excited, passing energy to other components. This stimulates the crosslinking process between molecules and convert exposure polymer from liquid to solid state. (Image reproduced from Wikipedia)

The photo-polymerization reaction is initiated through a free-radical process. Two components are involved in the radical formation : the dye that absorbs the visible radiation and the amine that can be oxidized by the triplet state of the dye. Once the radicals trigger the crosslinking mechanism, the monomers polymerize, developing into a three dimensional network. **Figure 1-7** show the schematic of the principle of photopolymerization. One specific characteristics of this formulation is related to the

existence of a threshould of polymerization that allows a sharp control of the polymerized area. This effect is mainly due to the well-known effect of free-radical reaction quenching by oxygen. Finally, the unreacted monomer are eliminated by rinsing with ethanol and the exposured part remains.

1.2.2 Incorporation of nanocrystals into photopolymer

Polymers are not only attractive by their technological feasibilities, but also for their optical properties, because they are highly transparent at wavelengths longer than 400 nm and their refractive index is relatively high (~ 1.5) [44]. Since polymers are solution process materials, they can easily act as matrices of different compounds of nanoparticles to provide additional properties [45]. It has already been demonstrated the use polymers as a matrix for metal nanoparticles and organic dyes, resulting in a broad range of applications like optical amplification, photovoltaics, sensing and plasmonics [46–51].

Recently, Polymer−QDs solution with excellent optical properties, chemical inertness has been demonstrated via simple mixing of photosensitive polymer and QDs components with reasonable proportion [52–54]. Incorporation of colloidal semiconductor quantum dots in polymers has emerged as an alternatively technology to form nanocomposites. In this way, QDs could be simply introduced into solid state devices after the polymeric pattern is created. And a polymer nanocomposites containing semiconductor nanocrystals results a flexible material which joins the active properties of the nanocrystals together with the technological feasibilities of the polymer matrices [45,55]. It has been demonstrated that the embedded QDs have similar optical properties as free QDs [56]. Therefore, A QD-polymer nanocomposite is prospective material to be used in future integrated photonic optical devices.

1.2.3 Two-photon polymerization

Single/One-photon absorption (SPA or OPA) is a linear absorption process whereby one photon excites an atom, ion or molecule from a lower energy level to a higher energy level. This process is usually applied in macroscale stereolithography 3D

printers [57]. The probability of the initiator molecule to absorb one photon is pretty high, meaning that polymerization would occur not only at the laser focus point but also around that point, where the laser intensity is lower. This undesired polymerization out of focus decreases the printing resolution.

Two-photon polymerization (TPP) was firstly proposed by S. Maruo in 1997, and in which the energy for exciting the electron from the ground state to the excited state is provided by two photons with approximately half the energy [58]. This non-linear optical effect is called two-photon absorption (TPA), represents the rule behind the TPP method. Since the laser energy scales inversely with the wavelength according to Planck's law, half the energy means twice the wavelength of the photon in single photon absorption. This lead to several distinct benefits. The long wavelengths used for two photon excitation are less damaging and penetrate more deeply into the object/photoresin than those used in single photon excitation. And the TPA is only achieved near the focus spot, this leads to little reaction to the regions above and below the focal plane. **Figure 1-8** show the comparison of the excitation mechnisms of OPA and TPA.

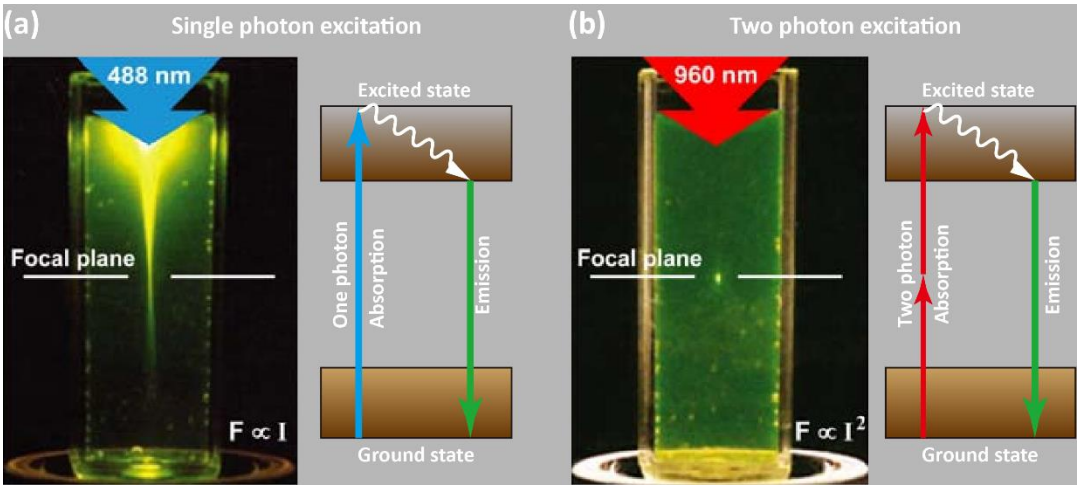

Figure 1-8 Comparison of excitation profiles of (a) single photon and two photon (b), a 488 nm laser used in SPA while a 960 nm laser used in TPA. For exposure areas, additional light emanates from above and below the focal plane in (a) while in TPA, the laser beam is focused in a spot in the focal plane. In Jablonski diagrams, only single photon is used to excite the

electron in (a) while two photons with twice of the wavelength are absorbed in (b). (Image reproduced from [59])

1.3 Hybrid plasmonic nanoemitters

Integrating the nanoemitters which are based on QDs-contained polymeric structures onto different plasmonic structures were also proposed by our group. We actually desire applying the nanoemitters based on QDs-polymer on different systems. Here, we show two related works which were conducted on silver nanowires (done by PhD student Aurelie Broussier, [60]) and plasmonic nanocubes (done by PhD student Dandan GE, [61]), respectively. Next, we introduce a previous work about the hybrid photonic-plasmonic system based on ion-exchanged waveguide, which is done by a former PhD student Josslyn Beltran MADRIGAL in our group.

1.3.1 Polymerized nanoemitters coupled with silver nanowires

Nanoplasmonic is an emerging research fields. One of the promising research topic is the controlling of energy transfer between nanoemitters and surface plasmons (SPs) [62,63]. SPs are surface electromagnetic waves that propagate in a direction parallel to the metal/dielectric interface [64]. Silver nanowires (Ag-NWs) are metal nanostructures which support propagative SPs that can be launched or detected at the nanowire's extremities [65,66]. Although QDs/Ag nanowires coupling has already been reported, most of them used spin-coating as a depositing method to obtain a layer of QDs onto the plasmonic system [67–71]. Spin-coating is a simple and fast way which does not permit any QDs position control. It should be emphasized the position of the QDs has to be accurately controlled in order to improve the coupling between QDs and nanowires and obtain efficient energy transfer. Here, we use an even faster and simpler way for integrating QDs near the plasmonic structures with the position highly controlled. Our method is based on direct laser writing technique based on TPP, which is described in detail in Chapter 3. In this section, we show our results about the coupling between CdSe/ZnS QDs and propagating SPs supported by silver nanowires

and the scattering of the surface waves at the nanowire ends. The schematic of hybrid nanoplasmonic system based on QDs and a silver nanowire is shown in **Figure 1-9**.

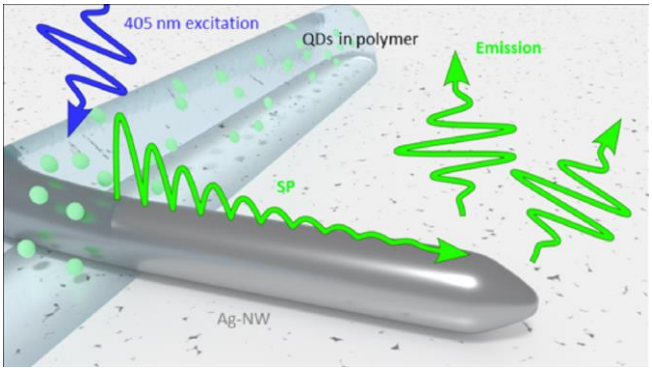

Figure 1-9 conceptual schematic of the coupling between quantum dots contained polymeric structure and surface plasmons (SPs) supported by a silver nanowires (Ag-NW). (Image taken from [60])

The Ag-NWs (Sigma-Aldrich, ref. 739448) were fabricated in an isopropanol solution and have a length ranging from 5 to 50 μm. This solution of silver nanowires was spin coated on a clean glass coverslip which could be mounted on the laser printing system. **Figure 1-10**(a) shows a typical SEM image of a silver nanowire which has a diameter in the 130-160 nm range. Chemically grown monocrystalline Ag-NWs are characterized by smooth defect-free surfaces and faceted ends, as shown in the inset (i) of **Figure 1-10**(a). By focusing a 514 nm laser on the Ag-NW end, SPs could be excited through scattering, generation of a large range of high in-plane wave vectors that match the SP dispersion function at this wavelength. And the SPs has the polarization selectivity, shown in the inset (ii) and (iii) in **Figure 1-10**(a). SPs can be excited for an incident polarization parallel to the nanowire axis, but not for the incident polarization perpendicular to the axis. **Figure 1-10**(b) shows the SEM image of a coupled system consisting of a silver nanowire and a laser printed polymer line. The photopolymer formulation was made of 1% Irgacure 819 (IRG 819) and 99% QDs-grafted pentaerythritol triacrylate (PETA). CdSe/ZnS QDs with an emission wavelength of 510 nm were used. Here, as shown in the inset of **Figure 1-10**(b), the width of this polymer

line is about 280 nm, but the widths of polymer lines can be controlled down to 70 nm by decreasing the printing laser energy during the TPP process.

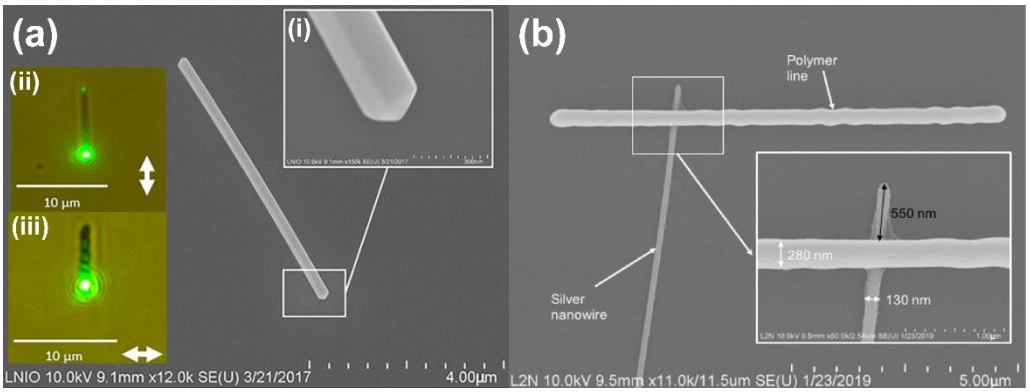

Figure 1-10 (a) SEM image of a typical silver nanowire on a Si substrate. Inset: Zoom-in view of the detail at the nanowire extremity; (b) SEM image of the nanostructure consisting of a silver nanowire coupled with QD-contained polymeric line printed by laser writing technique. Inset: Zoom-in view of the detail at the crossing position between the Ag-NW and the polymer line. (Image reproduced from [60])

QDs were used to launch SPs on silver nanowires. **Figure 1-11**(a) shows different local PL spectra recorded at different positions while the 405 nm excitation laser was always focused at the crossing point between the NW and the polymer line. PL spectra of NW-coupled QDs emission (510 nm) was detected only at the nanowire end, shown with the blue spectra. No PL signals could be detected from the position A and B outside of the nanowire body. In addition, the calculated effective SP wavelength in the case of 514 nm excitation is about 450 nm, which is far away from the 405 nm. In conclusion, only QD PL emission can be the resource of SP excitation.

Ag-NW enable the SPs propagation along the nanowire, making possible long-distance energy transfer between the nanoemitter and a specific nanowire point of interest. The energy transfer rate between the cross point and the nanowire end is determined by SP excitation efficiency (EE) at the cross point and SP propagation decay. The orientation and the positions of QD dipoles are supposed to be random. The EE depends on three main parameters: QD dipole orientations, the distance from the

nanowire surface and the spectral overlap between the SP modes and the QDs emission [72]. Here, we assumed that the EE is constant whatever the position of the cross point. Therefore, due to the SP propagation loss, the PL intensity at the nanowire end should exponentially decreases as *d* increases. In order to prove that, several polymer lines were made on several nanowires in order to carry out a parametric study of the effect of the *d*, the distance between the QDs location and the nanowire end. **Figure 1-11**(b) shows a clear relationship between the measured PL intensity with the *d*, showing that it is possible to control the PL intensity at the nanowire end by controlling the position of the nanoemitters based on QD-polymer structures.

The nanowire coupled with light emitting QDs, providing a promising and integrated platform for optical information propagation and processing. The results shown above also show the possibility of the direct laser writing technique based on TPP for integrating nanoemitters onto photonic chips with complex nanostructures. This work also provides valuable QDs integrating experience for the application on glass-based waveguides.

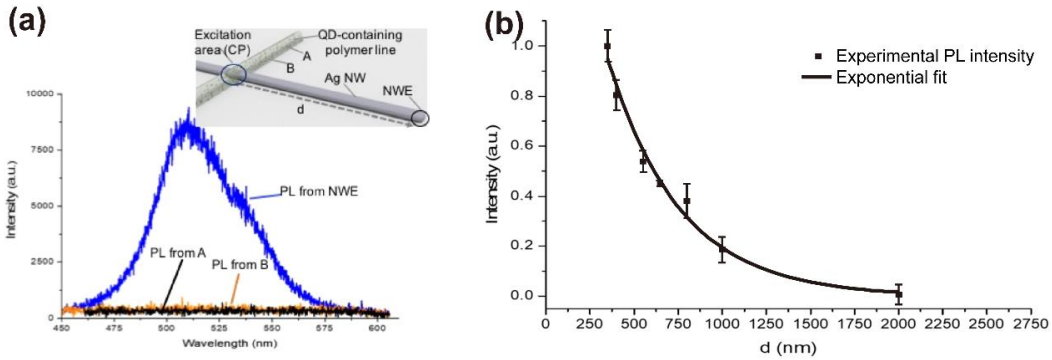

Figure 1-11 (a) PL spectrum from different detecting areas, Blue curve: from the nanowire end. Black and orange curves: from the polymer line outside the nanowire (A and B locations). The excitation position is fixed at the cross point; (b) PL intensity measured at the nanowire end as a function of the distance between the nanowire end and the cross point. (Image reproduced from [60])

1.3.2 Polymerized single emitter coupled with a metal nanoparticle

Over the past decade, hybrid plasmonic nanosources based on energy transfer between metal nanoparticles and quantum dots/nanocrystals or organic dyes have been demonstrated an efficient optical nanosources to be integrated into photonic nanodevices [73–77]. In 1946 Purcell was the first to show that the atom decay rate could vary when subjected to a change of its surrounding local environment [78]. Purcell effect between metal nanostructures and nanoemitters allows for controlling light emission through the control of the deexcitation rate of the nanoemitters. The electromagnetic local density of states of the plasmonic metal nanostructure results in an increase of the deexcitation rate and a decrease of the lifetime [79–81]. Although the outstanding achievements have been reported, a main challenge remains: to control the nanoscale spatial distribution of nanoemitters metal nanoparticles.

In the previous works of our group, a simple approach of plasmon-based two photon polymerization was proposed for integrating the nanoemitters onto the relative metal nanoparticles within nanoscale. In a typical photopolymerization process, light induces the polymerization reaction when the exposure energy dose exceeds a given threshold D_{th}. For the plasmon-based TPP process, shown in **Figure 1-12**(a) and (b), an exposure dose below the D_{th} was instead used, which guarantees no photopolymerization reaction happens except the close vicinity of the metal nanostructures, which enhances the local energy dose of the electromagnetic field that locally exceeds the D_{th} [82–87].

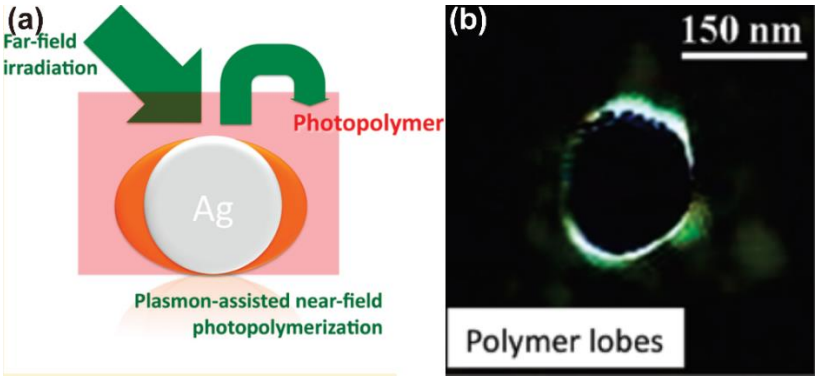

Figure 1-12 (a) Mechanism of the plasmon-based photopolymerization process; (b) Differential image obtained by subtracting the AFM images

before and after photopolymerization process. (Image reproduced from [82])

We have carried on this plasmon-based TPP for nanodisks, nanostars and nanocubes, shown in **Figure 1-13**. Most of the reported hybrid nanoemitters contain only a single output color. In hybrid plasmonics involving emitters, changing the color of emission requires changing the dyes. **Figure 1-13**(a) shows the SEM image of the nanodisk-based emitters (d = 90 nm) with two different quantum dots. The fabrication procedure consisted of two steps. The first step was to polymerize along the X axis to position green QDs in the X direction. The second exposure was performed by coating the sample with the red QDs. The signature of the selective spatial positioning of the QDs is shown by the far-field fluorescence images of the nanodisk-based emitter (**Figure 1-13**(b)). The dominant wavelength can be selected by rotating the polarization of the incident light. The results show the potential to produce switchable plasmonic nanoemitters with considerable applications in nanophotonics. The plasmon-based TPP fabrication technique is also applicable to arbitrary shaped nanoparticles such as nanostars, as the fabricated nanostar-based emitter shown in **Figure 1-13**(c). Thanks the plasmonic lighting-rod effect at the end of each branch, green QDs and red QDs were trapped along X axis and Y axis, respectively. The nanoemitter was also characterized optically by polarization-controlled fluorescence (**Figure 1-13**(d)). Again, the green QDs emission is noticeably higher than the red QDs emission with the incident polarization parallel to X axis, while the red QDs emission is dominant with the incident polarization direction is flipped by 90°. Another example we carried on is the gold nanocubes deposited on an indium-tin oxide (ITO)-coated glass substrate. **Figure 1-13**(e) shows the SEM image of the nanocube-based emitter obtained with an incident light parallel to the cube diagonal at 45° to the x, y axes. **Figure 1-13**(f) shows the its PL intensity as a function of the incident polarization angle. The PL level varies quickly depending on the excitation polarization direction, resulting in the “on” and

"off" states, named "state 1" and "state 0" respectively. So this control of the PL level permits novel perspectives in hybrid nanoplasmonics.

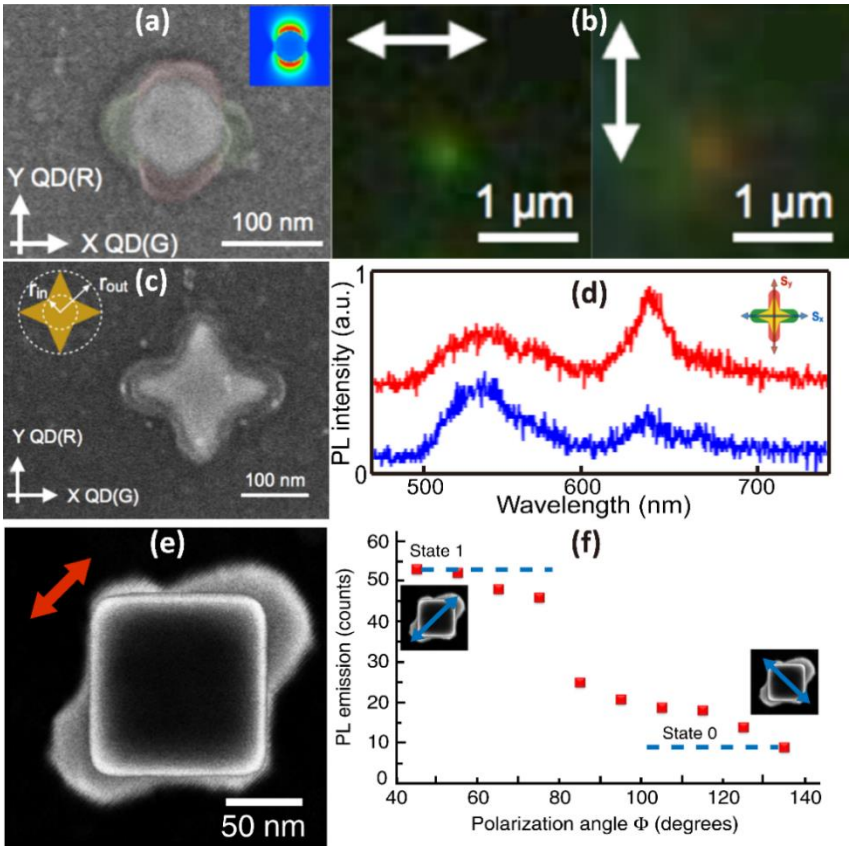

Figure 1-13 (a) SEM image of the nanodisk after second exposure that traps red QDs along the Y axis (Plasmonic near-field intensity of dipole emission for second exposure is shown in the inset); (b) Far-field fluorescence image of the nanodisk-dased emitters under illumination with X axis polarization and Y axis polarization; (c) SEM image of the nanostar-based emitter; (d) Fluorescence spectra collected with the polarization of excitation blue light along X axis (blue) and Y axis (red); (e) SEM image of the nanocube-based emitter; (f) PL intensity as the function of the angle of polarization of the exciting light. (Image reproduced from [39,61])

By decreasing the concentration of QDs within the original polymer solution, single QD or a few ones can be trapped inside the polymer lobes of the nanocube-based hybrid emitter, which extends the possibility of the hybrid nanoemitter to the single photon regime. **Figure 1-14**(a) shows the AFM image of a gold nanocube-based hybrid emitter. The corresponding auto-correlation function $g^{(2)}$ measurement result is shown

in **Figure 1-14**(b). The emission was collected and split into two beams that were coupled into optical fibers, These two fibers were then connected to two APD detectors in order to measure the photon anti-bunching behaviour of the $g^{(2)}$ autocorrelation function. This allowed to measure single photon emitters with high accuracy. At zero delay, $g^{(2)}(0)$ is about 0.35, which is below 0.5. This is the signature of a single photon emission [88]. This result opens up the avenue for polarization-driven tunable nanoemitters and even single photon emitters, which gives us the confidence and reference for the work of integrating single photon emitters onto hybrid photonic-plasmonic structures based on waveguides.

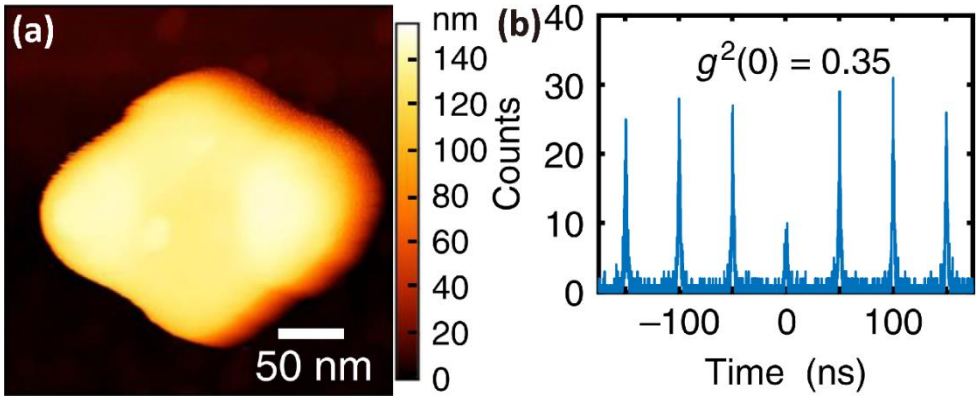

Figure 1-14 (a) AFM of a hybrid nanoemitter based on a nanocube. The polymer lobes contain a single or a few QDs; (b) $g^{(2)}$ autocorrelation function measurement showing $g^{(2)}(0) = 0.35$. (Image reproduced from [61])

1.3.3 Glass-based ion-exchanged waveguides (IEWs)

Glass is a well-known optical material and glass wafers are naturally oxidized and cost-effective compared to silicon wafers. Glass waveguides have several advantages including low cost, compatibility with commercial optical fibers, low propagation loss. Therefore, glass-based waveguide is a perfect candidate for the integrated photonic platform in our work. The ion-exchange on glass technology, developed for more than thirty years, is a simple and economy fabrication process. Indeed, the various ion exchange processes developed for integrated optics during the last decades allow

creating either surface optical waveguides or buried waveguides. In our situation, the surface buried waveguides with gradient refractive index distribution in cross-section were chosen. They are particularly indicated for sensing, as the guided light near the surface can interact efficiently by evanescent or hybrid coupling with structures on top [89,90]. The basic fabrication process is shown in **Figure 1-15**(a). After exchanging the Na^+ ions contained in a glass matrix by Ag^+ ions with the help of a mask, the ion-exchanged waveguide with graded refractive index is created on the surface substrate glass. **Figure 1-15**(b) gives a cut-view of the refractive index distribution of an ion-exchange waveguide. The sizes of width and diffusion depth are both around 2 µm. The position locates at the center on the waveguide surface has the maximum refractive index n = 1.57. All the IEWs sample were fabricated and offered by the cooperation TEEM PHOTONIS. The low refractive index contrast between core and glass substrate allows the weak light confinement, this can be benefit for doing polymerization with the surface-bound evanescent waves. (see Chapter 2)

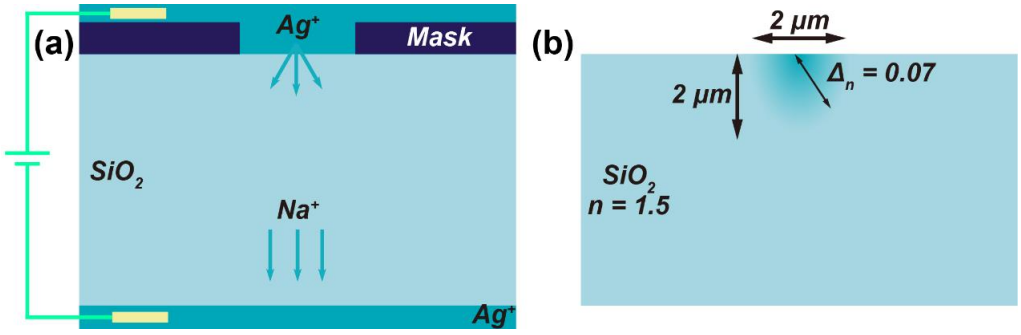

Figure 1-15 (a) Fabrication process of an ion-exchange waveguide, an external thermal field is applied to assist the migration of the Ag^+ ions into the glass. Meanwhile, the exchanged Na^+ ions move into the cathode; (b) Cut-view of refractive index distribution of an ion-exchange waveguide.

1.3.4 Quantum dots/semiconductor nanocrystals

Single photon sources/emitters can emit only one photon at a given time when exposed by an external optical pump. During the optical exposing, an electron can jump

from valence band to the excited band, then rapidly releases to the lower band, and emits one photon with lower frequency.

There are mainly two types of single photon sources, on-demand and probabilistic. For the on-demand single photon sources, most researches use diamond color centers, nitrogen-vacancy (NV) centers in particular are one of most promising candidates for single photon generation. Besides, artificial atoms, or quantum dots, and single moleculars are also used frenquently for obtaining single photons or producing highly entangled photon pairs. Probabilistic single photon sources can be generated probabilisticly rather than on-demand. Spontaneous parametric down-conversion (SPDC) and four wave mixing are the most popular generating ways.

Here we chose colloidal semiconductor nanocrystals/quantum dots as the photon sources for our application due to several reasons.

a) In the terms of photonic application, deterministic and on-demand single photon sources are more suitable to integrate.
b) Quantum dots can more stable and efficiency at room temperature, so they can be operated conveniently.
c) For the luminecense measurement, quantum dots need lower excitation laser power.
d) Colloidal quantum dots can be easily mixed with other liquid solutions for our application.

1.4 Objective of the thesis

The objective of this thesis is to integrate nanoemitters on glass chips based on the ion exchange technique. In the long run, we want to realize an optical light bus communication between different emitters in the visible range. A lot of current technologies are based on silicon photonic substrates, using complicated fabricating process. In quantum optics, single photon emission is mostly done in free space, which limits their applications on most pre-existing photonic chips (see methods in section

1.1). However, so far, less effort has been put into creating nanoemitters on glass chips with efficient integrating methods.

Photonic-plasmonic hybrid light concentrators proposed previously at the L2n have demonstrated efficient structures for producing a 'hotspot' [91], which is highly suitable for obtaining a Purcell effect system [78], as shown in **Figure 1-16**(a). Thereafter, similar structure configurations based on ion exchange waveguides were also proposed as a photonic platform for the integration of single photon sources, schematically shown in **Figure 1-16**(b). In this type of structures, the possibility of light coupling between nanoemitters and photonic structures was demonstrated feasible using simulation methods. Some results of these simulations on the coupling between nanoemitters and plasmonic modes on an integrated photonic overlayered structure on the ion exchange waveguide could be found in Josslyn Beltran Madrigal's PhD thesis [92]. These previous work done at the L2n in the last few years and in collaboration with the company TeemPhotonics (in Meylan) drove our choice towards the use of this photonic platform based on ion exchange waveguides in glass.

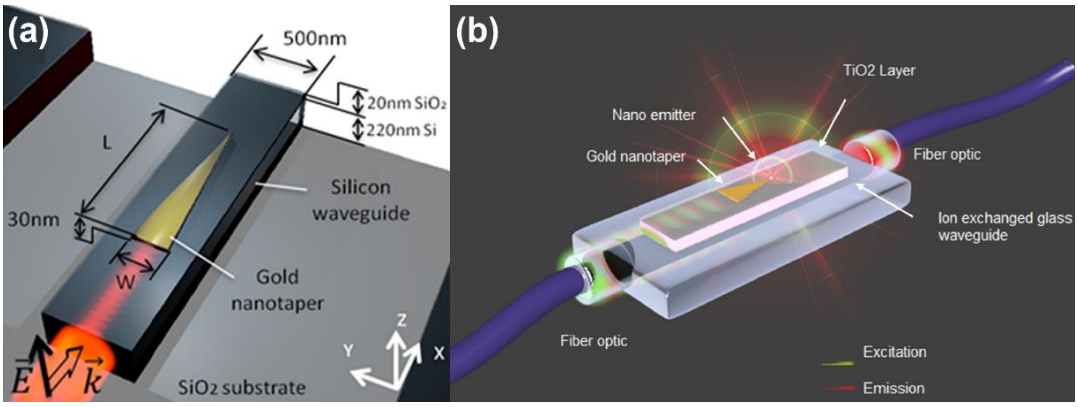

Figure 1-16 (a) Schematic illustration of the hybrid nanotapered light concentrator integrated on silicon ridge waveguide; (b) Schematic representation of the glass waveguide-based photonic circuit integrated with nanoemitters located near a 'hotspot'. (Image taken from [91,92])

As we shall see in the following chapters, for the issue of integrating nanoemitters on this photonic platform, the photopolymerization principle based on photon

absorption was used for our goal. Colloidal nanocrystals (also called quantum dots in the manuscript) dispersed inside polymer solutions have been used for the demonstration emitting systems which have been implemented widespread to develop sensing systems, electronic devices and light emitting diodes (LEDs) [93–98]. However, there is very little work on using this method for creating light (nano)emitters. This is what was intended for this PhD work.

In chapter 2, the photopolymerization reaction initiated by guided evanescent waves are developed and we will show that it can enable us to create polymer-QDs ridges along the waveguide. In chapter 3, we present the developed direct laser writing technique based on two photon polymerization which we used for fabricating nanoscale polymer-QDs composites there were eventually integrated directly on top of a waveguide. Finally, Chapter 4 gives more additional experiments and measurements for potential and practical problems which could be helpful for complex hybrid photonic structures in the future.

Chapter 2 Polymerized nanoemitters by guided evanescent-wave (GEM)

2.1 Introduction

In this chapter, we first characterize the propagation properties of light within ion-exchanged waveguides and the stability of the experimental set-up, crucial for photo-polymerization. Secondly, two main experiments are proposed, which are described in section 2.3 and section 2.4, respectively. The physical mechanisms can be depicted in **Figure 2-1**. In one case, the polymer resin is casted directly onto the surface of a waveguide and absorbs the energy from the surface evanescent wave to trigger the photo-polymerization process, as shown in **Figure 2-1**(b). While in the other case, a dielectric layer (TiO_2) with a high refractive index is deposited on the waveguide surface for transferring guided light into the TiO_2 layer. The polymer resin is then dropped on top and the photopolymerization process is triggered by the light energy which is located on the TiO_2 surface as shown in **Figure 2-1**(c). Finally, we describe the potential of our methods for confining the light to small areas for future structures where we combine with a tapered TiO_2 ridge in order to create a nanoscale emitter.

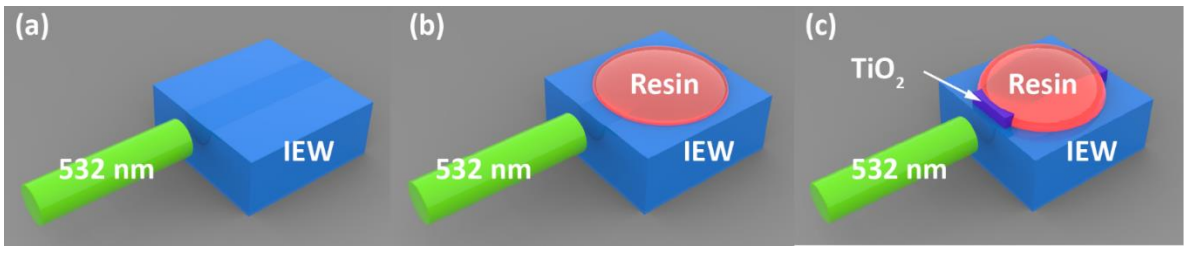

Figure 2-1 Schematic of the physical mechanism of photopolymerization by the waveguide coupled propagating light. (a) A 532 nm laser is coupled into an IEW. (b) Photopolymerizatiom experiment on a single waveguide

where a photoresin droplet is cast directly on it. (c) Photopolymerizatiom experiment on a two-layer waveguide with a TiO_2 layer on top of the IEW.

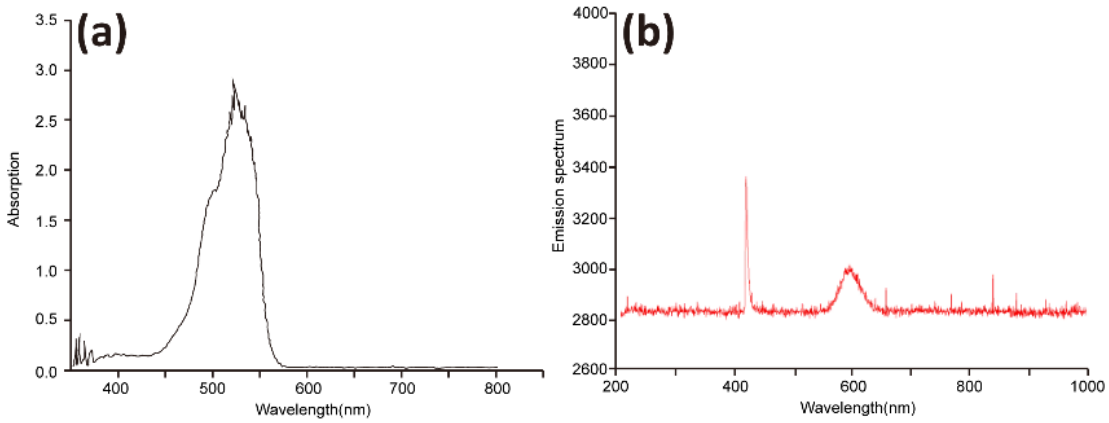

Figure 2-2 Measured absorption (a) and photoluminescence (b) for R_2.

In this work, two kinds of resins were used for the photopolymerization:

R_1: PETA+0.5%Eosin Y + 4%MDEA

R_2: PETA+0.5%Eosin Y + 4%MDEA+ 1% CdSe/ZnS QDs (emission: 590 nm)

The minimum absorbed energy dose triggering the photopolymerization process is called 'threshold' which is related to the exposure time (t) and the coupled excitation laser power (P_c) and we consider the product $t \times P_c$ [99]. The threshold of the sample R_2 was found to be $6.5 \times 10^4 mJ/cm^2$ at λ = 532 nm for the laser excitation. **Figure 2-2** (a) shows the absorption spectrum of R_2. As a matter of fact, the resin alone is more sensitive to blue light. However, with the presence of Eosin Y, we see that the resin becomes more sensitive to green light (**Figure 2-2** (a)). This turns out to be beneficial for our experiments as having a green laser propagating in the IEW is easier than with a blue laser. Moreover, the green laser hardly causes any damage to the quantum dots embedded inside the resin during the photopolymerization process. **Figure 2-2** (b) shows the photoluminescence measurement of R_2. Excitation was done with a 405 nm laser (visible on the spectrum) and the quantum dots emission is around 590 nm.

2.2 Experimental set-up based on GEM

Our home-made experimental set-up used for implementing the photopolymerization comprises two lasers, shown in **Figure 2-3**. Here, a 532 nm green excitation laser is used to couple into our waveguides, resulting in a surface evanescent wave which is then strongly absorbed by the polymer resin and trigger the photopolymerization process. An additional 640 nm red laser, at which wavelength the polymer resin is not sensitive, is used for fiber-edge laser coupling alignment before switching on to the green laser for fabrication. Two lasers are thus focused into an optical fiber splitter using objective lenses and then connected with a tapered single mode fiber. The tapered fiber (OZ Optics Ltd.) is produced by gently stretching an optical fiber while it is heated and it has thinner fiber core, shown in the inset of **Figure 2-3**. The tapered fiber tip reduces the mode area in order to achieve an improved coupling to the waveguide [100]. The tapered fiber is fixed to a x-y-z translation stage for adjustment of the coupling. Moreover, the IEW sample is also put on a sample holder which can be rotated and translated for ensuring that the light out from the fiber can be coupled into the waveguides efficiently. Besides, an electronic shutter was put along the green laser path in order to control the exposure time of the green laser. As for measuring the output laser power from the core of the waveguide output, a 20× objective lens is approached to the end of the corresponding waveguide in order to expand the output laser beam and observe the coupling. In addition, a pinhole is used for separating the light from the core. Finally, the power can be measured with a power meter behind the sample. The transmitted light is sent into an objective lens upon the sample and transferred to a CCD camera for observation.

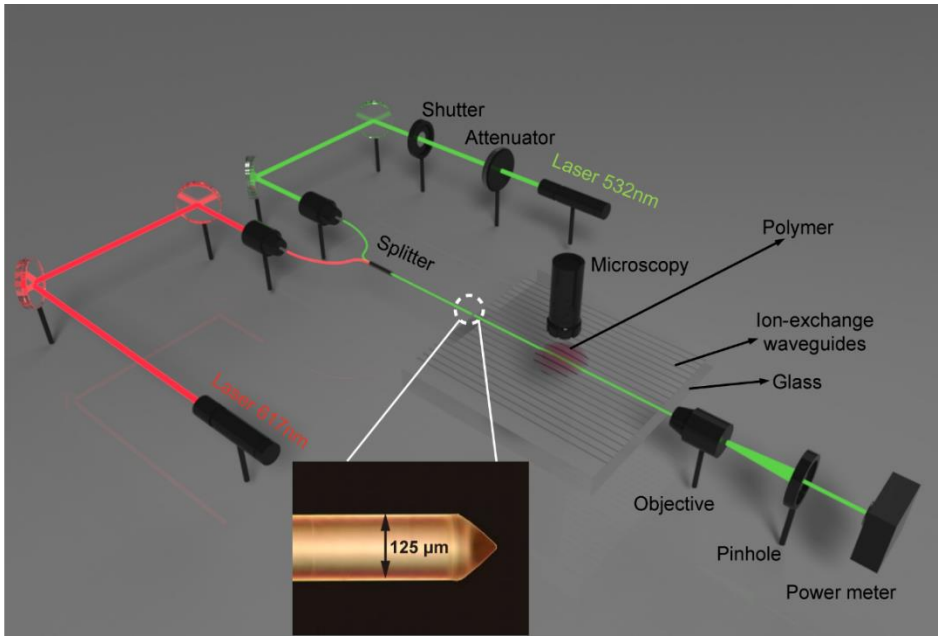

Figure 2-3 Experimental set-up for guided evanescent waves. Inset shows the details of the tapered fiber tip.

2.2.1 Stability optimizing of set-up

The light coupling efficiency from the tapered fiber to the waveguide is sensitive to the mechanical vibrations of the set-up. Therefore, it is quite necessary to optimize the laser coupling and the mechanical stability of the set-up before switching the laser source to the green laser. During the whole photo-polymerization process, the waveguide-coupled laser power should be kept constant. Several strategies have been made for reducing variations of light transmission in time.

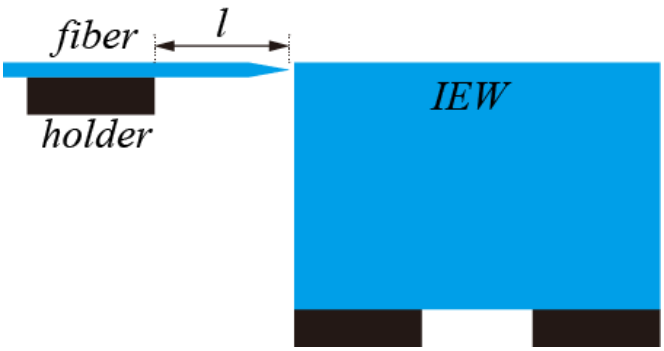

Figure 2-4 End-butt coupling stage. Fiber and IEW sample are both fixed on movable stages.

First, we reduced the length of the overhead part of the fiber *l* from 3 *cm* to 1 *cm*, as shown in **Figure 2-4**. As the IEW sample and the fiber are fixed on the stages, the end-butt coupling is easily affected only by the position of the overhead fiber part due to the fiber weight.

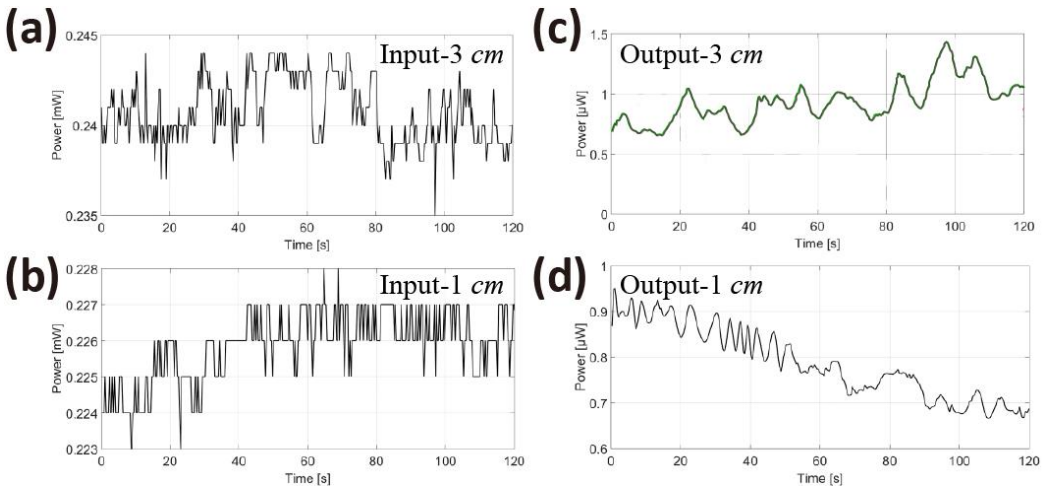

Figure 2-5 Laser power measurement with for a time of 120 *s*. Measured input laser power with overhead part of 3 *cm* (a) and 1 *cm* (b); Measured output laser power with overhead part at 3 *cm* (c) and 1 *cm* (d);

Here, a 640 nm laser was coupled into waveguide and we measured the input laser power P_{in} and output laser power P_{out} as function with time, as shown in **Figure 2-5**. We should mention here that the gap between the fiber tip and the corresponding waveguide changes every time we couple the laser for measurements. In order to compare the stability before and after reducing *l*, the measured errors are calculated by the equation (2-1) below, and the E_{in} decreases from 3.74% to 2.05% and the E_{out} decreases from 83.6% to 37%.

$$E_{in/out} = \frac{P_{max} - P_{min}}{P_{average}} \tag{2-1}$$

Where P_{max} and P_{min} is the maximum and minimum output laser power we could recored within 120 s, respectively. $P_{average}$ is the calculated average value.

The second potential source of the vibrations is from the fiber type used. Polarization maintaining (PM) optical fibers are the perfect candidate for preserving the

polarization of the propagating laser [101]. Here, we measured the P_{out} with a polarization maintaining fiber, as plotted in **Figure 2-6**. The calculated error E_{out} is 8.39% which is much lower than using the standard SM tapered fibers (37% in **Figure 2-5** (d)). This indicates a more stable output laser power can be obtained by using polartiztion maintaining fibers.

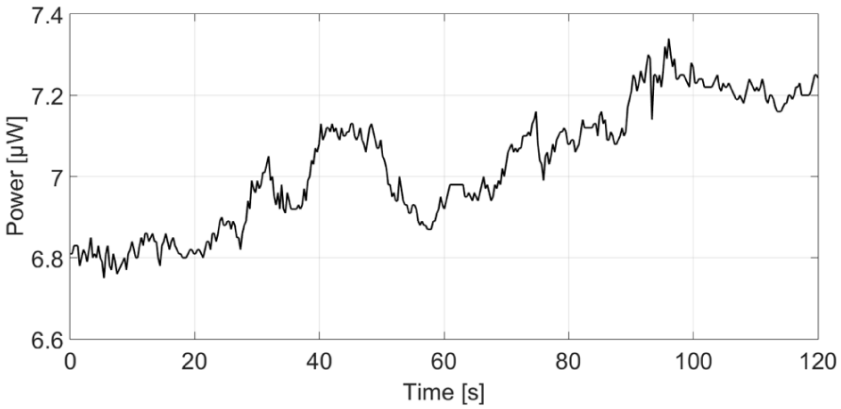

Figure 2-6 Measured output laser power with PM fiber

Another approach was considered for increasing the stability of the coupling condition by using immersion oil as the inter-medium between the fiber and the waveguide, as shown in **Figure 2-7**(a). Here, a droplet of PETA polymer resin without any quantum dots and photoiniators was placed at the gap between a cleaved fiber tip and a corresponding waveguide edge. The refractive index of the PETA polymer resin is almost the same as the glass fiber and our waveguide core. In this configuration, light reflection can be ignored due to highly-matched refractive index. Another advantage of this inter-medium is to increase the N.A of the waveguide and the fiber in order to get more laser light coupled into our waveguides [102]. We also measured the output laser power and compared the errors, as shown in **Figure 2-7**(b). The measured laser output error E_{out} decreased further to 5.62%, around 15 times higher than the stability using the fiber with a too long overhead tip (83.6% in **Figure 2-5**(c)). In addition, off-states of other electronic equipments and indoor fan system near the set-up can also help improving the experimental stability.

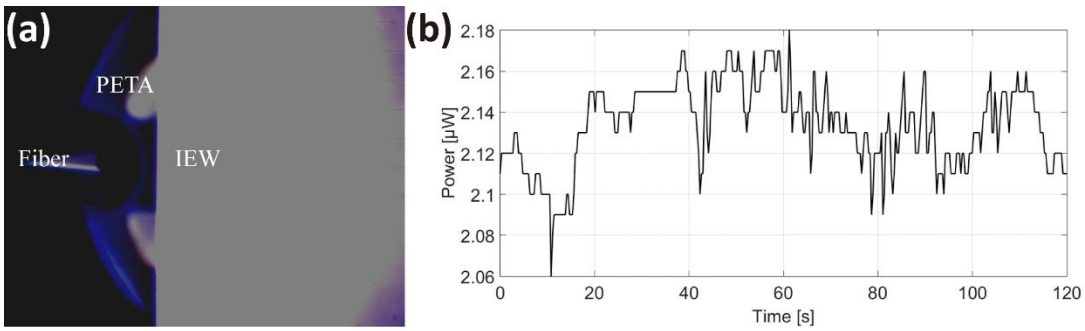

Figure 2-7 (a) One droplet of PETA attached between the fiber and the IEW; (b) Measured laser output power.

2.2.2 Light transmission characterization

Characterizing the light transmission properties of our IEW is necessary for understanding the photopolymerization happening on top. Our ion-exchanged waveguides are designed to support a single mode ranging from visible light to near-infrared light. As shown in **Figure 2-8** (a) and (b), both green and red lasers can be coupled into the IEW, the propagating loss for a red laser is lower than that with a green laser. This can be confirmed by the color intensity distribution measured by the CCD camera mounted above the observing objective lens. During the measurement process, the lasers were coupled into the waveguides, and the light leakage of waveguides surface went through a 20× objective lens and observed by a CCD camera which gave an observing area of 0.1× 0.1 cm^2. In order to obtain the surface light distribution of this whole waveguide along the propagation direction, we moved the microscopy system step by step. Finally, we put together all the images obtained at each step. As shown in **Figure 2-8** (c) and (d), the *x* axis represents the propagation length of the laser along the waveguide and the *y* axis is color intensity. Obviously, the transmission of green light starts to drop significantly in the middle (shown with the white markers in **Figure 2-8**(c)), while the propagation distance of red light is longer.

Although we can't measure the real laser powers inside the waveguide, we still calculated the light propagation losses using the obtained leak light intensities both for

green light and red light. Here, the propagation loss can be described by attenuation constant which means the power loss per 1 *cm*. It can be expressed according the following formula [103]:

$$\alpha = -\frac{10}{L} l_g \frac{I_0}{I_1} (dB/cm) \quad (2\text{-}2)$$

Where L is the length of the waveguides and I_0 and I_1 represent the light intensities at the start and the end positions. We roughly estimated from the **Figure 2-9**(c) and (d). The light intensities dropped to *1/10* of the value at the initial position for green light and *1/5* for red light which give the attenuation constants of -10 *dB/cm* and -7 *dB/cm*, respectively. There are also the input-coupling loss and output-coupling loss. The total light transmission can be calculated by $T = P_{out}/P_{in}$. There are over 100 waveguides on the same glass substrate and each of them has different surface quality and edge coupling conditions. We thus tried with over 20 waveguides and calculated the average of P_{out}. As shown in **Figure 2-9**, the output light is expanded by an objective lens and the observed red laser output spot is much brighter than the green laser output spot. The final calculated transmission is 0.07% for 532 nm laser and 3.1% for 640 nm laser.

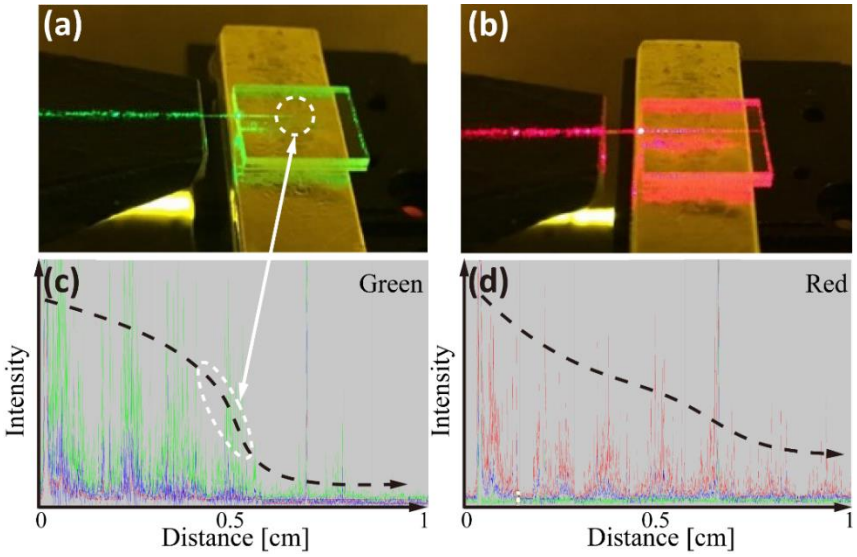

Figure 2-8 IEW-coupled green laser (a) and red laser (b); Color intensity distribution of the CCD images for green (c) and red laser (d) propagating along waveguides.

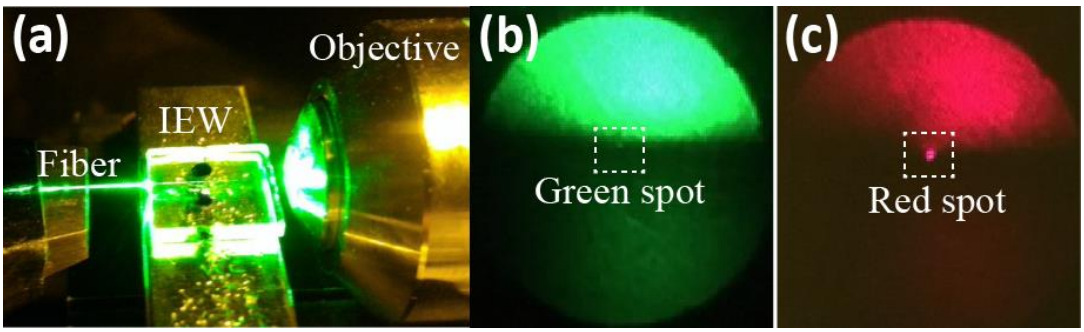

Figure 2-9 (a) Collecting microscope objective for enlarging the output light distribution; Output green spot (b) and red spot (c).

2.3 Polymeric ridges on IEWs

In this subsection, we analyse the size and emission of the polymeric ridges fabricated on top of our IEWs. We first discuss our abilities to control the size of our polymer-resin without quantum dots dispersed inside by changing the coupled excitation laser and the exposure time. Then, a polymer-resin embedded with QDs is used for creating polymer-QDs ridges whose emissions were also recorded by our home-build PL measurement set-up.

2.3.1 Characterization of polymer ridges

A small droplet of R_1 was casted on top of the IEW surface at the surface of the fabricated waveguides before adjusting the input coupling of the red laser. By monitoring the output power for the red laser, we can ensure the same output power for the green laser for each photopolymerization process. To find the threshold of R_1, we fix the output red laser power to 5 *nW*, the corresponding minimum laser power value has been found as the one below which no ridges were observed by AFM measurements. Here, by controlling the exposure time, we got ridges with different dimensions after cleaning the non-exposed resin, as shown by the white areas in **Figure 2-10**. Results suggest an empirical threshold exposure time *t* value of about 1 min.

Figure 2-10 CCD image of polymer ridges made with mixture R_1 with different exposure times.

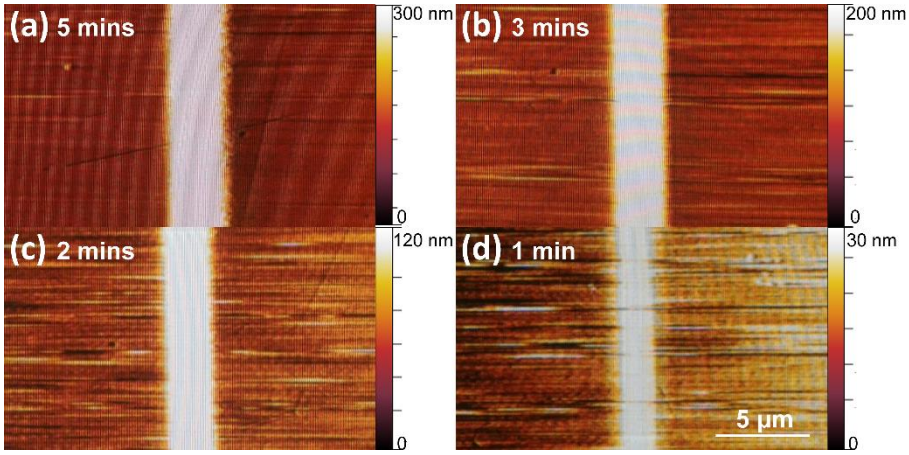

Figure 2-11 AFM measurement images of polymeric ridges made with mixture R_1 for 5 min (a), 3 min (b), 2 min (c) and 1 min (d).

All fabricated polymeric ridges have been characterized by AFM in terms of their height (*h*) and width (*w*), as shown in **Figure 2-11**. The dimensions of the obtained ridges are resumed in **Table 1**. The ridge width varies from 1.8 to 3.33 µm which is comparable to the width of the waveguide core (2 µm). In the same time, the ridge height increases from 23 to 255 nm. The results show the potential of this method for creating polymer waveguides with a width and a height down to nanoscale which is beyond the standard optical diffraction.

Table 1 Dimensions of polymeric ridges with different exposure times.

Time / Size	5 min	3 min	2 min	1 mins
w (μm)	3.33	2.89	2.73	1.8
h (nm)	255	159	100	23

A second experiment was carried out in order to create polymer ridges embedded with quantum dots using the mixture R_2. The energy threshold of R_2 is higher in the presence of QDs because QDs can also absorb part of the excitation laser during the process. In order to find the threshold of R_2, the exposure time is fixed at 1 min, and the input laser power was increased gradually from 5 *nW* until the minimum output laser (about 15 *nW*) which can trigger the process. **Figure 2-12**(a) shows the minimum polymer ridge obtained by 1 min and 15 *nW*, the measured width and height are 1.81 μm and 16.33 nm (**Figure 2-12**(b)). **Figure 2-12**(c) shows the larger ridge with 5 min and 15 *nW* which has 2.69 μm in width and 84.4 nm in height (**Figure 2-12**(d)). In particular, the ridge with 16.33 nm height is an important result as it is just slightly larger than the average diameter of our quantum dots which is around 15 nm typically. In the future, our technique can thus be used for fabricating polymer waveguides containing a single layer of nanoemitters.

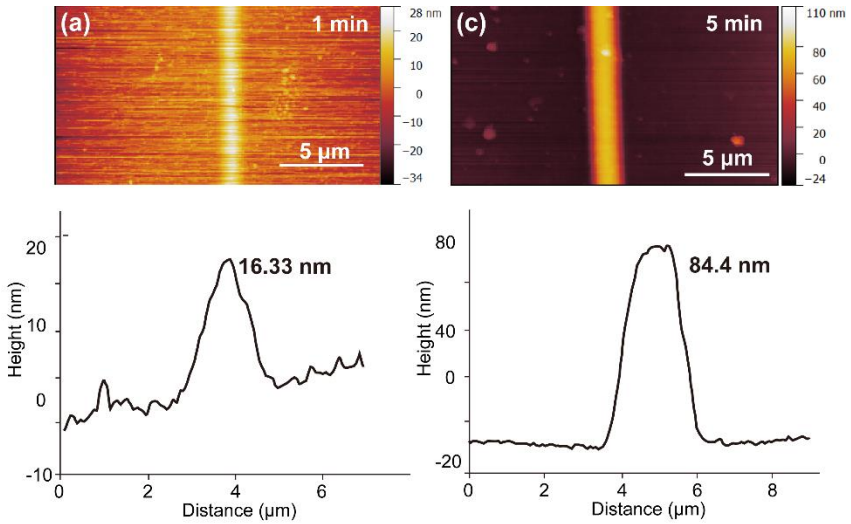

Figure 2-12 AFM measurement results of polymeric ridges made by mixture R_2 with exposure times of 1 mins (a-b) and 5 min (c-d).

During the process of photopolymerization, the refractive index of the polymer resin changes due to the absorbed laser energy [104]. Our measured refractive index value of polymer resin before photopolymerization is around 1.52, while it goes up to about 1.58 after photopolymerization [105]. This value is almost the same as the index value of the waveguide core, resulting in lower light confinement of the IEW. Besides, the quantum dots dispersed inside polymer resin also absorb part of the laser energy which also reduces the output propagating laser power. The measured output red laser power during the whole photopolymerization process (within 9 min) is shown in **Figure 2-13**. As one can see, the output power decreases over time, and keep constant after 400s, which indicates the local polymerization process finished.

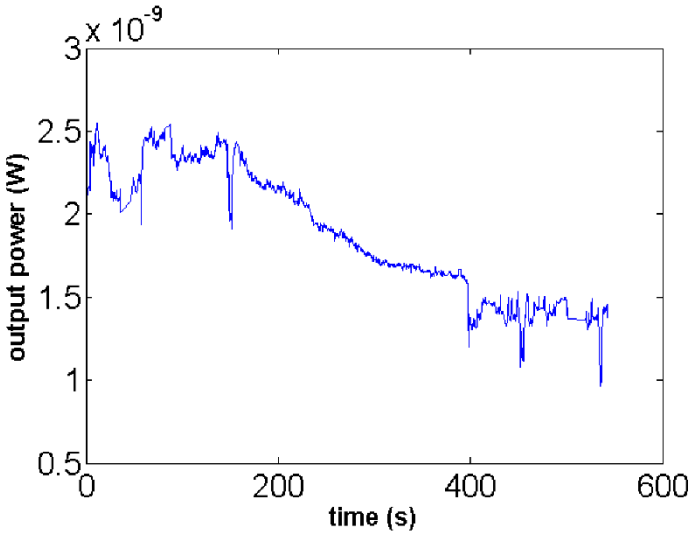

Figure 2-13 Detection of the output power during 9 min along the process.

2.3.2 Photoluminescence Characterization

In this subsection, we organized PL measurements to verify the presence of QDs inside the ridges. All measurements were conducted using a home-built confocal microscope equipped with an imaging spectrometer mounted with a Peltier-cooled CCD sensitive camera. Here, we can obtain not only the spectrum measurements from the specific locations by choosing the 404 nm laser, and also the measured PL images

for large-area of the sample surface by switching the excitation light source to a 450 nm LED. A yellow lamp was used here in order to illuminate the sample and not damage the QDs light emitting property. The QDs emission was collected by the same objective lens and then split by a 20: 80 (T: R) beam-splitter BS_2. The reflection was finally detected by a CCD camera and the transmission was captured by the imaging spectrometer with a high-pass filter (≈ 510 nm) which was set in front of the slit of the spectrometer. The experiment setup is shown in **Figure 2-14**.

Figure 2-15 shows the fluorescence of two polymer-QDs ridges (fabricated with the laser exposure time of 5 minutes and 3 minutes) under the illumination of the 450 nm LED source. It is clear that the first ridge (5 min) is brighter than the second one (3 min), which is due that a bigger volume of polymer-QD compsoite results in more quantum dots embedded inside. As comparison, there is no emission from the part without ridge, marked with white dashed line.

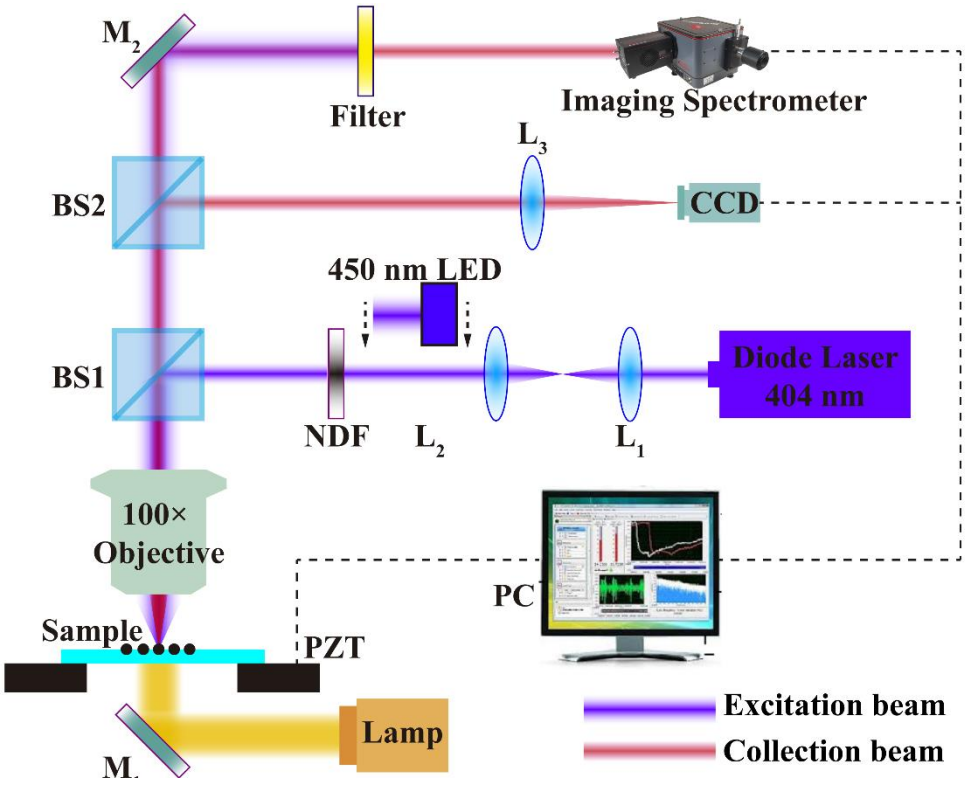

Figure 2-14 A home-made photoluminescence measurement set-up. NDF: neutral-density filter, BE: beam expander, M: mirror, BS: beam-splitter.

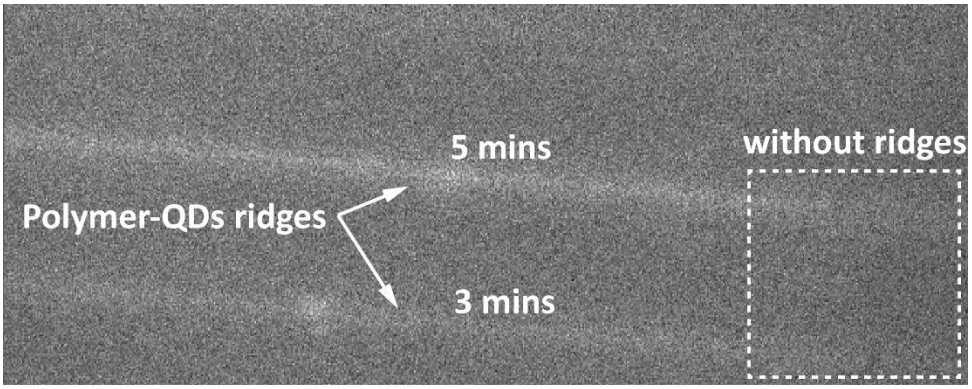

Figure 2-15 Emission of two polymer-QDs ridges with different exposure times, the emission is filtered with a 510 nm filter, excitation: 404 nm LED light source.

In order to analyse the fluorescence coming from the polymer-QD ridges, we also examined PL measurements for the different polymer solutions. **Figure 2-16**(a) shows the measured curve for polymer ridge which seems to be quite broad due to the contributions of the different compounds in the mixture R_2. There are basically two peaks which are located at 562 nm and 590 nm, respectively. Besides, two more measurements were carried in order to distinguish the two peaks, shown also in **Figure 2-16**(a). Among these curves, the blue dashed line represents the emission spectrum of PETA + Eosin Y which has a peak around 562 nm, while the green dashed line curve is for the emission of PETA + QDs with the peak around 590 nm. As one can see, these two peaks exactly overlap with the two peaks observed in the red curve which is the final mixture containing all the compounds. The peak at 590 nm belongs to the QD emission while the peak at 562 nm is caused by the Eosin Y resin. There is another peak between 510 nm and 520 nm which is attributed by the MDEA emission. **Figure 2-16**(b) shows the fluorescence images collected by the same confocal microscope. The emission of the whole polymer ridge is observed with a 20× magnification objective lens (**Figure 2-16**(b), top), and a quite intense emission spot is evidenced by focusing the excitation blue laser on a specific part of the ridge with a 60× magnification

objective (**Figure 2-16**(b), bottom). The results show high light emitting property of these integrated polymer-QD ridges.

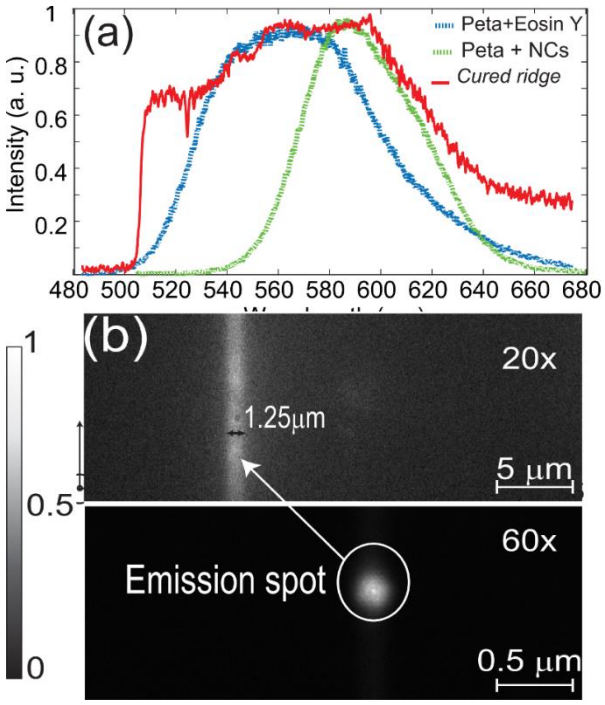

Figure 2-16 (a) Measured emission spectrum of the photopolymerized ridge (red solid line) compared with the emission of the PETA+Eosin Y (blue dashed line, peak at 562 nm) and of the PETA + QDs (green dashed line, peak at 590 nm); (b) Fluorescence images of the whole ridge (top) and a portion of the ridge (bottom). (Images reproduce from [106])

2.4 Polymeric ridges on TiO_2 layer of IEWs

As shown in Section 2.3.1, the length of the polymerized ridges depends on the dimension of the photo-resin spread on the surface, which is usually longer than 500 μm. As the purpose of our project in the future is to position a single nano-emitter on top of an IEW, it is necessary to confine the light down to a nanoscale volume and thus not only in height, but also in length and width. Based on our previous works [92], the presence of TiO_2 ensures an optimal confinement of light and an efficient coupling with the IEW glass waveguide underneath. Therefore, by coupling the excitation laser with

lower power (below the threshold of photopolymerization) into the waveguide, we can fabricate a small area of photo-resin containing less QDs by our photo-polymerization method. This could be a new and potential integrating method for applications in the context of integrated photonics.

2.4.1 Confinement of guided light

Here, titanium dioxide (TiO_2) was chosen due to its low loss light propagation and its abilities to support single- and multi-mode visible light [107–109]. Due to the proximity of the IEW and TiO_2 layer, the evanescent wave of the propagating mode of the IEW is able to excite the modes of the TiO_2 slab [110]. **Figure 2-17**(a) shows the propagating light distributions at cross-section for a IEW. The propagating light is concentrated inside of the waveguide core, however, parts of light locates at top surface can be exist as evanescent wave of which the electric field intensity away from the surface decrease exponentially [111]. In a system formed by two parallel waveguides placed in close proximity to each other, it is possible to observe a mode coupling between its fundamental modes due the interaction of its evanescent waves [112]. The energy of the modes propagating through the IEW can be transferred to the TiO_2 slab and vice versa. The interaction between the propagating modes of IEW and TiO_2 slab gives rise to hybrid modes that allow periodic energy transfer between both waveguides [113,114]. **Figure 2-17**(b) shows the simulated light energy exchange between the IEW and a TiO_2 slab on top of it using Finite Difference Time Domain (Lumerical - FDTD). Here, the height h of the TiO_2 layer was set to 180 nm, and the width w was set to 2 μm. A mode source at 532 nm (TE mode) was used as a light source in this simulation. It can be observed that the propagating light can be coupled into the upper TiO_2 layer, and then back into the IEW again. The cross-view light field distributions at position P_1 and P_2 which has maximum and minimum light intensity transferred into TiO_2, respectively, are shown in **Figure 2-17**(c) and (d). Here, the distance between two neighboring positions have maximum light intensities is defined as ‘beat length (BL)’ [115].

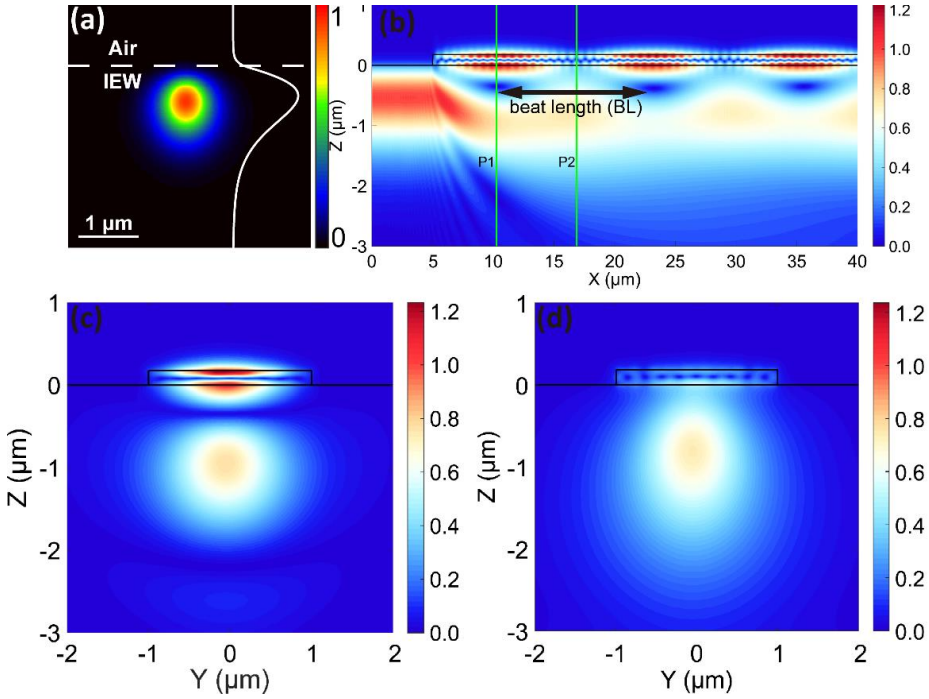

Figure 2-17 (a) Cross-section light distribution of fundamental TE propagating mode of the IEW. White line representes the electric field profile. (b) Side-view of the simulated light with a coupling of the optical modes between the IEW and the TiO_2 slab. Electric field distribution at maximum intensity-P_1 plane (c) and minimum intensity-P_2 plane (d).

Figure 2-17 show the simulated beating behaviour of the IEW-TiO_2 structure surrounded by air. Here, a thick layer of medium was added to the simulation model in order to simulate the structure surrounded by the QD-polymer liquid. The refractive index of the pure PETA polymer changes from 1.485 to 1.52 before and after the DLW-TPP measured by spectroscopic ellipsometry [105,116]. The QD-polymer formulation in this work is actually a mixture made of a monomer (n=1.484), a photo-initiator, an inhibitor (n=1.533) and QDs (n=2.549). it is speculated that the equivalent refractive index of nanocomposites should be at least 1.52 [117–119]. A more accurate value can be obtained by a complicated measurement which should take into account not only the QDs doping ratio, but also the printing laser power and the homogeneity of QDs inside the composites." Here, we set the refractive index of the QD-polymer liquid to about

1.52. We investigated how the sizes of the TiO_2 ridge affect the value of the BL, we firstly simulated the light field distributions and calculated the BL values by sweeping *h* (140 - 200 nm) and *w* (1 - 4 μm) with the input TE mode source, as shown in **Figure 2-18** (a) and (b). It is quite clear that the BL is strongly affected by the value of *h*, and the curve becomes flat when the height is higher than 180 nm and the BL value decreases to below 2 μm. The inset of **Figure 2-18**(a) shows the FDTD simulated side-view |E| distribution with *h* = 160 nm. Next, we studied the effect of the TiO_2 layer width on the beating length. As shown in **Figure 2-18**(b), the beating length almost unchanged with the width from 1 μm to 4 μm. Here, a simulated result is shown in the inset of **Figure 2-18**(b) with *w* = 1 μm, and the beat length is about 3.8 μm.

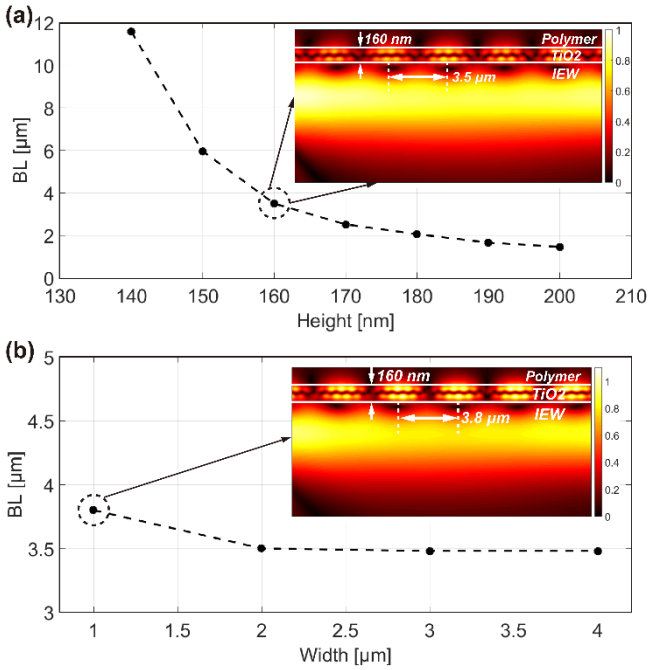

Figure 2-18 For the incident light with TE mode: (a) Simulated beat length-BL with varying height of the TiO_2 ridge, with a 2 μm width. The inset is FDTD simulated side-view |E| profile with *h* = 160 nm; (b) BL as a function of the width of the TiO_2 ridge, with a 160 nm height. The inset is FDTD simulated side-view |E| profile with *w* = 1 μm. The white lines represent the outlines of TiO_2 layer.

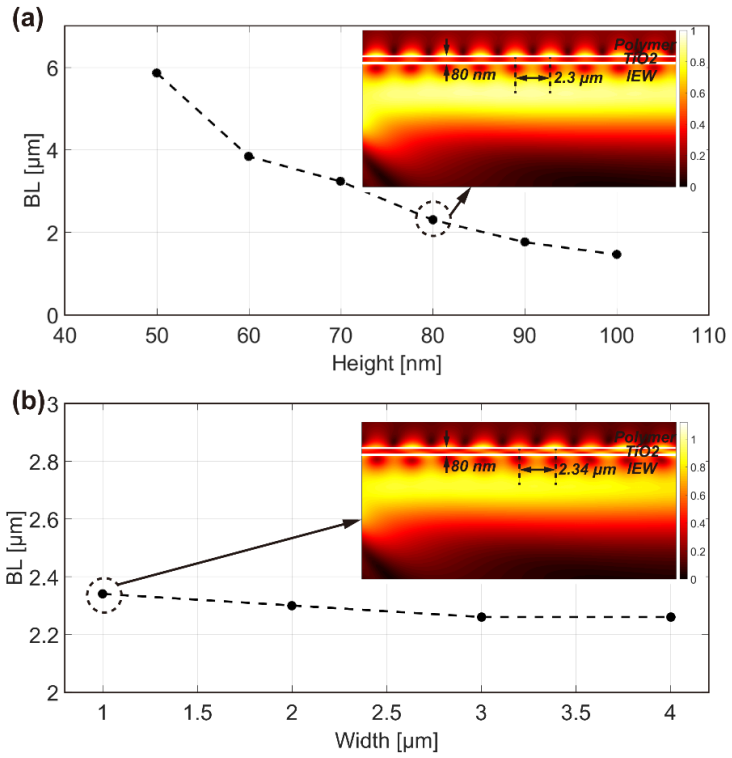

Figure 2-19 For the incident light with TM mode: (a) Beat length decreases as the height of TiO_2 layer increases, the TiO_2 ridge width *w* was fixed at 2 μm. The inset is the FDTD simulated side-view of light propagation with the deposited TiO_2 ridges for *h* = 80 nm; (b) BL as a function of the width of the TiO_2 ridge (*h* = 80 nm). The inset is FDTD simulated side-view |E| profile with *w* = 1 μm. The white lines represent the outlines of TiO_2 layer.

Besides the situation of TE mode, **Figure 2-19**(a) show the relationship between the BL and the height *h* for the TM propagating mode. As one can see with the increasing of the height, the value of BL decreases from 5.86 μm (*h* = 50 nm) to 1.46 μm (*h* = 100 nm). We also simulated the effects of the ridge width on the BL for the TM mode. As shown in **Figure 2-19**(b). Here, we fixed the TiO_2 ridge height at 80 nm, and sweeping the width from 1 μm to 4 μm. A similar behaviour in **Figure 2-18**(b) in which the TiO_2 layer width has almost no influence on the BL. A simulated example

with the width of 1 μm, which gives a BL of 2.34 was shown in the inset of **Figure 2-19**(b).

As our simulated results show that the width of the TiO_2 layer has little influence on the beat length for TM mode source, we deposited a TiO_2 slab instead of a TiO_2 ridge, Here, a TiO_2 slab with the height of 83 nm was deposited on IEWs, shown in **Figure 2-20**(a). Next, we coupled the TM mode of the green laser into the IE waveguide, part energy of the scattered light was absorbed by the photoresin on top of the TiO_2 slab and then triggered the photopolymerization process. After removing the unexposed photoresin, a polymer-QDs chain appeared, as shown in the inset of **Figure 2-20**(a) and the AFM image in **Figure 2-20**(b). This regular change in the size of the structure along the waveguide is exactly due to the energy exchange between the two modes of IEWs and TiO_2 layer. A morphology with a modulated thickness is observed. AFM measured thicknesses of the peak and the valley of this polymer-QDs chain were about (h_p = 64 ± 2 nm, h_v = 45 ± 2 nm) in **Figure 2-20**(c).

Interestingly, we found that the period of the polymer-QDs chain is 5.6 μm, which is different compared to our simulated value (BL = 2.3 μm with h = 80 nm) in **Figure 2-19**. This is probably due to three reasons. One is because the $Ti0_2$ was deposited not very nice and thus its refractive index is not the one from pure TiO_2. The sencond reason is the uncertainty on the refractive index distribution of our ion-exchanged waveguides which could have influenced the effective thickness and refractive index (cross-side) of this hybrid structure. In addition, during the photopolymerization process, the presence of the polymer resin might also alter the properties of the IEWs. Our previous works also have been done to analysis this phenomenon [120].

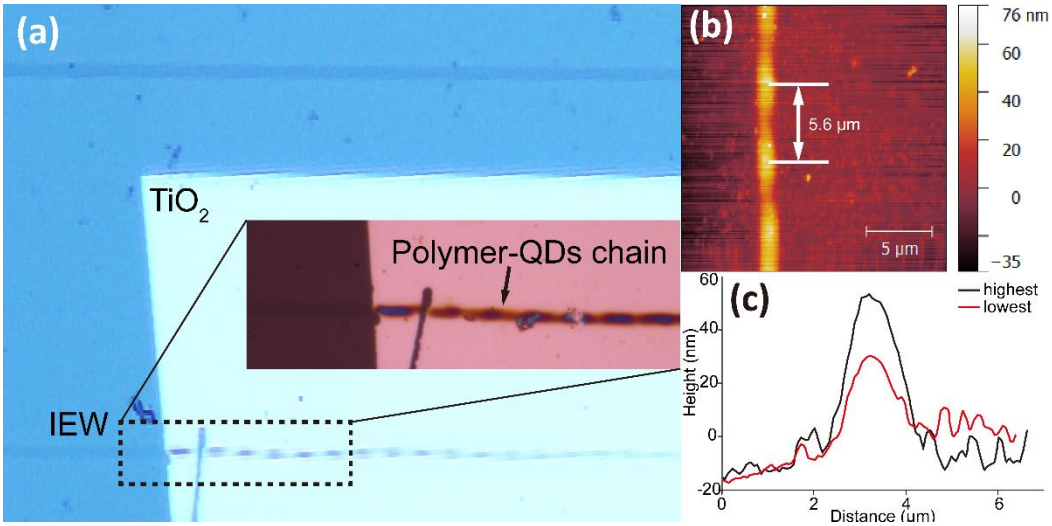

Figure 2-20 Results of the GEW experiment on the deposited TiO_2 layer on the IEWs. (a) optical micrograph of the TiO_2 slab on the IEW substrate, inset shows the enlarged details of the fabricated polymer-QDs chain; (b) AFM measurement of the same photopolymerized ridge on the polymer-QDs chain, showing a periodicity of 5.6 µm along the ridge; (c) cross-section profiles of the fabricated ridge indicating points with maximum and minimum thickness in red and black solid lines, respectively. (Images reproduce from [106])

2.5 Conclusion

In this chapter, nanoemitters based on polymer-QDs composites were fabricated on top of a photonic structure which are ion-exchanged waveguides using evanescent waves. A home-build photopolymerization set-up based on fiber-waveguide coupling system was used to carry on the experiments. Two kinds of photopolymerization experiments on IEWs and two-layer waveguide sample were conducted for producing polymer-QDs ridges. In the first experiment, two kinds of polymer-resin (with and without quantum dots inside) were used and were put on directly on the IEW surface. This was controlled via the excitation laser power and exposure time. That way, the size of the polymer-QDs ridges can be changed. PL measurement results indicate the

feasibility of our method. While in the second experiment, the polymer-resin was dropped on a TiO_2 slab which is deposited on the IEW surface beforehand which enable to excite the propagating mode of TiO_2 layer and make it easier for more propagating light in IEW couples into the TiO_2 layer. This was used for enhancing the photopolymerization and obtaining the polymer-QDs structures on desired positions. This has been demonstrated by our photoluminescence measurements at the positions with and without deposited TiO2 layer. The experimental results also show the 5.6 μm beat length of the two light propagation modes, which is also analysed by our simulated results. The results show the potential for producing luminescent polymer ridges on waveguides. In the future, we believe it is possible to create nanoemitters down to nanoscale with the help of a dielectric layer on top of plasmonic structures on our IEWs.

Chapter 3 Polymerized nanoemitters by Direct Laser Written – TPP

3.1 Introduction

Quantum emitters are one of the basic elements in the context of quantum devices, it is usually required that the dimension of the quantum emitters should be limited at a few tens of nanometers [121]. In this chapter, direct laser writing process based on two photon polymerization is used in order to scale down the dimension of the polymeric structures embedded with quantum dots, which paves a new way for deterministically integrating quantum emitters onto photonics devices.

A developed laser writing platform with a new configuration is proposed to expand its applications on thicker substrates. A thorough study of the fabrication parameters of the exposure laser was made in order to control the shapes and positions of QD-polymer nanostructures with high accuracy. This makes it possible to control quantity of QDs inside polymeric nanostructures, but also the QDs emission intensity. In addition, the substrates cleaning and the developing process were also optimized. The results prove its potential for applications on photonic chips. By using this developed method, we successfully transferred QD-polymer nanostructures on the surface of ion-exchanged waveguides. The far-field and waveguide-coupled quantum dots emission were detected by our homemade photoluminescence measurement set-up. Furthermore, FDTD simulated results of the coupling between quantum dots and waveguides have a good agreement with the measurement results.

3.2 Direct laser writing technique based on TPP

In this section, we introduce how we developed the configuration of the conventional laser writing platform for our specific needs. This is necessary for using IEW glass substrates on the platform. Moreover, in order to avoid the fluorescence influence from background, the cleaning process was also optimized.

3.2.1 Developed configuration of DLW-TPP

Standard DLW-TPP process is executed with a Nanoscribe Professional GT printer (**Figure 3-1**(a)) which is powered by a femtosecond near-infrared laser at 780 nm, operating with ~100 fs pulse duration and 80 MHz repetition rate and a maximum mean power of $P_{max} \approx 20\ mW$ (measured after the focusing objective) [122,123]. Photoresist is drop-casted on a 22×22×0.17 mm^3 transparent glass coverslip mounted on x-y-z piezoelectric translation stages imaged by a 100× immersion oil high resolution optical microscope objective, as shown in **Figure 3-1**(b).

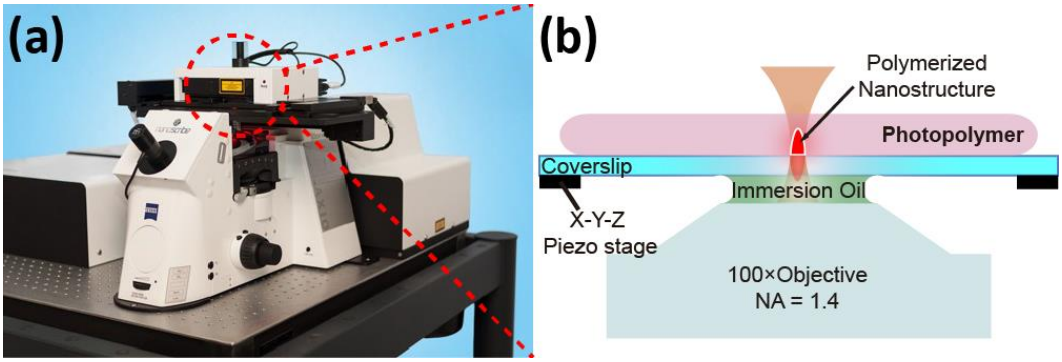

Figure 3-1 (a) Nanoscribe Professional GT printing platform; (b) Laser printing principle based on two photon polymerization.

In this conventional DLW-TPP configuration, a typical working distance of the oil immersion objective is less than 170 μm, which makes this approach to be used only for thin substrates. If one wants to use DLW-TPP on an another substrate containing waveguides in glass or a silicon on insulator (SOI) substrate, some developments are necessary in order to do DLW-TPP. Bückmann *et al.* proposed dipping the microscope

objective directly into a special photoresist material [124]. However, commercially available oil immersion-type microscope objectives are not designed for direct use with the photoresist material instead of the immersion oil. Moreover, diversity of substrate shapes and sizes limits its mounting to standard substrate holders. Thus, a need exists for developing a DLW-TPP configuration that can transfer QD-polymer nanocomposites onto thicker optical substrates, in our work, IEW-based glass substrates.

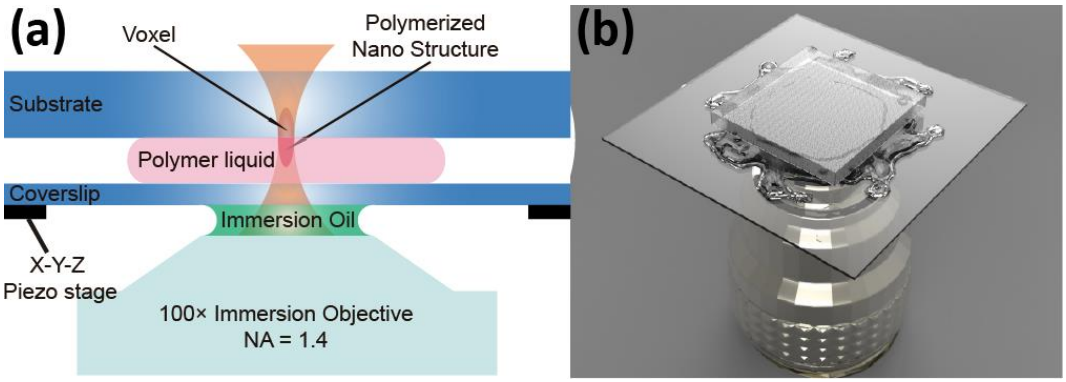

Figure 3-2 Schematic of the 'sandwich' configuration (a) and a silica substrate on a coverslip (b).

Creating a thin space between a substrate and a coverslip is a promising approach in order to use thicker substrates by laser writing system. In this case, the laser can go through the coverslips, and focus at the interface between the polymer liquid and the substrate (**Figure 3-2**(a)). As mentioned previously in Chapter 2, IEW substrates are fabricated based on the ion-exchanged technique with typical dimensions of ~ 10 × 10 × 3 mm^3, which is thicker than the working distance of the objective lens of the DLW-TPP system. For investigating feasibilities of different solutions, here, IEW substrates are replaced by silica substrates (10 × 10 × 1.2 mm^3) because of their similar optical transparent properties and refractive index (both are around 1.5).

We firstly attempt to put directly a face-down silica substrate on top of a coverslip with polymer liquid dropped on in advance (**Figure 3-2**(b)). However, the space distance starts decreasing with the polymer liquid spreading to the coverslip because of

the gravity. Considering the refractive index of coverslips, substrates and polymer liquids are quite near, a narrow space makes it difficult for the Nanoscribe system to identify the interfaces.

Secondly, we used thin plastic films as supports to create the space, as shown in **Figure 3-3**. The plastic films have a thickness around 50 μm and can be simply stuck on the coverslips, however, in the meantime, many bubbles are also produced. That makes the space thickness varying quite significantly. Moreover, the plastic films are not able to dissipate the static charge created on their surface, dust particles get attracted and often stick to the surface, which should be avoided for the fabricating process.

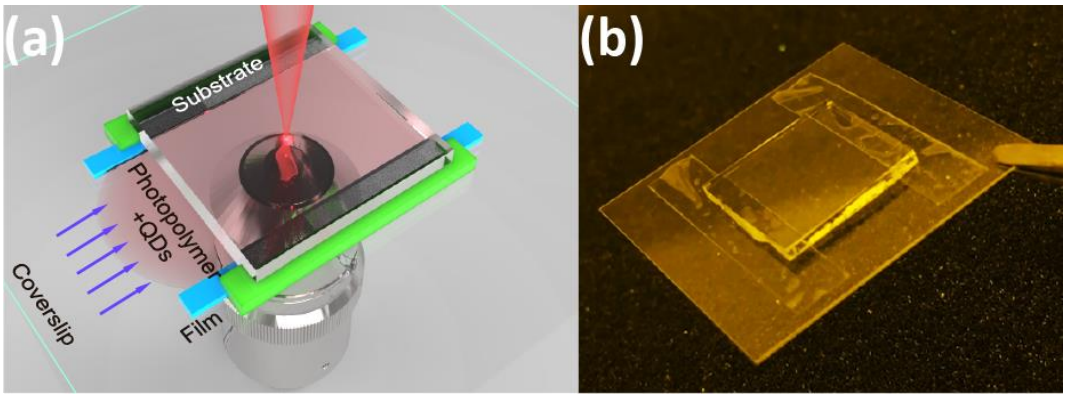

Figure 3-3 (a) Schematic of laser printing platform by using plastic film;

(b) A silica substrate supported by plastic films attached on a coverslip.

Commercial Tungsten metal is relatively inert, resisting attack by oxygen, acids and alkalis [125], therefore, to keep a stable space with a constant thickness value, the plastic films can be replaced by two tungsten microwires (Goodfellow. Ltd.) with 25 μm diameters, as shown in **Figure 3-4**(a). The micro-wires are placed parallel to the surface of the coverslip. The homemade photopolymer (PETA monomer) resist containing colloidal CdSe/ZnS quantum dots is placed into the space thanks to the capillary force of the narrow gap. Then the laser is focused at the interface between the polymer liquid and the substrate during the patterning process (**Figure 3-4**(b)). After the photopolymerization, the non-exposed part of photopolymer liquid is subsequently

removed in an acetone solution, resulting in a QD-polymer nanocomposite on the thick substrate.

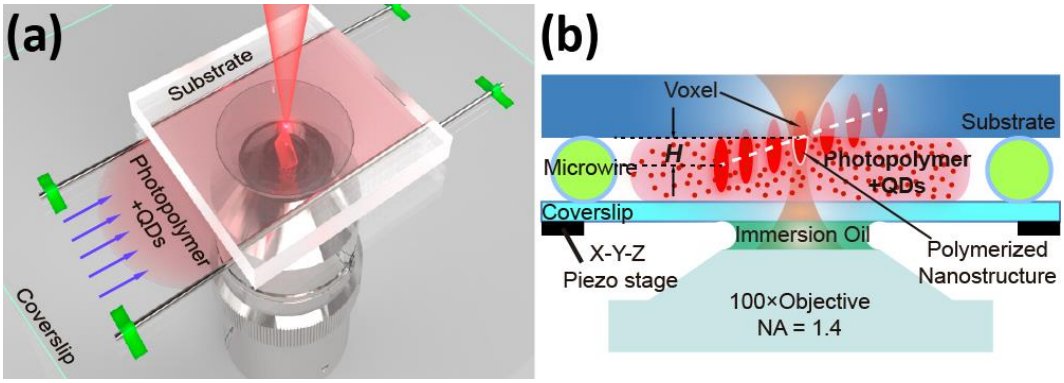

Figure 3-4 3D Illustration (a) and basic principle (b) of developed DLW-TPP platform.

3.2.2 Cleaning process optimization

The fabrication of devices using a polymer involve many processing steps starting with the preparation of the substrates prior to subsequent printing. It is mandatory to maintain cleanliness at each and every step of the unit steps involved in these processes, because the remnants which are left from the previous process steps influence the subsequent process steps and device properties. More importantly, the unremoved QDs on the sample surface also have strong fluorescence intensity which is higher than the emission intensity from few QDs inside our nanoscale polymer-QDs structures. As an example, **Figure 3-5**(a) shows the measured PL intensity of the polymer-QDs structure with unremoved QDs nearby. It seems that the emission intensity from the background is almost half of that from the structures, while this ratio obtained in a cleaner surface is less than 10% (**Figure 3-5**(b)).

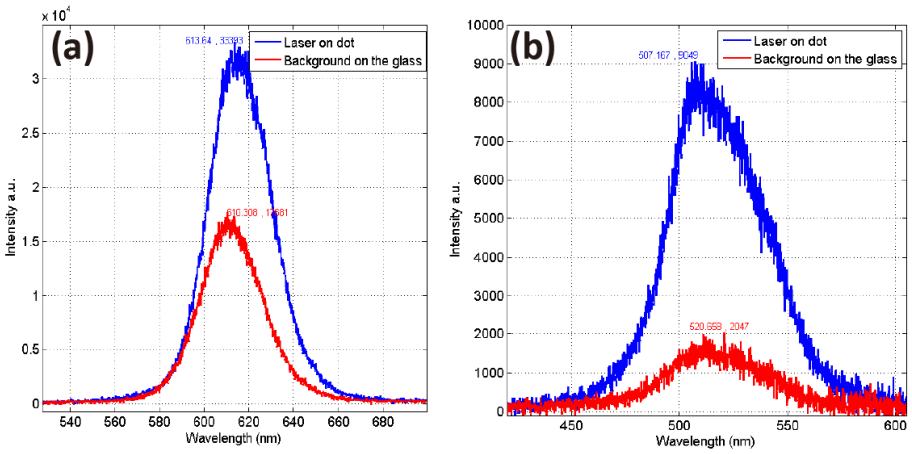

Figure 3-5 PL intensities contrast between sample with unremoved surface-attached QDs (a) and clean surface (b).

Firstly, for substrate preparation, we use two different cleaning processes A and B (**Table 3-1**) to clean the coverslips. **Figure 3-6** shows the AFM surface images of the coverslips using these methods. It is apparent that much more clusters appear on the surface handled with method A. Operating the cleaning process in a clean room and using ultrasonic bath enables us to obtain cleaner coverslips using method B.

Table 3-1 coverslips preparing-two cleaning approaches

Method / Steps	A	B
Clean room	×	√
Step-1	Rinsing with ACTN, IPA	Ultrasonic, decon90
Step-2	Rubbing by paper tissue	Rinsing by water
Step-3	Drying by air a blow gun	Ultrasonic, 5min ACTN, 10min IPA
Step-4		Hot plate, 80°C, 5min

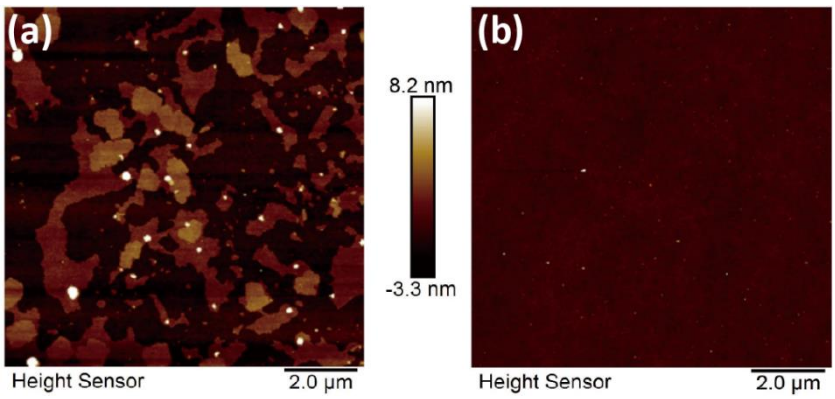

Figure 3-6. AFM images of coverslips cleaned by method A (a) and method B (b).

Secondly, after the coverslips are well cleaned and prepared, removing non-exposed parts of polymer liquid is necessary and crucial for a clean surface background. Unwanted polymer mass and quantum dots left on the surface produce photoluminescence noise stopping us from measuring the emission of single voxels which have comparable PL intensity. Acetone (ACTN) is a good solvent for dissolving two-part epoxies and superglue and cleaning plastic materials, oil and polymer resins before they harden [126]. Isopropanol (IPA) is the most suitable for removing contaminated acetone before it can form streaks and leave residues on the substrate [127]. As a secondary chemical, it also evaporates at a faster rate similar to acetone. The basic cleaning process is putting samples in ACTN for 10 minutes, followed by IPA with 10 minutes. The surface quality after developing is shown in **Figure 3-7**(a), as one can see, quantum dots can aggregate and attach to the surface due to their surface chemical properties. This makes it impossible to measure quantum dots emission precisely for these single voxels with some volumes.

To remove the quantum dots from the surface, we also use hydrogen chloride (HCl) solution ($pH \approx 3$) as an addition developing solvent between using ACTN and IPA. It has been demonstrated that the aggregates of quantum dots can be detached as the *pH* of the surrounding environment decreased [128]. Moreover, HCl liquid can also break the stability of the attachment between the QDs and the coverslip surface which

accelerates the quantum dots being removed. **Figure 3-7**(b) shows the SEM image of quantum dots distribution on the coverslip surface by adding the step of immersing in HCl solution of 10 minutes. The quantity of quantum dots remaining outside of the voxels decreases 43% according our area fraction calculation for the corresponding AFM images.

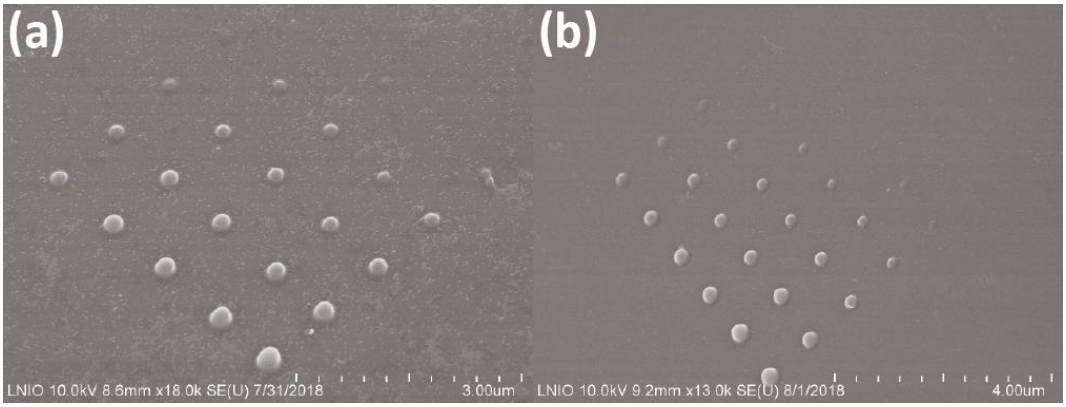

Figure 3-7 SEM images of coverslips cleaned without (a) and with (b) HCl solution.

Furthermore, optimizing the original polymer liquid formulation is another efficient approach for helping developing processes. Polymer liquids with different component proportions result in various chemical properties. Two formulations with different material proportions were prepared and drop-casted directly on the coverslips. The polymer resins stay on the coverslips for 10 minutes followed by the developing process described above. SEM and AFM measurement results of quantum dots distribution on surfaces are shown in **Figure 3-8**. According our area fraction calculation, the quantity of QD mass left on the coverslip in **Figure 3-8**(b, d) is decreased by 63% compared to that in **Figure 3-8**(a, c).

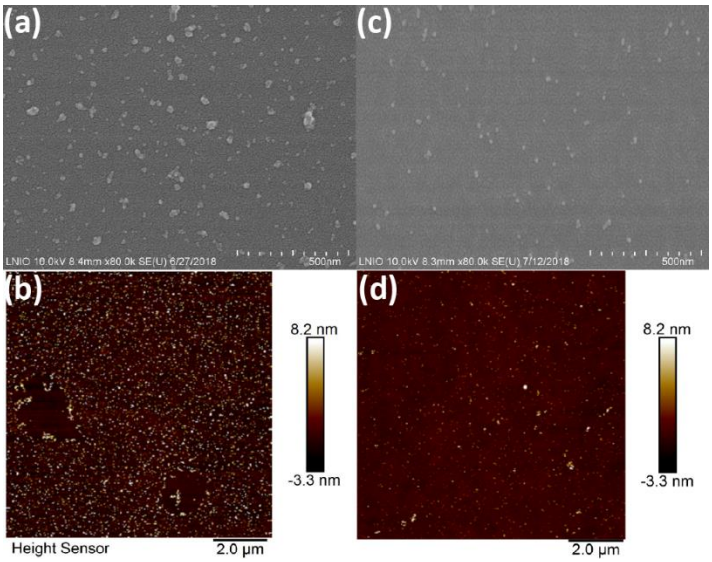

Figure 3-8 SEM images (a, b) and AFM images (c, d) of coverslips surface applied with two different formulations of polymer liquids, respectively.

3.3 Printing parameters study on glass substrates

Standard DLW-TPP has been widely used to fabricate 1D, 2D and 3D polymeric structures. Many researchers have analysed structure size scaling laws and study how to reduce the fabrication limit of the method. Previous works in our group have also been done to characterize the 2D and 3D QD-polymer structures. However, characterization of QD-polymer nanostructures fabricated by the developed DLW-TPP has never been studied. We also aim to fabricate QD-polymer nanostructures beyond the optical diffractive limit in order to isolate, in the near future, single quantum emitters within quantum devices,

In this subsection, we firstly present a full study of laser writing parameters on glass substrates by carefully adjusting laser power, exposure time and focus height during the printing process. The results make it possible to control the volumes of the nanostructures, as well as their PL intensity. In addition, the effects of QDs mass concentration in polymer liquids on the QDs quantity in QD-polymer nanocomposites has also been analysed. Next, this method can also be used on fabricating single layer of quantum dots. Finally, we investigated the possibilities for printing QD-polymer

nanocomposites on a silica substrate with a TiO_2 layer deposited on top of it for better coupling to a waveguide structure underneath.

3.3.1 Position and dimension control of nanostructures

The ellipsoidal-shape volume of the photo-polymerized resist inside the focused laser beam, called 'voxel', represents the ultimate resolution reachable during the DLW fabrication. Previous efforts for improving the precision of voxels by changing laser writing power *P* and laser exposure time *T* have been demonstrated on conventional DLW-TPP platform [129–131]. However, our specific DLW-TPP set-up is equipped with x-y-z translation stages enables us to realize the fabrication beyond the diffraction limit by controlling not only *P* and *T*, but also tuning the laser focal position (*H*) during the patterning process, as shown in **Figure 3-4**(b).

Before starting fabricating polymer-QDs structures on glass substrates, we firstly created markers on the glass surface using a micro-indenter, this step is for finding polymeric structures after the cleaning process. Nano/Micro indentation technique was developed to measure the mechanical properties and hardness of materials [132]. **Figure 3-9**(a) shows the schematic of the micro-indentation system. In a traditional indentation test, a hard tip (like diamond) is pressed into a sample surface, as shown in **Figure 3-9**(b). The load placed on the indenter tip is increased as the tip penetrates further into the specimen and soon reaches a user-defined value. At this point, the load may be held constant for a period or removed. A given load will make a smaller indent in a "hard" material than a "soft" one. **Figure 3-9**(c) shows the AFM image of indentation fabricated with a tip load of 30 *mN*.

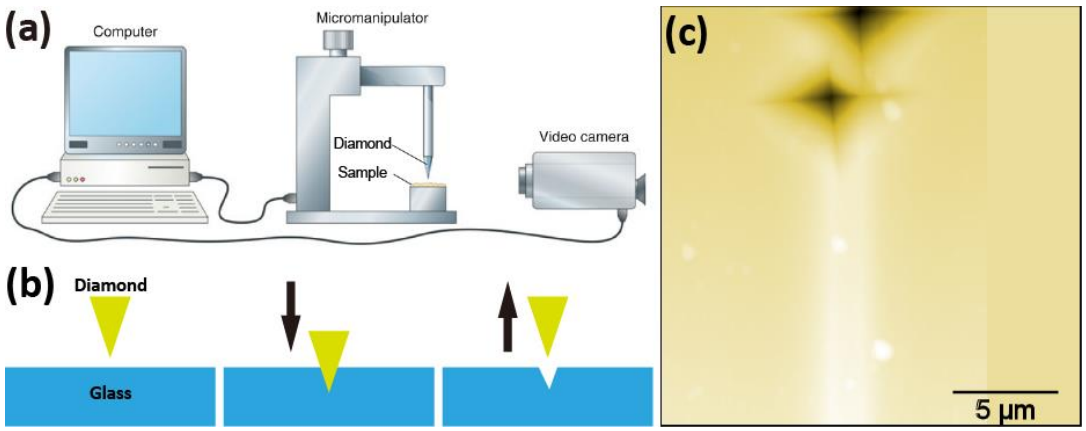

Figure 3-9 (a) Schematic of micro-indentation system. The diamond compresses the sample surface and the video camera helps visualize the displacement (Image reproduced from [133]); (b) The basic process of creating a small dent; (c) AFM image of fabricated dents with the load of 25 *mN*.

Figure 3-10(a) shows the microscope image of glass surface after creating markers. All the marks have the same shape of a four-pointed star and with a spacing of 50 µm. The glass substrate must be cleaned by ultrasonic bath to remove the glass slags produced after using the micro-indenter. All voxels were fabricated near the cross between the two lines made of markers. **Figure 3-10**(b) shows the dark field image of polymer-QDs voxels for different printing laser power (20-12 *mW*) and exposure time (1-3 *ms*). We can clearly observe that the size of these voxels decreases with shorter exposure time and smaller laser power.

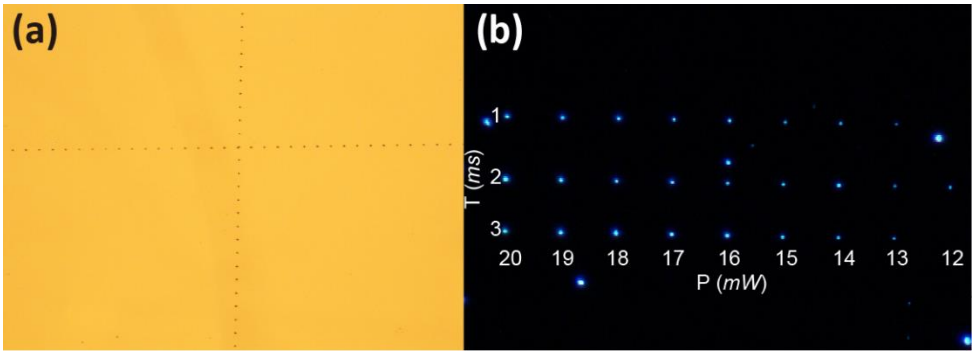

Figure 3-10 (a) Fabricated markers on glass substrate surface; (b) Dark-field image of polymer-QDs voxels.

We firstly systematically investigate the dependence of the size of the QD-polymer nanostructures by a fabricated array of 6 × 5 voxels (with pitches of 1 μm) on silica substrates while only adjusting *P* and *T*. **Figure 3-11**(a, b) show, respectively, scanning electron microscopy (SEM) and atomic force microscopy (AFM) images of the QD-polymer nanostructure voxels fabricated on the substrate. Clearly, by adjusting laser power and exposure time, the diameter and height of the voxels can be controlled with high spatial accuracy. The dependence of *P* on the voxel dimensions (diameter and height) is shown in **Figure 3-11**(c). Moreover, the relationship between voxel size with exposure time is shown in **Figure 3-11**(d). As expected, diameter and height decrease along with the decreasing of *T*. Consequently, this is an efficient way of controlling the volume of voxels by carefully adjusting *P* and *T* to control the amount of energy applied to the QD-polymer resin. The dimension of the voxel structures can be scaled down to ∼ 17 nm in height and ∼ 125 nm in diameter (with $P = 10\ mW$, $T = 1\ ms$), as shown in **Figure 3-11**(e, f). In this case, only few quantum dots are trapped inside the polymeric voxel considering that the average quantum dot diameter is typically around 4 nm. In addition, we also observed two QDs near the voxel that is might because they stick to the remained polymer near the laser focused area after DLW-TPP process. Smaller voxel can be fabricated with lower intensity of laser power and shorter exposure time, but it is hard to identify them. Meanwhile, the shape of the voxel starts to become irregular at the scale below 100 nm. However, it is still promising for creating the single QD by DLW-TPP process.

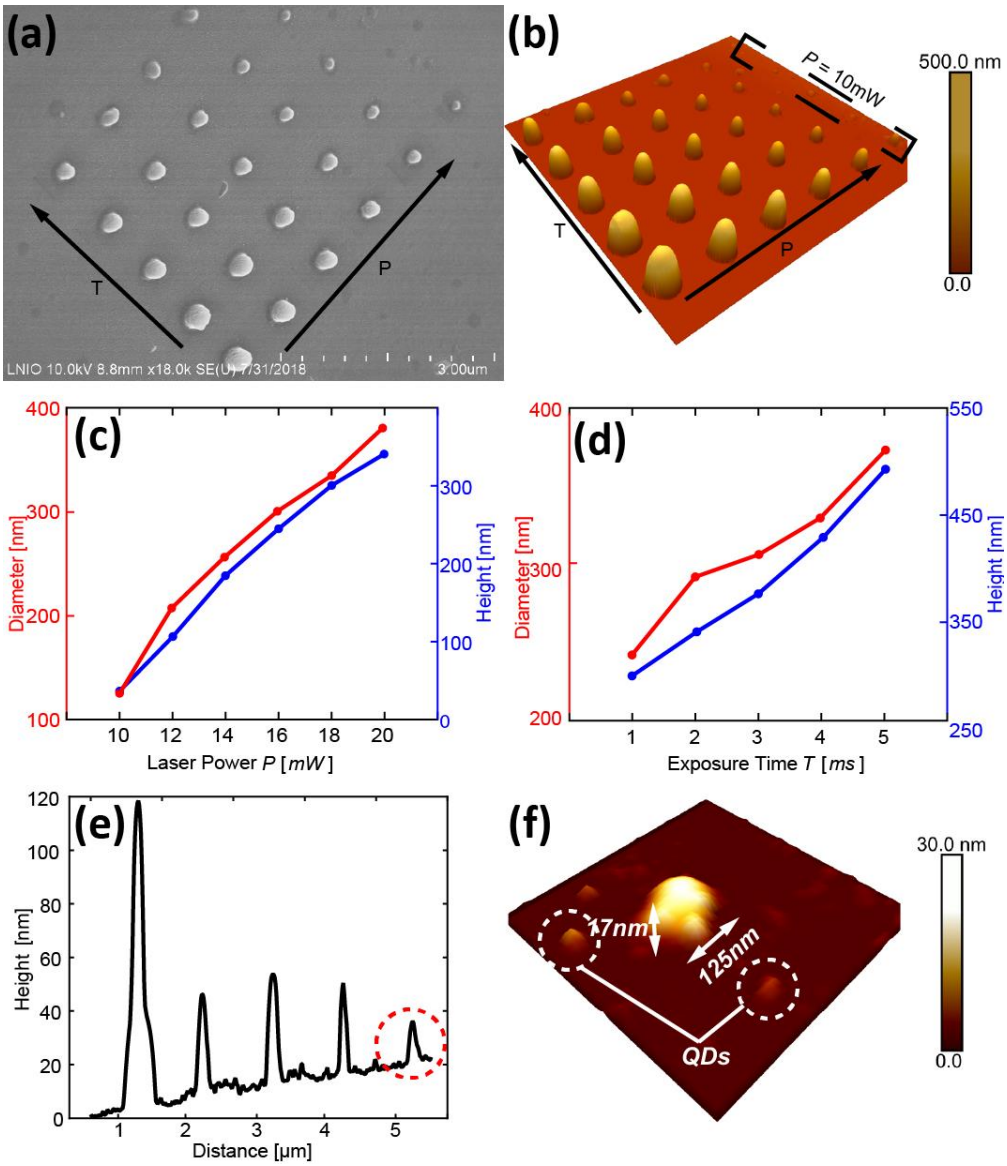

Figure 3-11 Characterization of QD-polymer voxels. Tilt-view SEM image (a) and AFM image (b) of a voxel array by changing laser power *P* (10 – 20 *mW* with a step of 2 *mW*) and exposure time *T* (1 – 5 *ms* with a step of 1 *ms*). The default value *H* in this sample is 0 nm; (c, d) Dependency of the height and diameter of single voxel structures as a function of *P*, *T* respectively. *T* = 5 *ms* in (c), *P* = 20 *mW* in (d); (e) AFM line profile of the QD-polymer voxels with *P* = 10 *mW*; The peak marked with red dashed circle indicates the profile of the smallest voxel, which is shown in the AFM image (not to scale) in (f) with *T* = 1 *ms*.

In order to verify the light emitting properties of the polymer-QDs voxels, we used a 404 nm laser to illuminate a single polymer-QDs voxel structure fabricated using 20 *mW* of laser power and 1 *ms* of exposure time. AFM and SEM analysis in **Figure 3-12**(a-c) reveal the diameter of 162 nm and the height of 84 nm. **Figure 3-12**(d) shows the emission spectrum of QDs inside of the single voxel with emission wavelength peak around 627 nm. The emission value of the single voxel (over 2000 counts) is much higher than the background light emission intensity (≈ 500 counts). We need mention that even though low QDs emission was detected from background, which means there are single quantum dots sticking to the surface outside the voxels, the results show that the feasibility of our integrating method for creating quantum emitters at a given position with high accuracy. This is another evidence that the we trapped the QDs inside the voxel structures at the position we desired. Forty repeated emission measurements for this voxel have been done to obtain stable, accurate as well as average spectrum. The average background emission value was calculated by measuring emission for 10 random positions around this voxel.

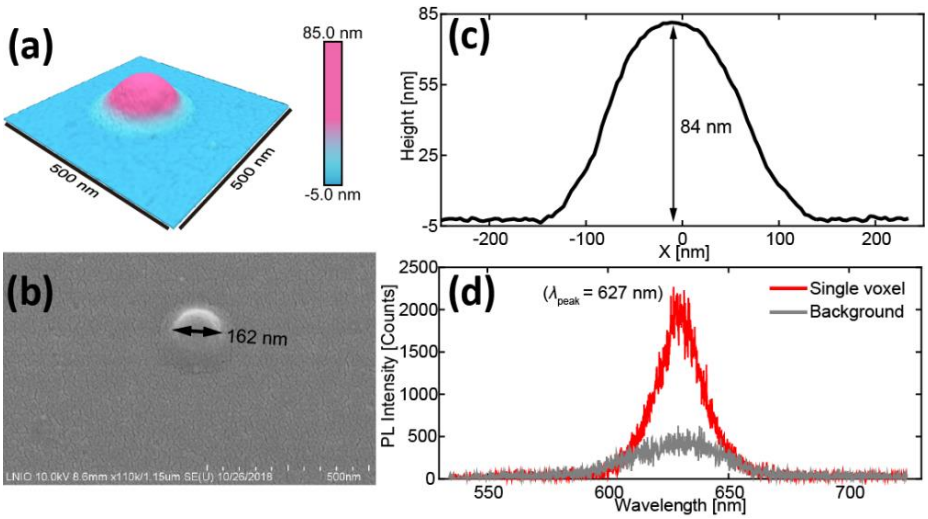

Figure 3-12 (a) 3D AFM image (500 nm scanning size) of a single voxel; (b) Tilt-view SEM image of the single voxel with diameter of 162 nm; (c) Height profile analysis of the single voxel; (d) Emission spectrum obtain by illuminating the single voxel with a 404 nm laser.

Secondly, the DLW-TPP equipped with x-y-z movement stages allows tuning the laser focal position *H* during the patterning process. This differs from adjusting laser power and exposure time by controlling the voxel size by changing the energy transferred into the voxel (see **Figure 3-13**(a) for a schematic). The height of the voxel can be decreased at a linear way, as shown in **Figure 3-1**(b) and **Figure 3-4**(b). Obviously, the polymer-QDs voxel could be formed out of the interface, which will result in the structures falling on the substrate (see insert of **Figure 3-13**(a)). By carefully adjusting *H*, we fabricated an array of QD-polymer voxels to investigate the possibility for further reducing the voxel size, as shown in SEM and AFM images (**Figure 3-13**(b, c)). The dependences of the voxel size on *H* is shown in **Figure 3-13**(d).

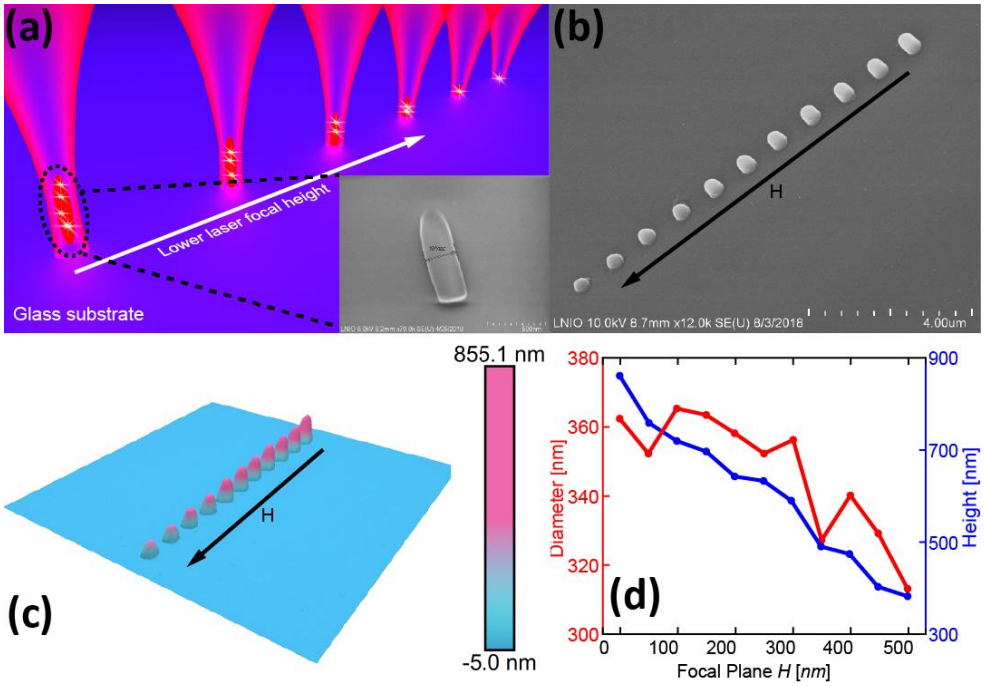

Figure 3-13 (a) Scheme of polymer-QDs voxel structures polymerized at different laser focal height on a substrate. Inset in (a) SEM image (top-view) of a voxel structure fallen down on the substrate; SEM image (b) and AFM image (c) of a single voxel structure array by only adjusting the laser focal height *H* (0 - 450 nm with a step of 50 nm, along the black arrow); (d) Dependency of the height and diameter of single voxel

structures as a function of *H*. 20 *mW* of *P* and 5 *ms* of *T* were used for the fabrication.

3.3.2 Single layer of quantum dots

Based on our results for characterizing QD-polymer voxels systematically, the quantity of QDs embedded in polymeric structures is highly related to its volumes which can be realized beyond the diffraction limit by our developed DLW-TPP platform. This allows us to create a single layer of quantum dots on a substrate by carefully adjusting the laser printing parameters during the DLW-TPP process. The SEM images of the QD-polymer lines fabricated with different laser focal height are shown in **Figure 3-14**.

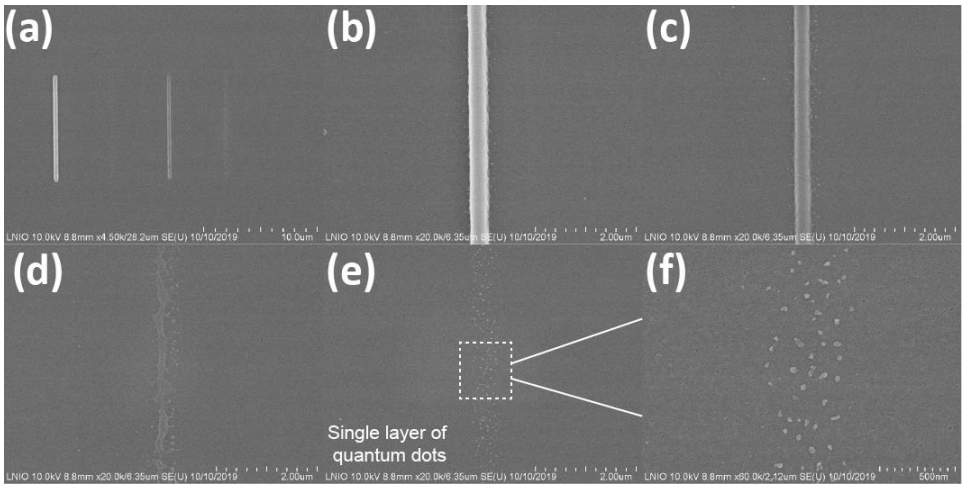

Figure 3-14 (a-e) SEM images of fabricated polymer-QDs lines with different thickness by controlling the laser printing parameters (*P*, *T*, *H*); (f) Enlarged SEM image of the white frame in (e).

Figure 3-15(a-e) show the 3D AFM images of these QD-polymer lines with different height. **Figure 3-15**(f) gives the measured height of each QD-polymer line. For the QD-polymer line showed in **Figure 3-15**(e), the measured height is around 15 nm, which is larger than the average size of quantum dots (typically 3-5 nm), but it is

clear that this is near the single layer of quantum dots. This probably is because the quantum dots are covered with a thin layer of polymer material. It has been demonstrated that the embedded QDs have similar optical properties as free quantum dots, moreover, the coated polymer can also protect the fragile quantum dots. This one-step depositing method is a promising way for creating single layer of quantum dots on many quantum devices in the context of hybrid light-emitting diodes (LED) devices, photonic crystals and optical lasing [134–137].

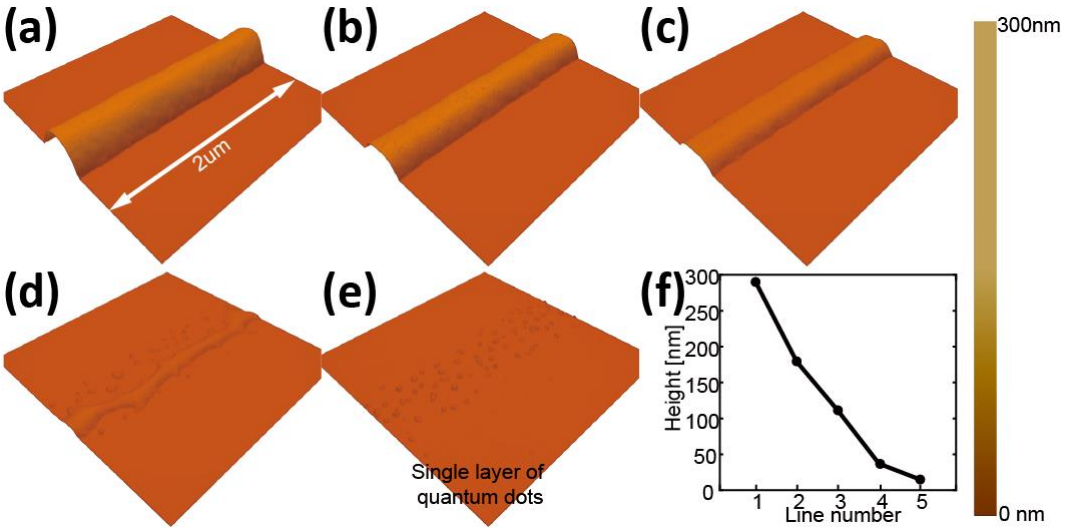

Figure 3-15 (a-e) AFM images of fabricated polymer-QDs lines with different thickness by controlling laser printing parameters (*P*, *T*, *H*); (f) AFM measured height of five QD-polymer lines.

3.3.3 Volume-related photoluminescence intensity

Due to the issues in quantifying the number of QDs inside of the voxels by SEM and AFM, and due to the importance in defining the fluorescence property of the QDs, we measured the photoluminescence emitted by each single voxel. Here we increased the distance between voxels from 1 μm to 5 μm, in order to avoid illumination from the neighboring voxels. **Figure 3-16**(a, b) show microscopy imaging of an array of single voxels. The exciting source is a blue LED (450 nm) within an ≈ 30 × 10 μm^2 field of view. The emitting light was filtered by a 530 nm long-pass filter (LPF) and recorded

by an Electron-Multiplying CCD camera. It is clear that without the filter the surrounding light due to the excitation is stronger than the photo-luminescence from the voxel, thus no PL can be recognized. However, when the filter is used, the camera does not get any light from the exciting source and bright points (**Figure 3-16**(b)) are clearly visible and correspond to the QDs emission from the voxels. The contrast between the two images reveals the light emitted by the QDs inside the polymeric voxels. It turns out that QDs can be trapped in the polymeric structures. Bright points with different intensities are clearly visible and correspond to the quantum dot emission from voxels with different volumes.

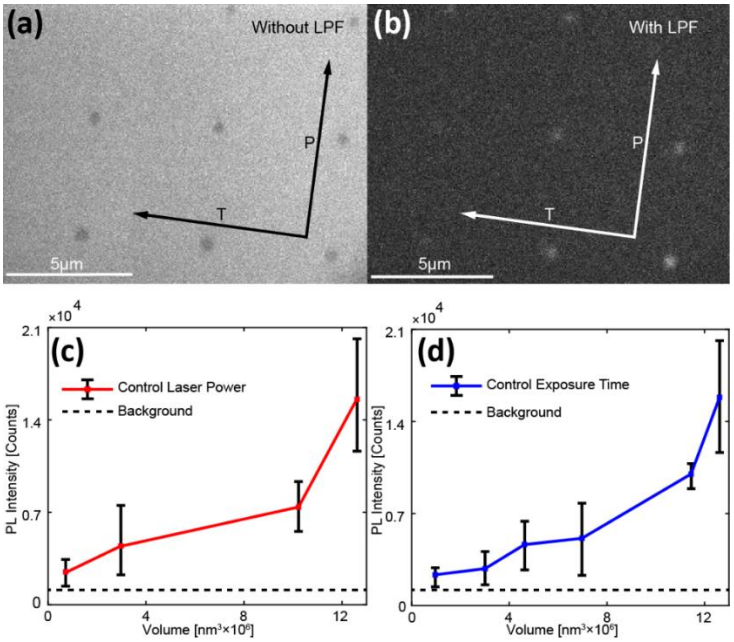

Figure 3-16 CDD images of the voxel matrix illuminated by a 404 nm LED without (a) and with (b) a 530 nm LPF; Relationship between QDs emission and volume of voxel by adjusting *P* (c) and *T* (d). Dashed lines represent the background emission.

Figure 3-16 (c, d) show the PL intensity mean values as a function of laser power (red line) and exposure time (blue line). Here, the volume of a single voxel could be calculated by $V = (4\pi hd^2)/3$, with *d* and *h* represent the diameter (by SEM) and the

height (by AFM), respectively. It is obvious that the emission of the QDs inside the voxel would decrease with the voxel volume. As we can control the size of the voxels at will, we can therefore control the number of quantum dots inside a given voxel. From the images, it is clear that the PL/volume dependency has a specific non-linear relationship. We suppose that this is due to the effect of the presence of the QDs inside the resin. In addition, all voxels were fabricated near the optical diffractive limit, this is different from the situation at large scale.

Additionally, the effect of QDs mass concentration in the photopolymer liquid far field PL intensity was also investigated. We made three polymer liquid formulations with different QDs mass concentrations (C = 3.6 mg was the original QDs solution dispersed in 1 g PETA solution and giving rise to C_1 = 1.8 mg/g, C_2 = 0.9 mg/g). We fabricated the voxel matrices on coverslips by using the same laser parameters (laser power 10 - 20 *mW*, exposure time 1-5 *ms*, shown in **Figure 3-17**(a-c) for the three formulations and select voxels which have similar volume from each sample in order to analysis the emission difference between them. Here, we need to mention that the actual laser energy transferred to the voxels varies with different polymers, thus we select 10 voxels fabricated with 1.5 *ms* in C, 2 *ms* in C_1 and 4 *ms* in C_2. The average volume is about 2.65×10^7 nm^3. 40 repeated emission measurements with same measurement parameters for each selected voxel have been done to obtain stable, accurate as well as average spectrum. As can be seen in **Figure 3-17**(d), the QDs emission from voxel structure decreases as the QDs mass concentrations decreases. It is a promising way to obtain few or even single quantum dots inside a single polymeric voxel.

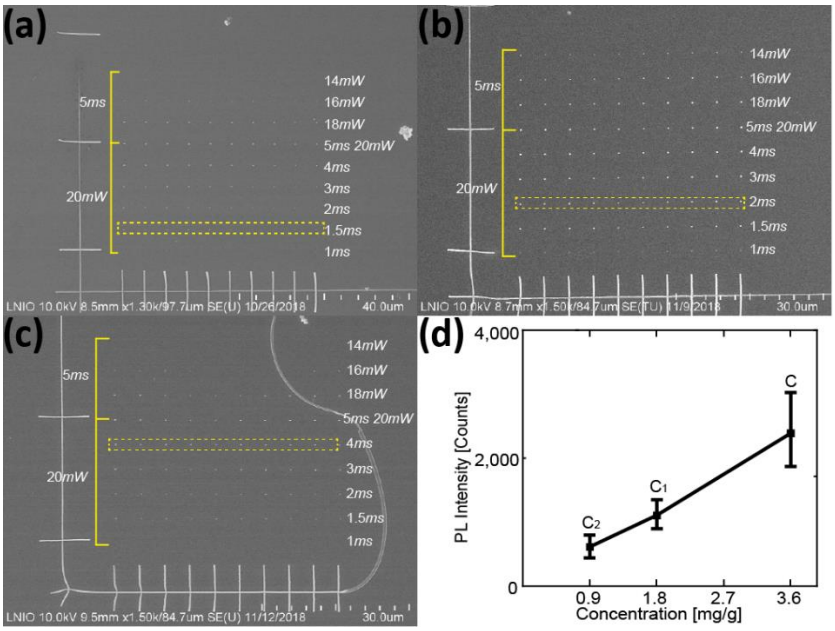

Figure 3-17 SEM images of voxels arrays fabricated with different polymer liquid formulations with the QDs concentration of C (a), C_1 (b), C_2 (c); (d) Dependence between QDs concentration with far field PL of QDs-polymer voxels.

We point out the potential of this control for the practical integration of single QDs into these polymer nanostructures that can be positioned onto optical chips by simply changing the voxel volume, specifically by adjusting *P*, *T*, *H* and as well as the QDs concentration. The results demonstrate the possibility of this method for fabricating polymer-QDs nanocomposites beyond the optical diffractive limit not only in the lateral, but also in the longitudinal direction.

3.3.4 QD-polymer nanocomposites integrated on TiO_2 surface

In order to explore the possibility of integrating polymer-QDs nanocomposites on different substrates, as an example, we attempted to apply our method on a silica substrate with a thin layer of TiO_2 deposited on top. We firstly clean the silica substrates according to the cleaning procedures we optimized, and then a thin layer of TiO_2 with the thickness of 150 nm was evaporated onto it using a PLASSYS MEB 400 evaporator with a speed of 0.15 nm/s at ~ 10^{-6} mbar. Next, the substrate was moved to the laser

writing process, and a polymer-QDs voxels array was fabricated on top of it, as shown in **Figure 3-18**(a). Interestingly, a second smaller voxel was observed to have grown on top of the first voxel for high laser power and long exposure time. We called these structures 'snowman'. We repeat this experiments by decreasing the distance between voxels, and we found the similar phenomenon as well, more interestingly, there are also bridges produced between neighboring voxels because of the points printing mode used on the Nanoscribe system. That is because the laser energy is not fully attenuated when finishing one position (**Figure 3-18**(b)). Here, we attribute the 'snowman' to the reflection of the Gaussian laser beam, as shown in the principle in **Figure 3-18**(c). The excitation laser transmit through the coverslip and polymer resin, then is focused on the substrate surface, and because of the high refractive index of TiO_2, the laser can be reflected and refocused on the same side, a second polymer 'voxel' is formed eventually. By carefully controlling the energy dose, we can also realize a polymer-QDs nanocomposites chain, shown in **Figure 3-18**(d). This could be a good example for fabricating chain polymer waveguide in the future.

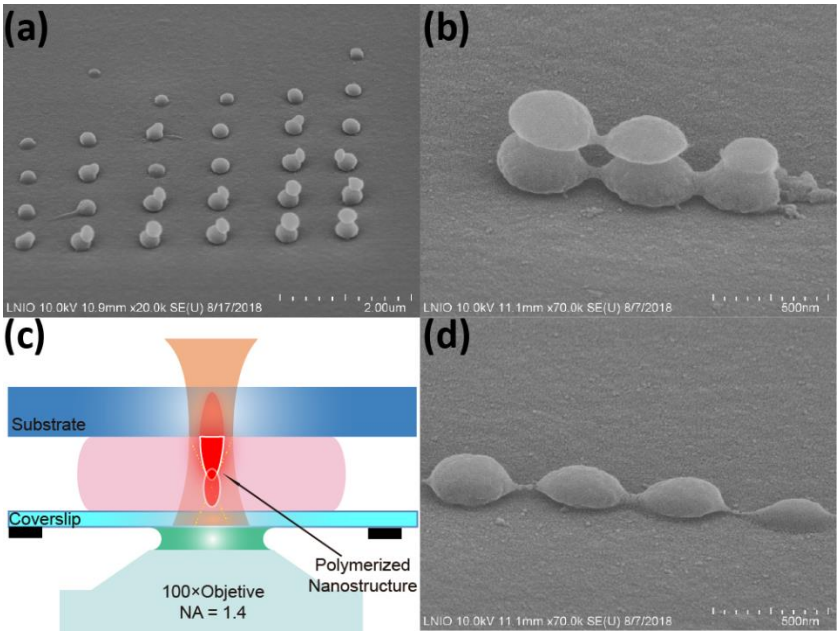

Figure 3-18 (a, b) SEM images of fabricated polymer-QDs voxels on TiO_2 layer; (c) The second voxel volume formed by the reflection of Gaussian laser beam; (d) Voxels array with a 500 nm period.

3.4 Nanoemitters integrated on IEWs

As we are able to control positions and dimensions of polymer-QDs nanocomposites on glass substrates, we wanted to explore whether the IEW could be used as a photonic channel for integrated nanoemitters. **Figure 3-19** shows the schematic of this application. Based on the optimized laser writing technique, we succeeded in creating nanoscale polymer-QDs composites at the center of an IEW surface. By exciting the integrated nanoemitters with an external laser, we obtained the emission at the end of the waveguide which showed the evidence of a waveguide-coupled QDs emission. The results demonstrate the possibility of integrating nanoemitters by using laser writing technique based on TPP.

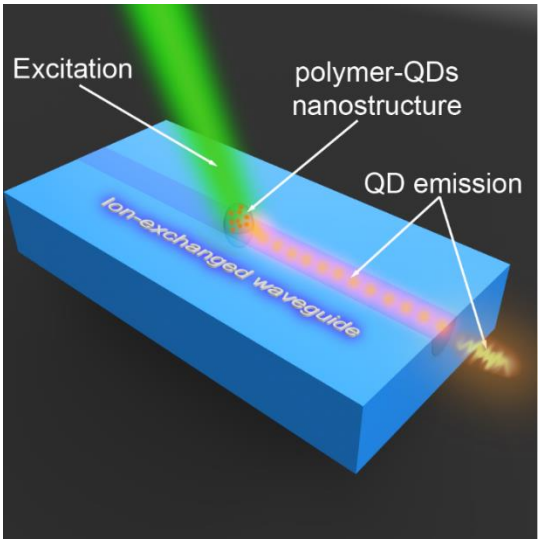

Figure 3-19 Schematic of waveguide-integrated polymer-QDs nanoemitters.

3.4.1 Fabricated QD-polymer nanocomposites on IEWs

Based on the empirical printing parameters, we fabricated polymer-QDs nanocomposites on IEWs. As shown in **Figure 3-20** (a), we fabricated voxels along the waveguide by decreasing the exposure time from 20 *ms* to 16 *ms* (top to bottom). **Figure 3-20**(b) shows the details of the part in white frame. Clearly, all these polymer-QDs nanocomposites are located at the center of the waveguides. The results show the

precise control of position and size of voxels. This ensures an efficient emission coupling from QDs into IEWs, the importance of voxels position will be discussed in the next section.

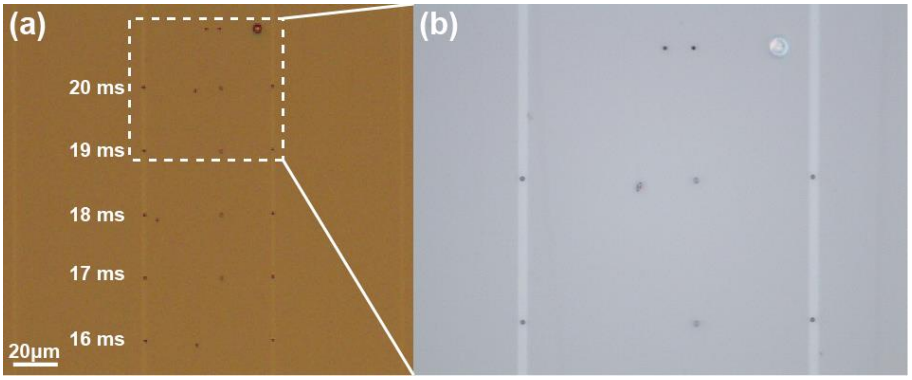

Figure 3-20 (a) Microscope image of polymer-QDs voxels integrated on IEWs; (b) Enlarged details inside the white frame in (a). The laser power is fixed at 20 *mW*.

In fact, during the PL measurements, only one polymer-QDs voxel should be created on each waveguide, that is because when one voxel was excited by the laser, the waveguide-coupled QDs emission could be scattered by other voxels on the same waveguide. In order to verify this, we experimentally coupled a 627 nm red laser (considered as QDs emission) into the waveguide, as shown clearly in **Figure 3-21**, the light is scattered to free space by a voxel, the propagating light intensity inside waveguide decreases a lot from the voxel position onwards. The QDs emission has almost completely leaked out of the waveguide and make it impossible to measure the signal at the end of the waveguide.

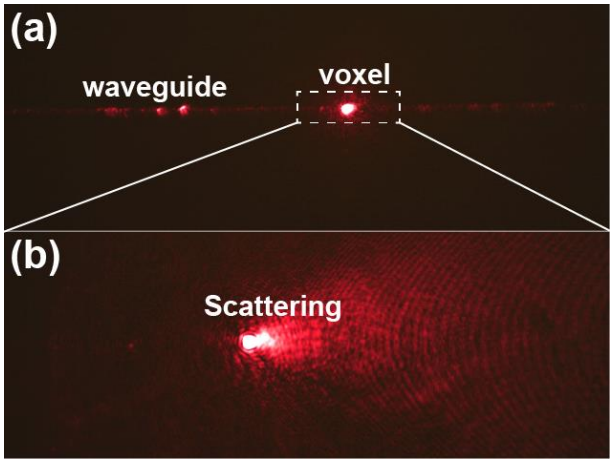

Figure 3-21 (a) 627 nm red laser scattered by a polymer-QDs voxel on one waveguide; (b) Enlarged details inside the white frame in (a).

Thus, three nanoscale polymer-QDs voxels (exposure time of 3 *ms*, 2 *ms* and 1 *ms*) were created on different waveguides shown in **Figure 3-22** (a) and (b). The printing laser power used for photopolymerization was 20 *mW*. **Figure 3-22** (c) and its inset show the details of the voxel with 1 *ms* exposure time.

These were the voxels created for the scattering measurement. We could have created a smaller voxel with lower printing laser power. However, considering the quantity of QDs would decrease, resulting in lower intensity of QDs emission, it would have made it more difficult for us to measure with our current experiment system shown in the next subsection.

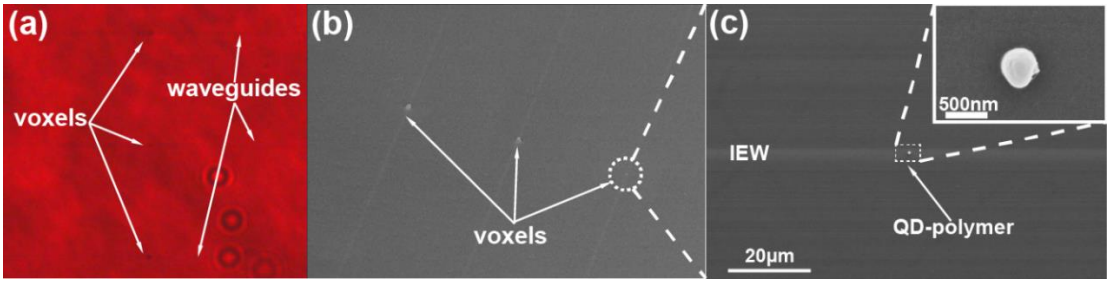

Figure 3-22 Integrated three polymer-QDs voxels on different waveguides as shown in microscopy image (a) and SEM images (b, c).

3.4.2 Fiber-chip coupled PL measurement setup

A home-built photoluminescence measurement set-up was used to detect the quantum dot emission coupled to the IEW, as shown in **Figure 3-23**(a). A 617 nm LED light source below the sample stage allows individual devices to be imaged. The input single mode fiber (Thorlabs-630HP, mounted on a x-y-z piezoelectric stage) is aligned at the end of the corresponding waveguide facet with a 640 nm continuous laser to optimize the fiber-IEW coupling. Some of the alignment light is scattered out of the waveguide plane. The spatial distribution of light intensity along the waveguides is projected onto an CCD camera and this allowed us to observe light propagation and to pre-align our waveguides to the optical fiber. Once the input fiber is properly aligned, the sample is excited from top simultaneously by switching the excitation laser to 532 nm through a 60× microscope objective (Numerical Aperture NA = 0.9). The QD emission coupled to the IEWs is collected and detected by a CCD-cooled grating spectrometer. The far-field QD emission can also be collected by a multimode fiber and directed through a 540 nm long-pass filter towards another commercial portable spectrometer (Ocean Optics, QE Pro).

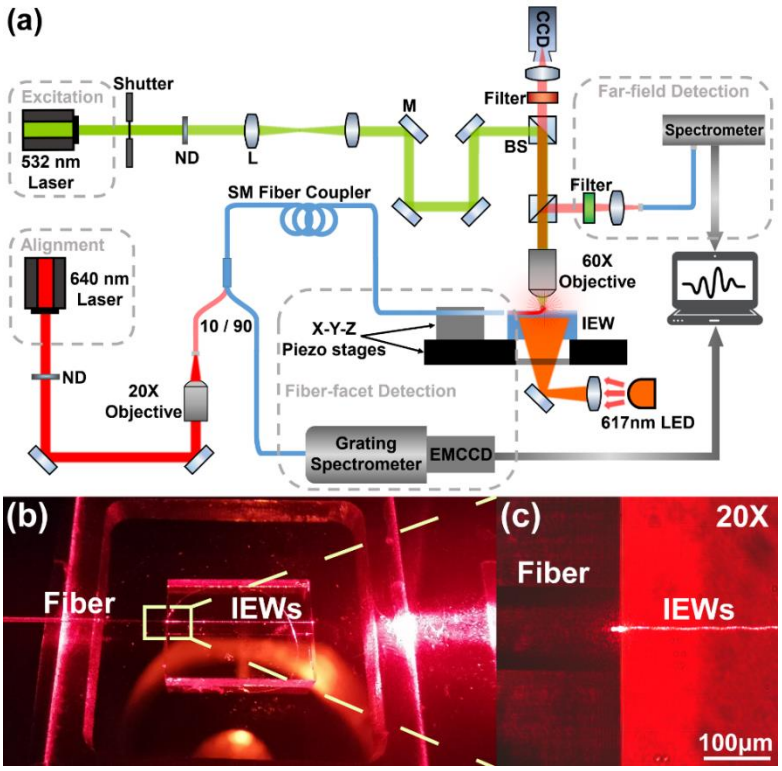

Figure 3-23 (a) Experimental fiber-IEWs coupling stage; (b) Fiber tip coupled with the edge of IEWs; (c) Enlarged part of the yellow dashed square in (b).

Pre-alignment of fiber and waveguide ensures we are able to measure the QDs emission from the waveguide facet. The external 640 nm CW laser is focused into a fiber, then coupled into the IEW. Fiber-waveguide coupling is achieved by adjusting the position of the fiber tip via piezo electric translation stages. The leakage of the propagating light makes it possible to optimize the coupling visualized by our microscope system. **Figure 3-23**(b) shows the experimental fiber-waveguide sample coupling stage, the red light line on IEWs sample surface indicates the propagated 640 nm laser indicative of a coupling efficiency. **Figure 3-23**(c) shows the enlarged microscopy image for the yellow dashed square in **Figure 3-23**(b). No scattered light between the fiber and the IEW is observed when the optical fiber mode and the ion-exchange waveguide mode overlap well. At the position of QD-polymer voxels on the waveguide integrated far away from the waveguide input facet, a clear light spot is observed due to the guiding laser scattered by the structure. This helps us optimizing the fiber-to-waveguide alignment, as described in **Figure 3-21**(b) in section 3.4.1.

3.4.3 IEW-coupled QDs emission measurements

After optimizing the fiber-waveguide coupling, next, we switched from the red laser to the green laser (532 nm). Firstly, we check the emission of the QDs by far-field detection. The voxel shown in **Figure 3-22**(c) was used for the PL measurement. A significant far field QD emission was observed in **Figure 3-24**(a) (red emission spot, filtered by a 540 nm long pass filter). The results show the evidence of the presence of quantum dots inside the polymer nanostructures and their high emission quality. The recorded spectrum shows an apparent peak at 588.5 nm with a FWHM of about 43.1 nm, which is indicative of our CdSe/ZnS QD-like emission signatures, as shown in **Figure 3-24**(b).

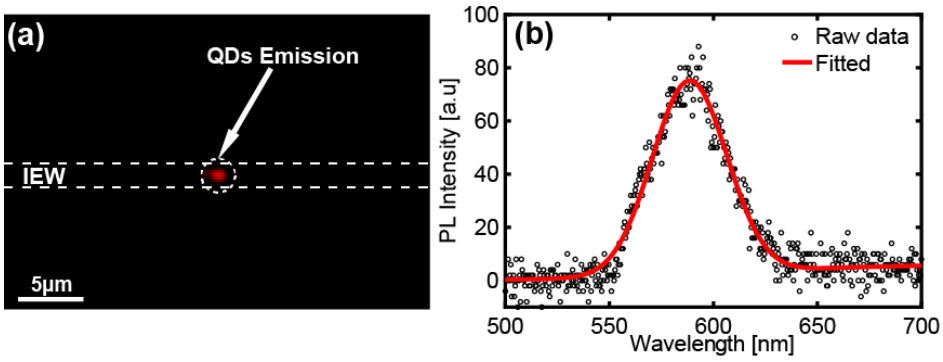

Figure 3-24 (a) CCD image of QDs emission (red spot), white dashed line represents the outlines of the waveguide; (b) Spectrum of the far field quantum dots emission for a single QD-polymer nanostructure on IEW with a Gaussian fit (red line).

Next, we measured the waveguide-coupled QDs emission by fiber coupled detection. The result shows the extracted spectrum which gives rise to a narrow luminescence peak at 591.1 nm with a FWHM of about 8 nm as presented in **Figure 3-25**. The wavelength at maximum intensity is in very good agreement with the far field spectrum. The spectra with high intensity between 500-560 nm represents the 532 nm excitation laser. In fact, as shown in Fig. 4(c), the intensity of waveguide-coupled QD emission is relatively low compared to the signal of the propagating excitation laser (532 nm). Putting a long-pass filter at the end of the waveguide has been tried for cutting the excitation laser, but this also reduces part of the QD emission (590 nm) which makes difficult to detect the signal and obtain the PL image at the facet of waveguide. And the broad spectral emission between 600-700 nm arises from the fluorescence from the IEW substrates which is verified by the measured PL spectrum performed on a bare IEW without QD-polymer nanostructure, as plotted in grey solid line.

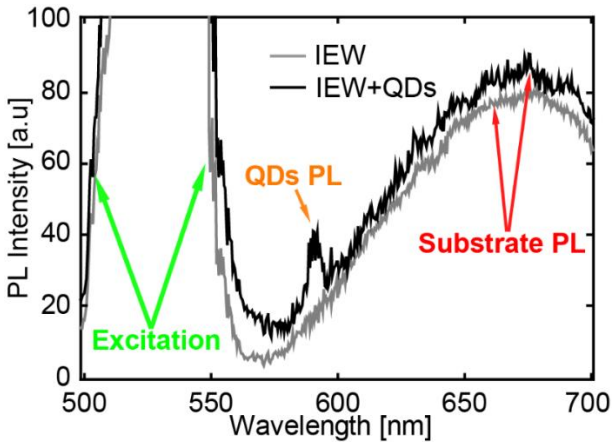

Figure 3-25 Normalized extracted spectrum collected from waveguide facet by a single mode fiber. Black line for QD-polymer nanostructure placed on IEW while grey line for IEW without QDs on top.

Interestingly, there is a strong discrepancy of the PL spectrum FWHM between QD emission into the far field and into the IEW. This discordance is related to the dissimilarities in the PL measurement conditions. The IEW guided mode has its energy density maximum underneath the surface. Because of the evanescence of the guided mode above the glass surface [138], it is expected that the QD-waveguide coupling efficiency decreases exponentially from the surface to the center of the polymer nanostructure. As our quantum dots dispersed randomly inside the polymeric nanostructures, the coupling efficiency is strongly related to the QD's positions. Thus it is necessary to analyse the effect of QD's position on the coupling efficiency. To estimate the coupling efficiency between the embedded QDs and the IEW, we simulated the mode propagation in the IEW using finite-difference time-domain numerical simulations. We approximate the quantum dots emission with a x-oriented electric dipole source radiating inside the polymeric structure with the shape of a semi-ellipsoid on the IEW. We fix the diameter of the voxel at around 500 nm and the height at 500 nm. We assume the refractive index of the polymer is around 1.57. The total emitted power carried by the fundamental TE mode supported by the IEWs were

collected through a power monitor at a waveguide's cross-section. In fact, the QDs emission propagates along two directions (-y and +y). Considering the same situation for both, we only calculate the coupling for one direction.

Figure 3-26(a) show the coupling efficiency as a function of the QD position shifting along the x-axis. The coupling efficiency decreases slowly because the gradient refractive index of the IEW changes. The result shows around 0.22% coupling efficiency for the optimized QD position (at the center of the guide, attached on surface the of IEW). **Figure 3-26**(b) shows the dependence along the z-axis of the QD's position with the coupling efficiency, which has a near exponential relationship similar to the electric field distribution at the interface. We should mention that in our work, QD-polymer can only be integrated on the substrate surface, in fact, the IEW has its maximum electric field intensity inside the guide (0.52 µm below the surface). Coupling efficiency could be increased to 2.5% (10 times higher than from surface) by simulating a QD located at this position.

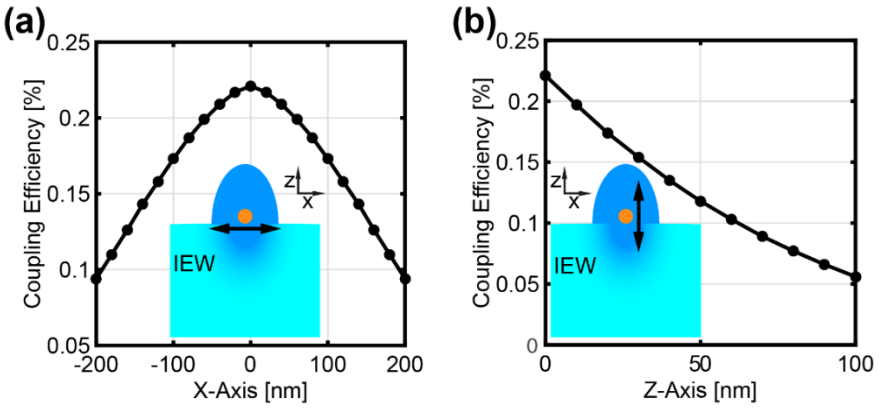

Figure 3-26 QD-IEW Coupling efficiency as a function of QD position shifting along (a) x-axis and (b) z-axis.

As a consequence, only few to even one single quantum dot is localized at very short distances from the waveguide interface might be efficiently coupled to the waveguide. On the other hand, far field emission is collected from an ensemble of quantum dots embedded into the polymer voxel. This certainly causes an

inhomogeneous broadening of the collected emission line shape [139–141], resulting in the broad quantum dot emission peak in **Figure 3-24**(b).

Here, we investigate the size distribution of our quantum dots and the dependence in the emission. Quantum dots are semiconductor materials and their emission wavelengths are determined not only by their material composition but also by their dimensions (size and shape) [142]. As a result, the ensemble PL spectrum of a QD-polymer nanocomposite is defined by the convolution of the average emission of the individual QDs and the size distribution of the QDs in the nanostructure, as schematically depicted in **Figure 3-27**(a). In order to demonstrate this mechanism, we simulated the total transmission of an IEW coupled with an ensemble of QDs inside a polymeric voxel, shown in **Figure 3-27**(b). Here, 11 dipole sources with different polarizations and different emission wavelengths (ranging from 540-650 nm, with FWHMs about 7 nm) were placed randomly inside a polymer voxel. The fitted total transmission spectrum has 2 dominant peak at 588.6 nm and 565.8 nm because these two dipoles are quite near the center at the interface. For this reason, in **Figure 3-24**(b), the PL broadening of far field QDs emission might be accounted for the inhomogeneous distribution of QDs size. Furthermore, by carefully controlling the patterning laser focal height *H*, a thin layer of QD-polymer with a thickness close to the thickness of a single QDs layer was created, as shown in **Figure 3-27**(c), which measured with the same sample as **Figure 3-14**(e). **Figure 3-27**(d) is the corresponding histogram exhibiting the size distribution of CdSe/ZnS QDs on a glass substrate. Therefore, in our work, the emission spectrum collected from few QDs coupled into the IEW has narrower PL line width than the far field ensemble spectrum, which is characterized by a broad PL line width. This demonstrates the fact that only few to a single QD emission in the voxel and near the surface of the ion-exchange waveguide is coupled into the guide thus leading to a narrower linewidth.

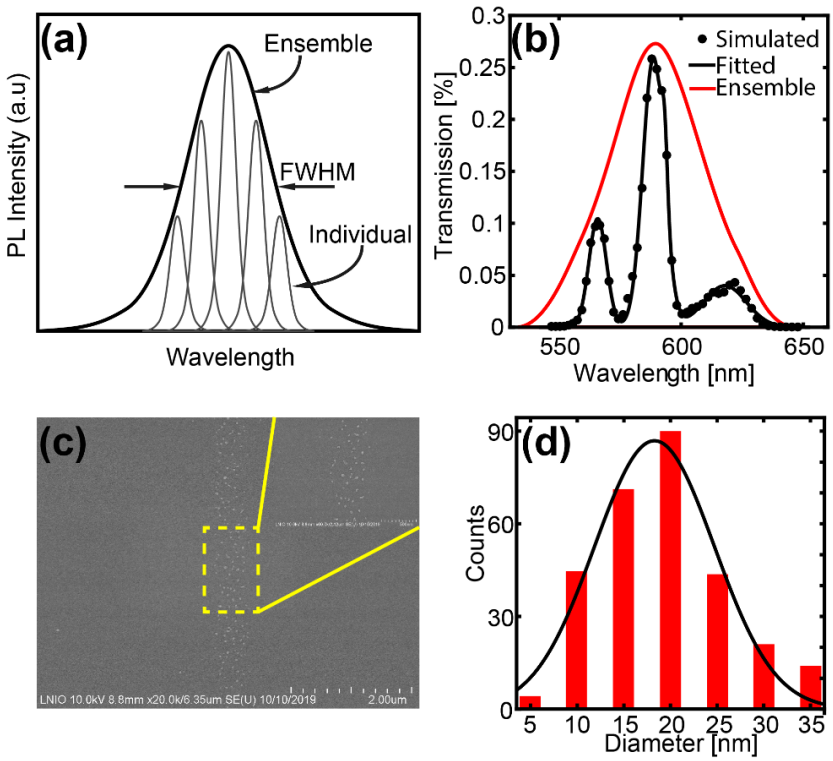

Figure 3-27 (a) Schematic of an ensemble PL spectrum consisting of the individual QD emission spectrum convolved with the interparticle inhomogeneities; (b) Simulated ensemble transmission spectrum for 11 QDs emission coupled into IEW; (c) SEM image of a single QD layer of the QD-polymer nanocomposite; (d) Corresponding histogram with fitted curves (black line), representing the size distribution of QDs on a glass substrate.

Moreover. This single layer of QDs shown in **Figure 3-27**(c) can also be used as for calculating the QDs density distributed inside the polymer. This enable us to estimate the quantity of QDs dispersed inside the QD-polymer voxels and which is helpful for creating single QDs and realize the single photon nanoemitter.

The calculation can be separated two parts. The first step is calculating the QDs density inside polymer composites:

The QDs density distributed inside polymer can be calculated by:

$$D = \frac{N}{V} \tag{3-1}$$

N is the total number of QDs dispersed inside the polymer composite, and *V* represents the volume of the polymer composite. The AFM (**Figure 3-15**(e)) and SEM (**Figure 3-27**(c)) measurement results show the single layer of QDs has the length of 5 μm, 500 nm in width and 15 nm in height. Thus the calculated volume is around 3.75×10^7 nm^3. And the total number of QDs is around 335 according the measured quantity of QDs shown in **Figure 3-27**(d). Therefore, the calculated QDs density is around $8.93\times10^{-6}/nm^3$ by equation (2-1).

The second step is calculating the QDs number inside the QD-polymer voxels. As already mentioned in section 3.3.1, the voxel has a shape of semi-ellipsoid. So the volume of the voxel can be calculated by the equation below:

$$V = \frac{2\pi}{3} hr^2 \tag{3-2}$$

Where *h* indicates the height of the voxel, and *r* is diameter. As an example, we calculated the QDs number for the voxel shown in **Figure 3-11**(f). The AFM measured results show that this voxel has the diameter of 125 nm and 17 nm in height. So the calculated volume of this voxel is around 5.56×10^5 nm^3. And the calculated total number of QDs is around 4.97 (rounded to 5).

3.4.4 Background emission from IEWs substrate

One may notice that we did not use a blue laser to excite the polymer-QDs structures. That is because in this case, there exists a strong emission emitted from the waveguides themselves. **Figure 3-28**(a) shows the waveguide-coupled emission spectrum obtained by exciting the QDs with a blue laser. Here, we replaced the green laser with the 405 nm blue laser and we organized PL measurements by exciting directly the IEW without any QD-polymer voxels integrated with a blue laser (404 nm). The measurement process is shown in **Figure 3-28**(a). 10 waveguides with good surface qualities were chosen, and the laser was focused at the center of each waveguides along the propagation direction. And no filters were used and the reason we have mentioned

above. Finally, the fluorescence was detected at the end of corresponding waveguide towards to the spectrometer. The average spectrum is shown in **Figure 3-28**(b). Clearly, the peak at 404 nm represents the excitation laser which is also indicated with a captured CCD image shown in inset (i) of **Figure 3-28**(b), and there is another narrow peak locates at around 550 nm, which we assume that is from the emission of sliver ions introduced into IEWs during the thermal ion exchanged process. Furthermore, we also found several articles in the literature which describe similar emission from silver ions [145–147]. Besides, a broadband emission is also observed between 600 nm to 800 nm, and we attributed this to the emission of the glass material. In order to confirm this, we organized the PL measurement for pure glass substrate, the spectrum is shown in the inset (ii) of **Figure 3-28**(b). Apparently, the intensity starts decreasing from around 650 nm, which has a similar tendency with the emission of the IEWs samples.

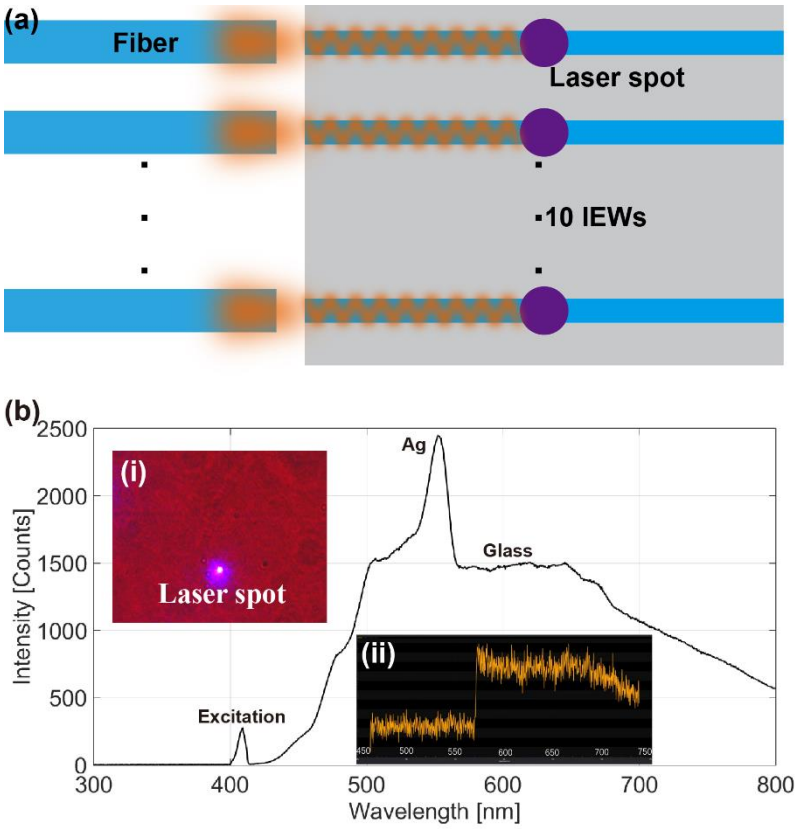

Figure 3-28 (a) Schematic of PL measurement process for pure IEWs with 404 nm excitation laser; (b) The average of 10 measured PL spectrums.

the inset (i) shows laser spot and (ii) shows the emission from a pure glass substrate with a filter was set to filter the emission below 560 nm.

The result is also confirmed by recorded fluorescence CCD images of ion-exchanged waveguides, as shown in **Figure 3-29**(a). A long-pass filter with wavelength of 530 nm was set before the camera. 5 neighboring waveguides were excited by scanning the IEWs sample, and far-field fluorescence is recorded at different time. Bright red emission can be observed when the laser hit the waveguides. While no emission was observed when laser beam excites the other positions on the sample surface. In addition, a laser-scanning measured PL image for the single IEW is shown in **Figure 3-29**(b). This significant results show evidences that the sliver ions diffused inside IEWs can emit light as long as excited with the blue laser. Therefore, it is necessary to avoid any other emission from the IEWs substrate except the QD-polymer nanocomposites for our applications.

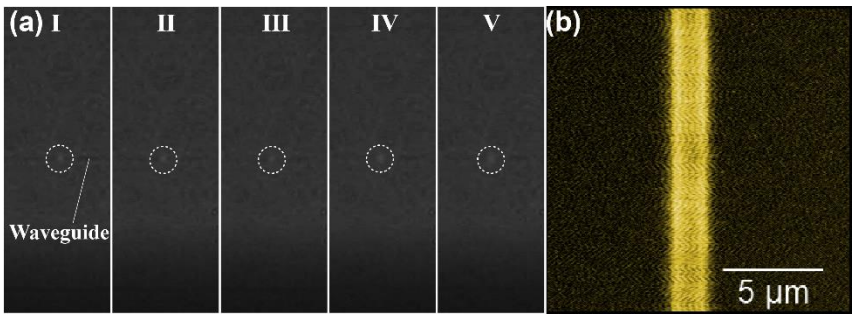

Figure 3-29 (a) PL images of 5 IEWs measured by scanning the excitation laser. The emissions are depicted with white dashed lines; (b) Laser scanning measured PL image for single IEW.

Considering our low waveguide-coupled QD emission signal, the emission from the background can easily obscure the QD emission intensity and overlaps with its wavelength. Therefore, for reducing the background emission, one practical method is to switch from the blue laser to the green laser due to the insensitivity of the silver ions

to the green laser. **Figure 3-30** shows the emission spectrum obtained by using a green laser to excite the waveguide. The narrow peak is the detected excitation green laser which is also shown in the inset. In contrast with the result in **Figure 3-28**(b), it is clear that the silver ion emission disappeared and only the part of emission from glass substrate is still present. That is the reason why a green laser was used as excitation source in the section 3.4.2.

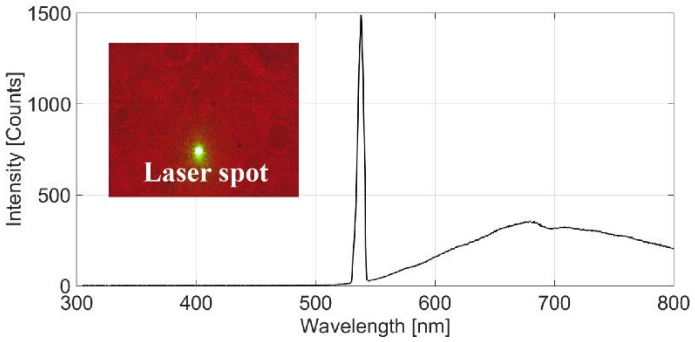

Figure 3-30 PL spectrum detected at the end of waveguide with a 532 nm laser, inset indicates the green laser spot.

3.5 Perspective and conclusion

Further investigations will be done to push the limits of the fabrication and characterization process in order to control carefully the number of quantum dots embedded in the polymeric nanostructures. For detecting the emission from less quantum dots (even single QDs) coupled to the IEW, it is possible to increase the signal by improving coupling efficiency from quantum dots to IEWs. The low coupling efficiency is mainly due to the weak electric field confinement to the interface between QDs and IEWs. One efficiency way to increase the coupling would be to add a layer of TiO_2 between the QDs and the IEW. The covered TiO_2 layer on IEWs with higher refractive index has already demonstrated the increase of light confinement to the interface in the previous work [143]. **Figure 3-31**(a-c) show the schematics of a single QD on a glass substrate, a pure IEW, and an IEW covered with a TiO_2 layer,

respectively. For the IEW covered with a TiO_2 layer, the polymer voxel size here should also be reduced for ensuring the high optical confinement between TiO_2 layer and the IEW. Corresponding simulated QD emission propagations along z-axis are shown in **Figure 3-31**(d-f). Here, we put a dipole inside a polymer semi-ellipsoid with a diameter of 50nm which is then cover by a 100 nm TiO_2 layer. The excitation light is the 590 nm mode source. An expanded power monitor is placed inside the IEW and behind the dipole source, this expanded monitor count only the light energy coupled to the fundamental modes of the IEWs, so we could calculate the ratio of the light power before and after the dipole. Here, based on our simulated results, the QD-IEW coupling efficiency is increased to 23.6% for IEW covered by TiO_2, while only 0.22% for the pure IEW. 100 times enhancement can be achieved. This is promising for improving the coupling efficiency for our future works. Moreover, reducing the fiber-waveguide coupling losses, placing QDs near the hot spot of plasmonic nanostructures and creating a reflector at another end of the waveguide can be further applied to increase the PL measurement signal [13,14,144]. Our results give a new method for integrating not only QDs, but also other quantum emitters such as single molecules or single nanodiamonds onto complex hybrid quantum devices in the future.

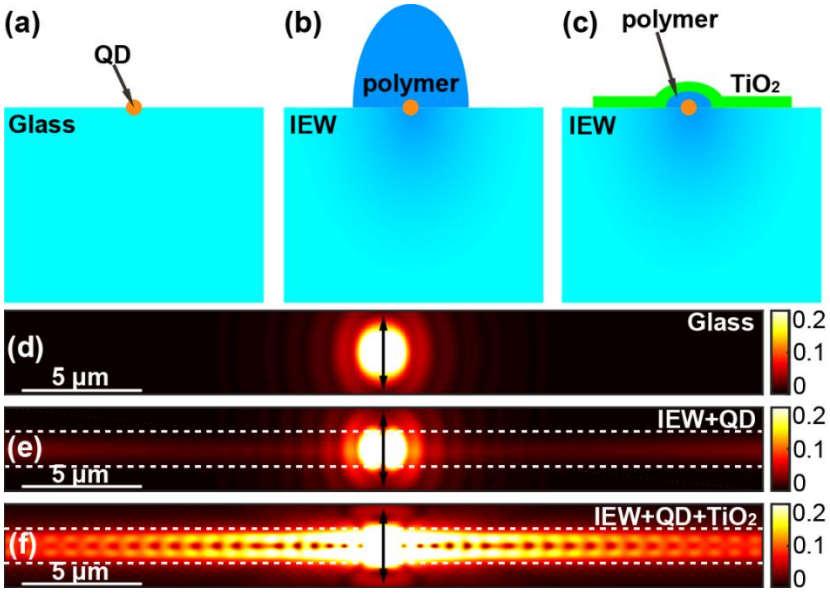

Figure 3-31 (a-c) Schematic of single QD integrated on (a) a glass substrate, (b) a pure IEW substrate and (c) IEW substrate covered by TiO_2

with thickness of 100 nm; (d-f) Visualization of simulated electric field |E| of coupled QDs emission and light (590 nm) propagation in (d) pure glass substrate, (e) a pure IEW and (f) IEW covered by TiO_2. The results were obtained 200 nm below the surface. Black solid arrays at center indicate x-orientation dipole sources with polarization along x-axis, while white dashed line represent the outlines of IEW.

To conclude, we demonstrated the capability of the DLW-TPP method for enabling the positioning of nanoemitters on a thick substrate leading to the coupling of the light to a photonic optical chip. Based on this technique, the control of three fabrication parameters, namely, the laser power, the exposure time and the focal height, provide a control of the QD-polymer voxel size, which is strongly related to the volume of the voxels, all confirmed by far field photoluminescence measurements. Single QD-polymer nanostructures have been successfully integrated at the center of an ion exchanged optical glass waveguide for the first time. The QD emission was measured from the waveguide facet by our home-build measurement setup. The extracted spectrum of our quantum dot emission showed a narrow peak at 590 nm which is in good agreement with the far field measurement result and suggests that the PL from only few QDs is efficiently coupled into the waveguide. This shows the high potential of QD-polymer nanostructures for nanosources of light positioned onto glass photonic circuits. Future work will focus on improvements of the emission efficiency from quantum dots into the waveguide to enable the efficient detection of single quantum dot emission from the waveguide facet for smaller integrated QD-polymer nanostructures. Finally, our developed DLW-TPP technique opens an exciting route for the top-down deterministic integration of quantum dot or other quantum emitters such as colored centers in nanodiamonds within future complex quantum photonic circuits.

Chapter 4 Additional experiments towards future works

This chapter presents additional experiments for further developments in the future regarding the integration of nanoemitters on more elaborated IEW-based hybrid structures. As we already mentioned, our final goal is to realize the integration of nanoemitters near plasmonic structures based on glass IEWs. Although we have demonstrated the possibility and feasibility by directly creating QD-polymer nanocomposites directly on IEWs in Chapter 3, there still exist some challenges that need to be resolved including:

i- the reduction of noise fluorescence from the IEWs (4.1);

ii- how to optimize the coupling efficiency from QDs to waveguides using SiC layer (4.2);

iii- how to position nanoemitters near the 'hotspots' of plasmonic structures by surface functionalisation (4.3) and the DLW-TPP technique (4.4).

These issues greatly influence the possibility of DLW-TPP technique for our future works and some partial solutions have been implemented as can be seen in the following paragraphs.

4.1 Reducing the silver ion emission from the waveguides

As already mentioned in Chapter 3, the silver ions diffused inside glass-based ion-exchanged waveguides (IEWs) can emit light when using a blue excitation laser. Although we can replace the blue laser with a green laser which can reduce the silver ion emission significantly, a blue laser is still more suitable for exciting the QDs

efficiently and benefit from their excellent emission properties. Thus, it is necessary to reduce the light emission from silver ions under the illumination of a blue laser.

During the process of measuring the far-field emission of IEWs themselves, we found that the emission disappeared when the waveguide surface is under the illumination of the blue laser for long time, which is similar to the phenomenon of quenching. Quenching refers to any process which decreases the fluorescence intensity of a given substance, and quenching can occur through various mechanisms [148]. Metal ions (including silver ions) have been shown to act as a quencher [149–151]. That gives us the possibility of reducing this fluorescence 'noise' from the IEWs.

In order to do that, we intended to compare the spectra by exciting a fixed position at the center and onto the waveguide surface before and after a long-time exposure laser irradiation. However, the position of the laser spot tends to drift slowly during the process due to the mechanical drift of our piezo-stage. This makes the excitation laser spot deviate from the waveguide surface and move to the glass surface where has no waveguides. It is thus not possible to do the measurements for the specific positions. Another solution is to scan a micro-scale area of the waveguide surface. In this case, the area is illuminated evenly, so even though the position shifting happens, we can still measure the emission at different positions and calculate the average PL spectrum within the area. We can then compare with the spectrum before the laser illumination.

There is however one obstacle which comes from the fiber-edge coupling. The sample and the fiber are both fixed on piezo scanning stages separately and long-time scanning movements will cause relative position shifting between the fiber and the waveguide. In order to stabilize the fiber-edge coupling condition, we pigtailed our IEWs with polarization maintaining (PM-panda, SM-630) fibers. **Figure 4-1**(a) shows the pigtailed IEW sample which was done at Teem Photonics by Muhammad Ahmed. This pigtailing avoids position shifting during the measurements, decreases light scattering at the waveguide edges and also increases the light coupling between the waveguide and the fiber, which is very similar to the function of the polymer drop

between the fiber and the waveguide as illustrated in **Fig 2-7**, section 2.2.1). Next, a blue laser (404 nm) was used as the excitation beam and focused on the waveguide surface. The pigtailed fiber was connected directly to our cooled grating spectrometer (PI Acton SP2300), as shown in **Figure 4-1**(b). The IEW sample was moved along the x- and y- directions (20 × 20 μm^2, 5 min per scanning) by the piezo stages underneath.

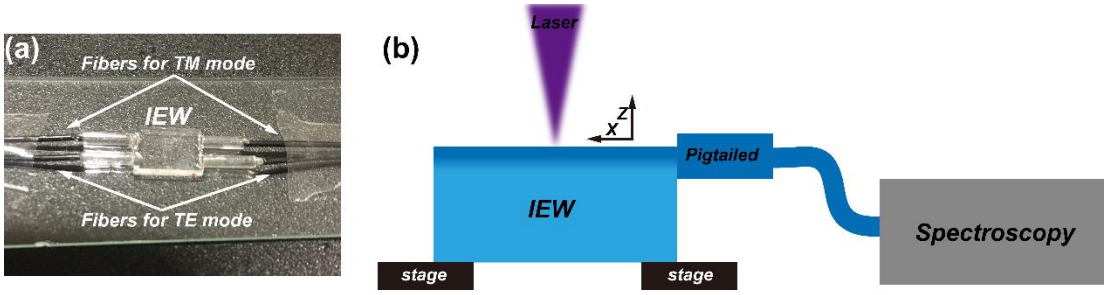

Figure 4-1 (a) Pigtailed IEW with PM fibers; (b) Schematic of measurement setup.

Figure 4-2 shows the measured PL spectrums from the positions within the scanning area before and after laser illumination. The PL intensity drops by half after scanning 1 time (about 5 min). For longer scanning times the PL intensity decreases slowly. That might be due to the fact that the excitation laser power was not strong enough (maximum laser power was about 5 *mW*, measured before the objective lens), a lower PL intensity could be obtained after the sample was scanned for longer time (10 min and 15 min which were also plot with red and green in **Figure 4-2**). One can notice In **Figure 4-2**, some standing waves can be found and that might be due to the second pigtailed fiber on the other side of the IEW. In this situation, the silver ion emission propagates along two opposite directions and then are reflected by both IEW sides, which results in the light interferences within the waveguide.

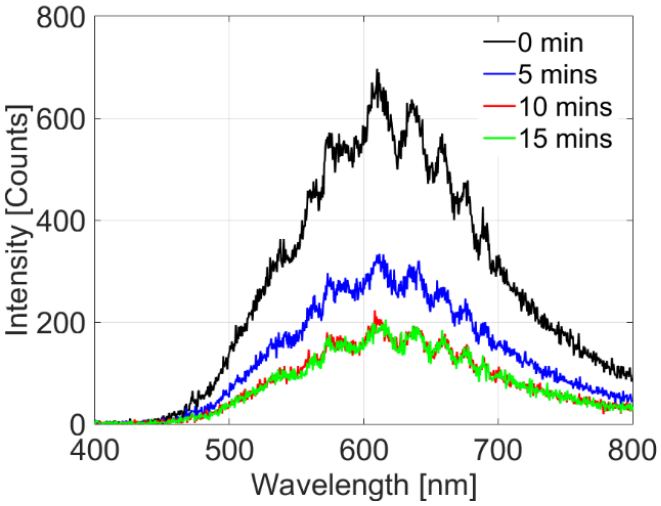

Figure 4-2 Measured spectrums before and after the laser scanning.

There is a difference between the PL spectra shown in **Figure 4-2** and the ones shown in **Figure 3-29** is the fact that no excitation laser signal (located at around 405 nm) can be observed in **Figure 4-2**. When the blue excitation laser is focused on the sample surface, part of the light can be coupled into the glass material or scattered at the surface. In the case of Chapter 3, the fiber was not pigtailed to the waveguides edges. As such, the excitation light scattered at the sample surface could be directly coupled into the waveguides. While in **Figure 4-2**, due to the nice quality of the pigtail of the fiber to the IEW sample. the pigtailed fiber only allows the light coming from the waveguide propagation modes to couple into. As the IEWs are designed and fabricated for the visible and near-IR ranges (500 - 780 nm), the blue laser (405 nm) was filtered out by the IEWs and no excitation was found in the spectra in **Figure 4-2**.

4.2 SiC layer deposition on IEW as an alternative to TiO_2

As shown in Chapter 3, adding a layer of TiO_2 increases the light coupling between IEWs and the QDs in an efficient way. Silicon carbide (SiC) is another material with a high refractive index and could be another good candidate for obtaining a higher coupling efficiency [152]. In this section, we introduce the first results about the PL measurements for the QDs emission from the IEWs covered by the SiC layer.

4.2.1 Confocal laser scanning microscopy (CLSM) for PL measurements

Here, we developed our fiber-chip coupled PL measurement setup in order to detect, measure and extract the light signals only from the QDs emission. The configuration of the microscope has two detection channels with filters allowing the detection of the fluorescence wavelength longer than 510 nm. The sample was mounted on a piezo stage and the excitation laser was temporally modulated by an acousto-optic modulator (IntraAction Corp. AOM-80) to produce the RF signals. The excitation laser was then collimated and expanded by several mirrors and lenses, finally was focused on the sample surface by a 50× Objective lens (Olympus LMPLFLN). The sample and the butt-coupled fiber were both fixed on a x-y piezo stage, which enable to realize scanning the sample and obtain the PL images. As long the sample was excited by the laser, one part of the QDs emission came back to the objective lens and then reflected by a beam splitter, finally was transferred into a photodetector, this detected signal is called “far-field” QDs emission. While another part of the QDs emission could be coupled into the underneath IEW, and then detected by another photodetector, we call this detected signal “waveguide-coupled QDs emission”. Here, two avalanche photodiodes (APDs) were set to record the emission which were measured from the top (far-field) and from the side of the IEW independently to convert the light signals to AC signals. Considering the emission wavelength of our QDs is in the visible range, our so-called APD2 (Hamamatsu Photonics C5460, designed for near-IR range) was less sensitive than our so-called APD1 (Hamamatsu Photonics, C12703-01, 400-1000 nm). Based on our experience, the emission signal detected at the IEW edge is much weaker than that from the top, so we measured the signal from the top using the APD2 and the waveguide-coupled signal using APD1. After the signals were processed and extracted using a lock-in amplifier, the signals only from the detected QDs emissions were subsequently sent to the computer system and converted to the PL images. The schematic of the measurement setup is shown in **Figure 4-3**.

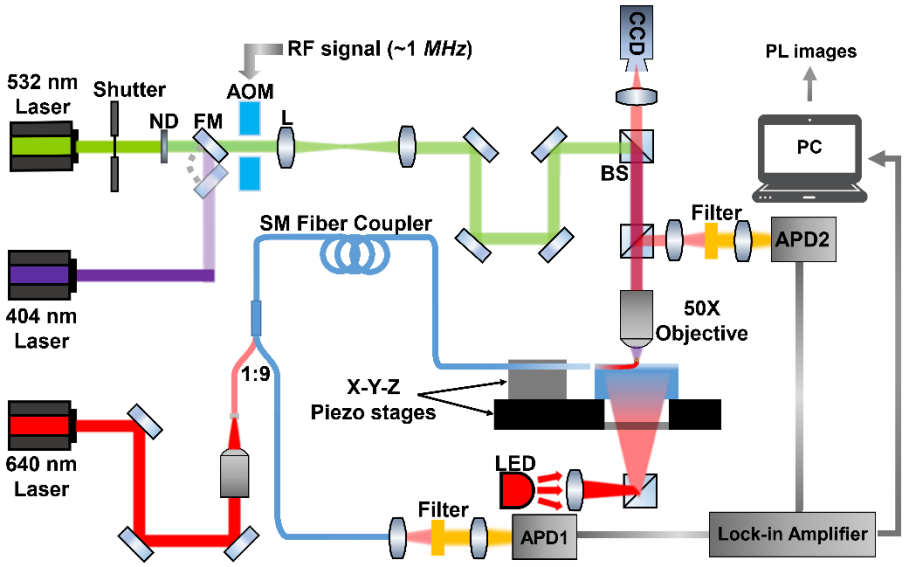

Figure 4-3 laser-scanned PL images measurement setup with a modulated excitation laser.

4.2.2 Detection of the QDs emission from the SiC layer covered IEWs

In order to show that the deposition of a SiC layer can also be used for optimizing the light coupling from the QD-polymer to the IEWs, we fabricated QD-polymer lines near the edge of the SiC layer and across the IEWs. **Figure 4-4**(a) shows the deposited layer of 50 nm SiC on an IEW sample (This sample was fabricated by PhD student Muhammad Ahmed). A maximum coupling efficiency about 5% (the light from a dipole to the IEW) could be obtained with the 50 nm-thickness SiC layer. A 640 nm CW laser was coupled into the IEW in order to see the difference in light scattering from the areas without and with the SiC layer. It is apparent that there is more light scattered from the right part covered on with SiC than the left-hand side without a layer of SiC. This means that the more IEW propagating light was converted into the SiC layer, as shown in **Figure 4-4**(b).

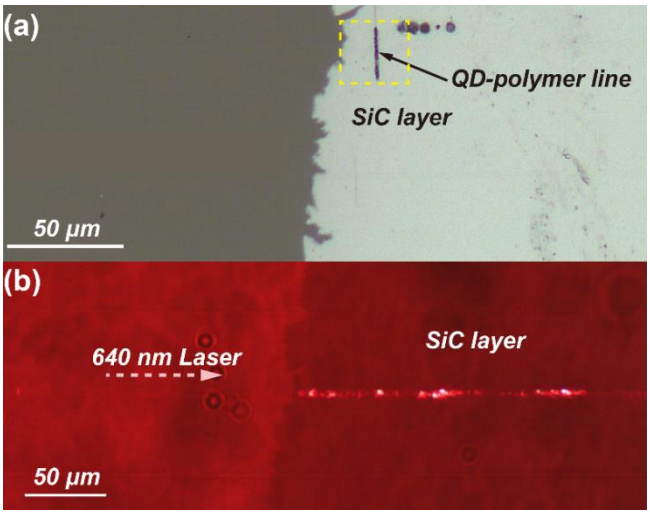

Figure 4-4 (a) Deposited SiC layer on top of IEW surface; (b) Comparison of light scattered from IEW surface and SiC layer.

By scanning the sample in the x-y plane with the piezo stages, we conducted the PL measurement for the QD-polymer line, shown in **Figure 4-5**(a). The white dashed lines represent the outlines of the crossed IEWs. Low excitation power here was used in order to avoid damaging the physical property of our quantum dots during the scanning (usually 5 min per image). **Figure 4-5**(b) show the corresponding recorded images of the laser reflection measured by APD2. As one can see, the reflected signal measured with APD2 is strong enough for observing the QD-polymer line. The refractive index of SiC layer is much higher than the polymer and glass material, so the laser reflection from the SiC layer is also higher, resulting the much bright area. This result show the setup enable to obtain a stable laser scanned image. The most important result is the signal of the waveguide-coupled QDs emission recorded using APD1, shown in **Figure 4-5**(c). Although the detected signal is weak, which is might due to light propagation losses in the IEWs and the low light coupling efficiency from the QDs to the IEWs, we are still able to obtain the PL image which show the signal from the IEW position is much higher than that from the area outside the IEW. This is the proof of the QDs emission was coupled into the underneath IEW and propagates along the IEW, and then was detected by the butt coupled fiber. The distorted shapes of the QD-polymer lines in **Figure 4-5**(b) and (c) are due to the effect of the mechanical drift. In

fact, during our measurement process, the signals measured with APD1 were usually also affected by the environment noise due to the excitation laser and the signal lights of the experimental equipment. This has never been realized for the fabricated QD-polymer nanocomposites directly on the IEWs surface (without SiC layer) with the same measurement setup. We mention that this is the preliminary measurement result, there is still a long work to do to optimize the coupling conditions and improving the detections.

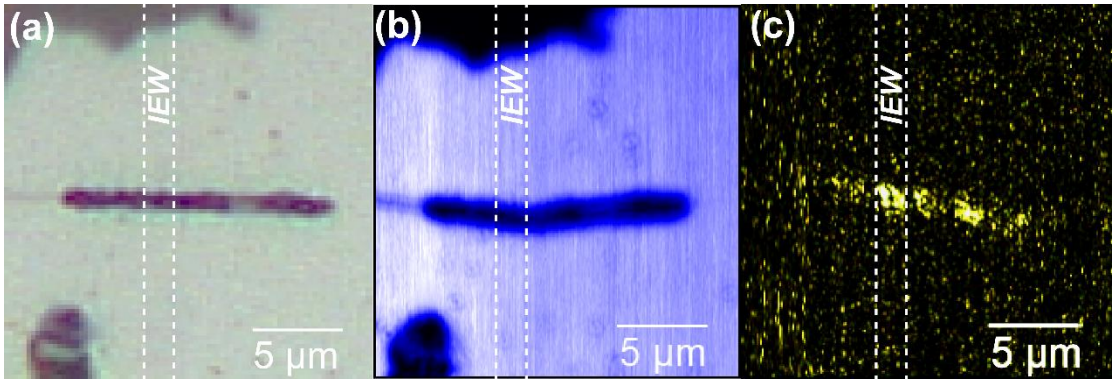

Figure 4-5 (a) Microscopy image of a QD-polymer line across a waveguide; (b) Reflected excitation laser detected with APD2; (c) Waveguide-coupled emission detected with APD1.

4.3 Photopolymerized structures attached with functionalized QDs

As seen in previous sections, we can mix quantum dots into a polymer matrix in order to obtain a controlled emission from micro/nano structures. Within our another project, we are currently working on another way of combining the quantum dots with the polymer and that is by functionalizing and changing the surface chemistry properties of the quantum dots in order to get attached to the polymer rather than being inside it. By this mean, quantum dots can be attached at the surface of pre-fabricated polymeric structures. The details on how to functionalize the QDs are not described as this process is currently undergoing a publication for a patent. This work and preparation was done by Dr Ali ISSA who is currently a post-doc at the L2n. **Figure**

4-6 shows the basic process of attaching the functionalized quantum dots onto the surface of prefabricated polymeric structures. After the fabrication of polymeric structures, a droplet of functionalized QDs liquid was put on the sample surface, then the connection between QDs and the polymeric structures surface occurred after a while. The surface-attached QDs can be obtained after developing the process.

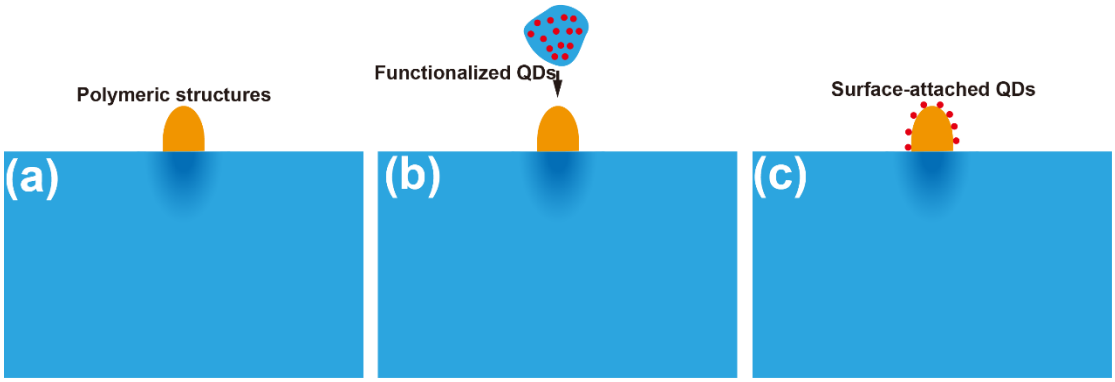

Figure 4-6 Basic process of grafting quantum dots on the surface of polymerized structures. (a) Printed polymeric structures; (b) Doping functionalized QDs liquid on the sample surface; (c) Attached QDs after removing the remains.

For our specific need, we fabricated various polymeric structures such as squares, lines and dots that were then grafted with functionalized QDs on top of our IEWs, as shown in **Figure 4-7**(a-c). Under the illumination of a blue LED (450 nm), significant QD emission from these structures could be observed. Predictably, the IEWs were also excited by the LED simultaneously and the emissions can be also seen clearly, as shown by the green lines (see previous sections). In terms of brightness, the squares are brighter than the IEW luminescence, while the emission brightness from the lines and the dots are comparable to the one from the IEWs. This is yet another evidence that both the emission of the IEWs and QD-polymer structures can be excited by blue light. The large area of the polymer square and the large quantity of QDs in the square enable us to measure the average PL spectrum as shown in **Figure 4-7**(d). The peaks at around 450 nm and 590 nm represent the excitation blue LED and the QDs emission, respectively. Next, we carried the PL measurement (the measurement setup has been

described in Chapter 3) for the waveguide-coupled QDs emission. As shown in **Figure 4-7**(e) for a QD-polymer line, a weak peak appeared at 590 nm which show the evidence of the detected waveguide-coupled QDs emission.

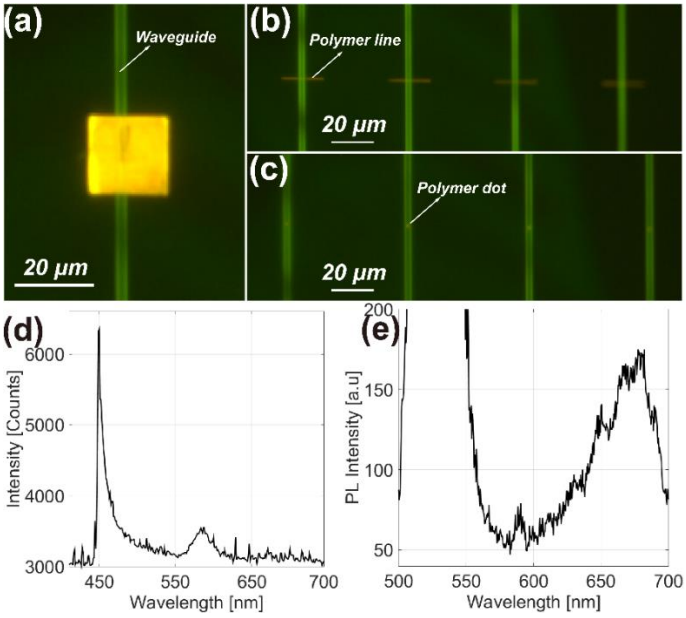

Figure 4-7 Polymerized structures attached with functionalized quantum dots. (a) Squares. (b) Lines. (c) Dots; (d) Measured far-field PL spectrum for the square; (e) Measured waveguide-coupled PL spectrum for a typical polymer line.

PL images have also been obtained by scanning the sample with the setup in **Figure 4-3**. Here, for this sample, we firstly measured the reflected laser signal and extracted the images for the QD-polymer square, line and dot as shown in **Figure 4-8**(a-c). The reflection from them are quite significant. Next, we measured the far-field PL images for the emission of these structures from the top with a 510 nm filter in order to obtain the QD emission exclusively. The QDs inside the QD-polymer square and line give much higher intensities than that of the dot. These results indicate the excellent photoluminescence performance of the QD-grafted polymeric structures. This also shows that our developed PL measurement setup is capable of detecting the QD-polymer structures with dimensions down to micro-scale.

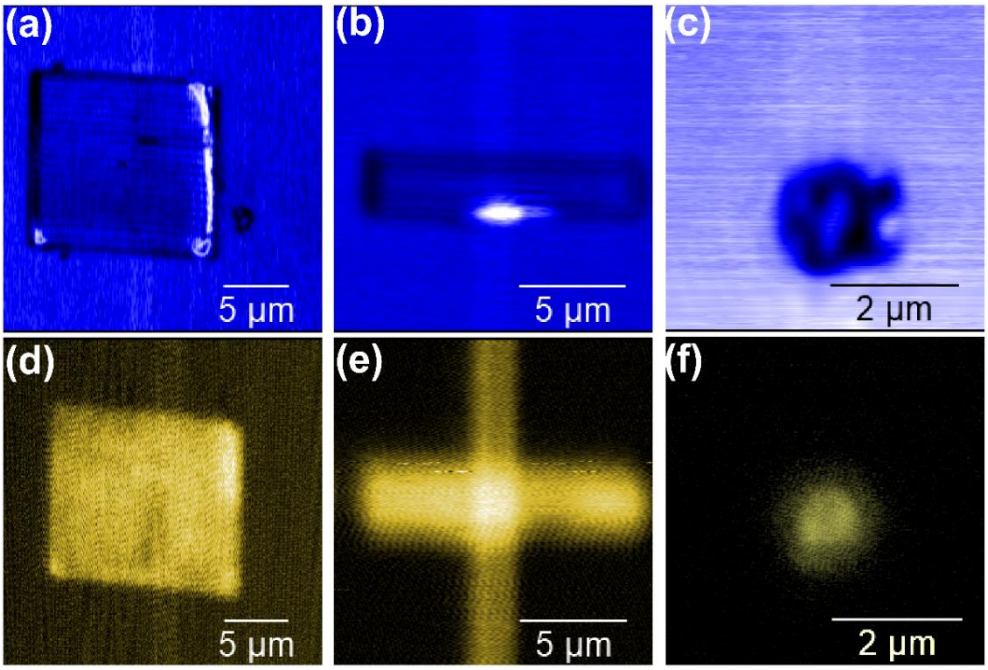

Figure 4-8 (a-c) Laser reflected signal from the QD-polymer square, lines and dot; (d-f) Measured far-field PL images by APD2 for the corresponding QD-polymer square, lines and dot, and all the emissions were filtered with a 510 nm high-pass filter.

4.4 Photopolymerization induced by plasmonic antennas

As already discussed, photopolymerization induced by plasmonic structures can be used for the controlled positioning of nanoemitters at the 'hotspots' of plasmonic structures and placed on top of photonic channels. This is of prime importance in order to maximise the interaction between a nanoemitter and a plasmonic antenna for the future observation of Purcell effect and strong coupling. Although we've already achieved the plasmon-based two photon polymerization with nanoparticles on ITO substrates, as described in section 1.3.2 in Chapter 1, in this section, we describe how we attempted to create QD-polymer structures near the pre-fabricated plasmonic Au bow-tie antennas on a planar glass substrate using the DLW-TPP platform/method. We analysed and discussed the potential solutions for optimizing the QD distribution during

all the fabricating process and hope to provide some preliminary experimental results for future works.

4.4.1 QD-polymer composites between bow-tie antennas

Figure 4-9 shows the fabrication process of plasmonic Au bow-tie antennas using electron-beam lithography. This process is divided into 7 steps:

1. **Substrate cleaning.** The glass substrate (22 × 22mm) is cleaned with an ultrasonic bath of acetone for 10 min. After that, the sample is immersed in an ethanol and isopropanol bath for 1 min, respectively. Finally, the sample is dried on a hotplate apparatus for 1 min at 90°C.
2. **PMMA deposition.** Poly(methy1 methacrylate) or PMMA is an electron sensitive resist commonly used in electron beam lithography process. Positive PMMA with concentration of 30 g/L is spin-coated on top of the substrate with a duration of 30 s and at a speed of 4000 rpm. The deposited PMMA layer has a thickness around 160 nm. After deposition, the substrates were heated up during 3 hours to 170°C in an oven.
3. **Conductive layer deposition.** In order to avoid the diffusion of charge accumulation at the surface of the PMMA. The ESPACER (a commercially conductive polymer which can be simply applied by spin coating, and simply removed by rinsing with water) was spin-coated on top of PMMA for 30 s with a speed of 3000 rpm.
4. **Electron-beam lithography.** A mask is designed in order to excite only a desired zone. After the electron beam exposure, the large molecules of PMMA are broken down to small molecules, which are more soluble than large molecules. It is thus easier to wash away by development process.
5. **PMMA development.** The ESPACER was removed by immersing the sample in a water bath for 2 min. Then, the sample was moved in MIBK:IPA bath for 1 min to remove the exposed PMMA. After that, the isopropanol was used to rinsing

residues of exposed PMMA on the sample surface. The result is a hole localized in the exposed zone by the electron beam.

6. **Au deposition.** A gold layer with a thickness around 50 nm is deposited by thermal deposition.
7. **Lift-off**. The last step of the fabrication process is to immerse the sample in an acetone bath for 2 days to remove the residues of PMMA.

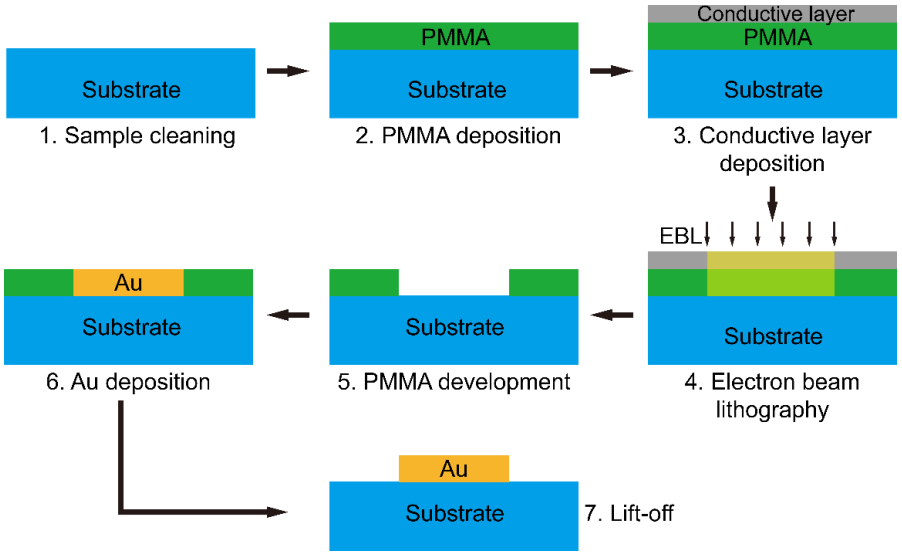

Figure 4-9 Fabrication of Au antennas on glass substrates. 1- substrate cleaning. 2- PMMA deposition. 3- Conductive layer deposition on PMMA layer. 4- Electron beam lithography. 5- PMMA development. 6- Au deposition and 7- The lift-off process.

4.4.2 Photopolymerization induced by plasmonic antennas

As shown in **Figure 4-10**, we obtained the QD-polymer composites only at the gap area of the boew-tie. Here, we used the point printing mode of the DLW-TPP system. The laser power was around 10 *mW* and the exposure time was 5 *ms* which makes the laser energy below the threshold of photopolymerization. As shown in the inset of **Figure 4-10**, although due to the observation limit of the 780 nm gaussian beam which makes difficult to see the clear outlines of our targets (bow-ties), we still got the result in which the quantum dots covered with a layer of polymer were gathered together and

confined only in the gap of the bow-ties. And no remained QD-polymer composites were found at other positions on the background.

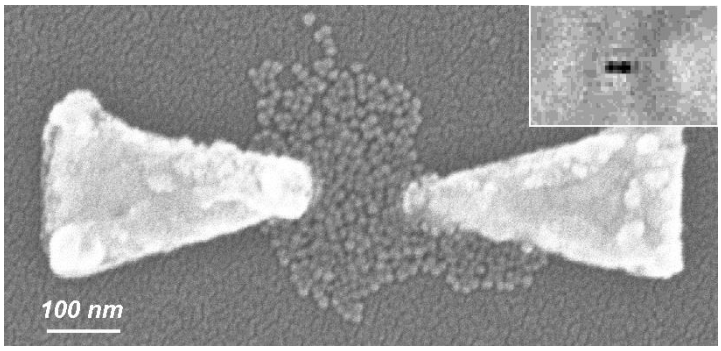

Figure 4-10 SEM image of the bow-tie antenna after photopolymerization.

Besides, during this photopolymerization process, bow-ties can also be damaged. As shown in **Figure 4-11**(a-d), some bow-ties seem to be 'melted' and their triangle-shapes were completely deformed. We postulated that the high laser energy was damaging the bow-ties during the printing process. In order to prove that, we repeated the printing for four bow-ties with different printing laser power (10-16 *mW*, steps of 2 *mW*), but with the same exposure time of 10 *ms*. With the increase of the laser printing power, the 'deformations' become more obvious. Clearly this deformation has quite an influence on the distributions of QDs which could be seen everywhere on the surface. This could be solved by using lower printing power and short exposure time as much as possible. Here, the possibility of hydrochloric acid should be ruled out. As mentioned in Chapter 3, an HCl solution was used to help removing the unexposed polymer liquid. However, due to the short bath time (5 min) and the low *pH* value ($pH \approx 3$), it has almost no damage to the bow-ties, proved by the bow-tie in **Figure 4-10**.

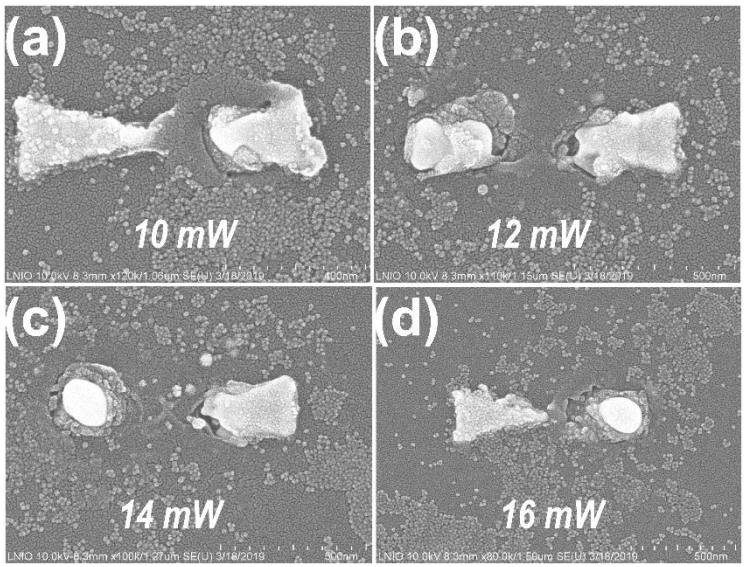

Figure 4-11 (a-d) Deformed bow-ties with different laser printing power.

4.5 Conclusion

In this Chapter, using a blue laser, we proposed to reduce the PL from the IEWs which was proven to be feasible experimentally. We also demonstrated that adding a layer of SiC on top of the IEWs can help increasing the coupling efficiency from the QDs to the IEWs. We also presented some first tries on printing QD-polymer composites around bow-tie structures and analysed the problems such as QD distributions and deformations of bow-tie structures. These results indicate that it is possible to realize a high efficiency coupling of nanoemitters on glass-based circuits using the DLW technique based on two photon polymerization. These experiments can provide valuable experience for further optimizing the structure configuration and experimental procedures in future works.

General conclusion

The integration method based on photopolymerization provides a simple way for creating nanoemitters onto photonic substrates with the positions highly controlled. The photopolymerized nanoemitters can be integrated onto the prefabricated/preselected photonic chip and function as the non-classical light sources to quantum devices, and it is expected to be applied to more commercial photonic devices.

We first reviewed the main integration method for crating nanoemitters on different photonic devices. However, the complicated and time-consuming manufacturing process of these methods limits their applications. The concept of the nanoemitters based on QDs-contained polymeric nanostructures is proposed, which is created by the photopolymerization reaction. Two examples (were carried out simultaneously with my PhD work) of plasmon-based polymerized nanoemitters coupled with silver nanowires and gold nanocubes, respectively, show the feasibility of this method for being applied to the hybrid plasmonic nanosystems. While in this PhD work, we showed the advantages of the optical glass ion-exchanged waveguides (IEWs) and present the target of this thesis is to realize the integrated nanoemitters onto the glass IEWs-based optical substrates by photopolymerization process.

We next conducted the photopolymerization induced by a IEW-coupled green laser. We analysed the problem of unstable output laser power from the IEWs and found the length of overhead fiber tip, fiber types and light propagating of IEWs are the three main parameters can affect the stability of the experimental platform. The instability of output power has been reduced by 15 times after the optimization of the experiment setup. Polymer ridges with and without quantum dots were fabricated and characterized, the results show the ability of controlling their dimensions by adjusting the excitation laser power and exposure time. A TiO_2 layer was deposited on top of IEWs surface to

obtain the QD-polymer ridges chain, which is caused by the beating behaviour of the propagating modes of IEW and TiO2 layer.

In order to fabricate the QD-polymer nanocomposites on IEWs substrate, we developed the TPP-based direct laser writing platform with a 'sandwich' configuration. By optimizing the cleaning process after the photopolymerization. the quantity of quantum dots remaining outside of the QD-polymer voxels decreases 43%. We demonstrated that by adjusting the printing laser power and exposure time, the volume of the printed QD-polymer voxels can be controlled down to nanoscale, resulting in the difference in quantities of the QDs inside these voxels, which are verified by the PL measurement results. In addition, by adjusting the printing laser focal height, the typical size of the voxel could be scale down to 17 nm in height and 125 nm in diameter, which probably contains only 4-5 QDs based on our calculation and the fabricated single layer of QDs.

Most importantly, we succeeded in fabricating a single QD-polymer voxel directly on a IEW by the developed DLW-TPP platform. A significant far-field emission could be observed and the PL spectrum show the evidence of the emission comes from the QDs inside the voxel. Moreover, we demonstrated the IEW-coupled QDs emission by detecting at the end of waveguide coupled with a fiber in spite of the weak detection signal. The discrepancy of the PL spectrum between far-filed and IEW-coupled was explained by the dissimilarities in the PL measurement conditions, which was proofed by our simulated results.

Additional experiments were conducted for further developments in the future regarding the integration of namoemitters on IEW-based structures. By illuminating the IEWs with longer time, we are able to decrease the emission form the IEWs themselves, which helps identifying the QDs emission for smaller QD-polymer nanocomposites. We also demonstrated depositing a SiC layer on IEWs surface can help the light coupling between IEWs and QD-polymer nanocomposites by the laser scanned PL images. We demonstrated the light-emitting properties including far-field and IEW-

coupled emission for the polymeric nanostructures with attached QDs. At last, we also conducted the first integration of QD-polymer composites near the plasmonic bow-tie structures by the DLW-TPP platform.

There is still a long work to do to succeed in our final goal which is the realization of the integrated nanoemitters onto a complex IEW-based photonic structures. Many issues such as coupling efficiency between QDs and IEWs, laser printing process and PL controlling need to be explored. The results shown in this work actually provide primary experimental experience for our future work, and also feeds a strong reference for other research in the fields of guided optics, photopolymerization reactions, 3D laser printing techniques and photoluminescence measurements.

Chapter 5 Résumé en français

Les nano-émetteurs et les nanosources de lumière sont des éléments cruciaux pour de nombreux dispositifs photoniques destinés à être utilisés dans l'imagerie biologique, les lasers optiques, les capteurs et les technologies quantiques [1-4]. Les concentrateurs de lumière hybride photonique-plasmonique proposés par notre groupe ont déjà démontré l'efficacité des structures permettant de produire une amélioration du champ électromagnétique à l'échelle nanométrique, qui convient parfaitement aux nanoémetteurs intégrés et à l'obtention d'un système à effet purcellulaire [78]. Par la suite, des configurations de structures similaires basées sur des guides d'ondes d'échange d'ions ont également été proposées comme plateforme photonique pour l'intégration de sources de photons uniques. Dans ce type de structures, la possibilité de couplage de la lumière entre les nano-émetteurs et les structures photoniques a été démontrée comme étant faisable en utilisant des méthodes de simulation.

Pour la réalisation pratique de ces dispositifs photoniques évolutifs, l'une des exigences clés est la capacité d'intégrer des nanoémetteurs sur des emplacements de puces optiques spécifiques. De nombreuses approches ont été explorées, notamment la lithographie par faisceau d'électrons (EBL) [8,9], le piégeage optique [10,11] et les méthodes de transfert par microscopie à force atomique (AFM) [12,13]. Cependant, ces méthodes présentent certaines limites telles que des opérations compliquées, des coûts de fabrication élevés et de multiples étapes de fabrication. En optique quantique, l'émission d'un seul photon se fait principalement dans l'espace libre, ce qui limite leurs applications sur la plupart des puces photoniques préexistantes. Jusqu'à présent, moins d'efforts ont été consacrés à la création de nano-émetteurs sur des puces de verre avec des méthodes d'intégration efficaces.

La photopolymérisation contrôlée dans l'espace représente un outil intéressant pour le micro et le nanomodelage des structures polymères [14]. L'écriture laser directe (DLW) basée sur la polymérisation à deux photons (TPP) a été utilisée pour produire des structures polymères tridimensionnelles (3D) arbitraires à l'échelle micro et même nanométrique de manière rapide et simple avec une grande précision de positionnement et d'écriture laser [15]. Les points quantiques semi-conducteurs colloïdaux luminescents (QD) se sont déjà révélés être des nano-émetteurs à l'état solide prometteurs dans les domaines de la nanophotonique et de l'optique quantique [5-7]. Récemment, l'intégration de points quantiques semi-conducteurs dans une matrice hôte photopolymère a été exploitée pour produire des composites QD-polymère par photopolymérisation, qui associe la propriété d'émission de lumière active des QDs aux possibilités technologiques de la matrice polymère [26-29]. Cependant, l'intégration de ces nanocomposites QD-polymère sur les guides d'ondes préexistants ou présélectionnés reste un défi.

Cette thèse vise à explorer la faisabilité de l'intégration de nanoémetteurs basés sur des nanocomposites de QD-polymère sur les guides d'ondes optiques à base de verre. L'objectif final du projet est de réaliser des nanoémetteurs intégrés sur des guides d'ondes plasmoniques-photoniques hybrides. Mon travail de doctorat est principalement axé sur l'exploration préliminaire, notamment la construction du dispositif expérimental, l'optimisation du processus de polymérisation, la caractérisation des nano-émetteurs polymérisés et l'analyse du couplage des QDs-guides d'ondes. L'objectif final de ce projet est d'intégrer des nanoémetteurs sur des puces de verre en utilisant la technique de l'échange d'ions. À long terme, nous voulons réaliser une communication par bus de lumière optique entre différents émetteurs dans le domaine visible.

5.1 Concepts préliminaires

Ce chapitre passe en revue les principales méthodes existantes d'intégration des nano-émetteurs sur/dans les dispositifs photoniques. Nous proposons une méthode d'intégration chimique basée sur la photopolymérisation et en présentons les concepts de base. En mélangeant des nanocristaux colloïdaux semi-conducteurs luminescents avec des solutions photopolymères, les nanocristaux peuvent être intégrés dans des structures polymères à l'échelle micro/nanométrique pendant le processus de photopolymérisation.

5.1.1 État des lieux et défis

Des méthodes de fabrication fiables nécessitent le dépôt contrôlé de nanoparticules/nanoémetteurs sur des substrats photoniques arbitraires avec une grande précision. Depuis une dizaine d'années, de nombreuses approches ont été explorées, notamment la lithographie par faisceau d'électrons [1-3], le piège à force optique [4-7], les forces capillaires interfaciales [8-11], la croissance épitaxiale [12-16] et les techniques de "pick-and-place" [17,18]. Nous passons maintenant rapidement en revue ces différentes méthodes.

Lithographie à faisceau d'électrons:

La méthode la plus populaire utilisée dans ce contexte est la lithographie par faisceau d'électrons (EBL) qui utilise un faisceau d'électrons focalisé à haute énergie, pour générer un contraste sur la photoréserve, formant ainsi des motifs aussi petits que plusieurs dizaines de nanomètres. Pour la plupart des structures photoniques, des procédés EBL supplémentaires doivent être réalisés afin de placer les nanocristaux aux positions souhaitées, ce qui augmente la complexité opérationnelle de la méthode.

Croissance épitaxiale:

La croissance épitaxiale pour la préparation de points quantiques a été démontrée lorsque des matériaux dont le réseau est apparié ou non peuvent être utilisés pour la fabrication des QDs [15]. Combiné à la lithographie par faisceau d'électrons et à la spectroscopie de luminescence, on peut créer de manière déterministe des dispositifs photoniques quantiques intégrés hybrides contenant des points quantiques individuels

présélectionnés. Toutefois, le processus de fabrication compliqué reste un problème important en termes d'intégration. En outre, un point quantique unique intégré dans un circuit doit encore être présélectionné, ce qui limite l'application pour de nombreux types de dispositifs photoniques quantiques.

Pince optique:

La **Figure 5-1**(a) montre un exemple dans lequel deux fibres optiques sont utilisées pour piéger et faire tourner une cellule musculaire humaine. Cette technique est appelée "pincette" à double fibre [27]. Combinées à des structures plasmoniques (telles que des antennes et des cavités plasmoniques à l'échelle nanométrique), les forces optiques de proximité provenant de plasmons de surface localisés peuvent être utilisées pour attirer et manipuler les nanoparticules vers les points chauds avec une puissance inférieure à celle utilisée pour le piégeage optique en espace libre. Comme le montre l'exemple de la **Figure 5-1**(b).

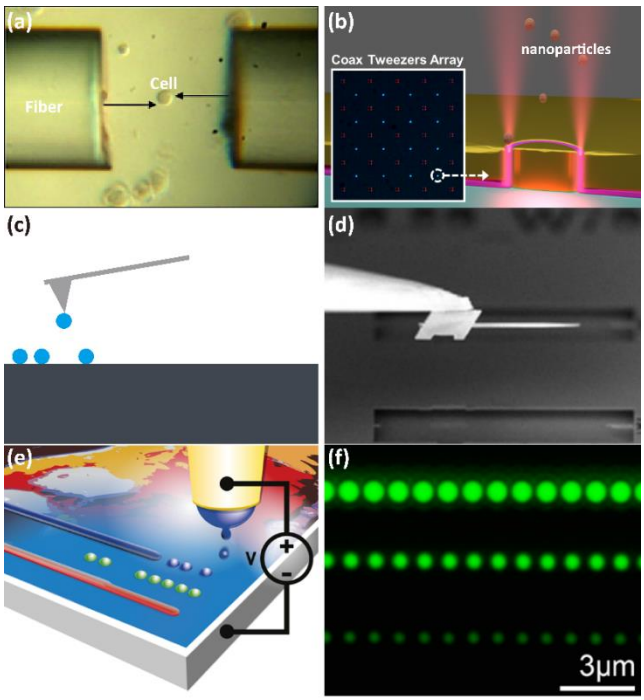

Figure 5-1 (a) Cellule musculaire humaine capturée par deux fibres optiques; (b) Piégeage optique de nanoparticules avec des nano-ouvertures résonantes de 10 nm d'intervalle; (c) Schéma du pick-and-place des nanoparticules; (d) Structure conique fabriquée et piquée contenant des points quantiques d'InAs; (e) Schéma du dispositif d'impression EHD; (f)

Micrographies par fluorescence de points imprimés. (Image tirée de [15,18,27,32])

La technique du "pick-and-place:

La **Figure 5-1**(c) présente une esquisse de la procédure de base de "pick and place". En principe, il est possible de l'étendre aux nanocristaux car elle ne repose que sur l'adhésion de surface. Kim et al. ont intégré un émetteur quantique unique sur une puce photonique en silicium en prélevant une structure conique contenant des points quantiques sur un guide d'onde en Si, comme le montre la **Figure 5-1**(d) [18]. Bien que cette méthode puisse être appliquée pour prélever et placer des particules arbitraires avec une précision à l'échelle nanométrique, contrairement au processus de prélèvement, la pose n'est pas toujours réussie, ce qui limite ses applications sur des surfaces complexes aux arêtes vives [30].

Electrohydrodynamic (EHD) printing:

Récemment, une approche similaire d'impression haute résolution basée sur une solution, appelée impression électrohydrodynamique (EHD) ou NanoDrip, a été développée [31,32]. La **Figure 5-1**(e) montre le schéma d'une configuration EHD. En contrôlant les paramètres d'impression tels que la tension de polarisation, la vitesse de balayage de la buse, le volume et l'intensité de la fluorescence peuvent être manipulés [32]. Les images de fluorescence des spots imprimés ont confirmé une résolution sub-micro, allant de 200 à 100 nm, comme le montre la **Figure 5-2**(f).

5.1.2 Concept de base de la photopolymérisation

Les photopolymères ou les résines activées par la lumière sont des matériaux polymères sensibles à la lumière qui changent de propriétés lorsqu'ils sont exposés à la lumière. Habituellement, les photopolymères sont conservés à l'état liquide pour un usage général et ne peuvent être durcis qu'avec des sources de lumière (laser UV, lampe, diodes électroluminescentes (LEDs), etc.). La lumière de ces sources déclenche des réactions chimiques qui modifient leurs propriétés chimiques et mécaniques, ces

changements se manifestent souvent au niveau de la structure, pour finalement changer leur état de substance liquide en substance solide. La **Figure 5-2**(a) montre le schéma du principe de la photopolymérisation.

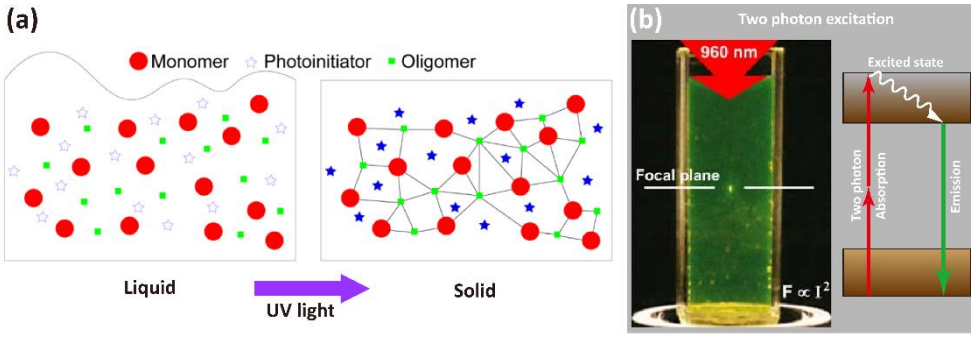

Figure 5-2 (a) L'énergie UV frappe les molécules du photo-initiateur, transmettant l'énergie à d'autres composants. Cela stimule le processus de réticulation entre les molécules et fait passer le polymère exposé de l'état liquide à l'état solide; (b) profils d'excitation de deux photons, un laser de 960 nm utilisé dans le TPA, le faisceau laser est focalisé dans un point du plan focal. Dans les diagrammes de Jablonski, deux photons ayant deux fois la longueur d'onde sont absorbés. (Image reproduite de [59])

La polymérisation à deux photons (TPP) a été proposée pour la première fois par S. Maruo en 1997, et dans laquelle l'énergie nécessaire pour exciter l'électron de l'état fondamental à l'état excité est fournie par deux photons avec environ la moitié de l'énergie [58]. Cet effet optique non linéaire, appelé absorption à deux photons (TPA), représente la règle qui sous-tend la méthode TPP. Comme l'énergie du laser s'échelonne inversement à la longueur d'onde selon la loi de Planck, la moitié de l'énergie signifie deux fois la longueur d'onde du photon en absorption à un seul photon. Cela entraîne plusieurs avantages distincts. Les grandes longueurs d'onde utilisées pour l'excitation à deux photons sont moins dommageables et pénètrent plus profondément dans l'objet/la résine que celles utilisées pour l'excitation à un seul photon. Et le TPA n'est obtenu qu'à proximité du point focal, ce qui entraîne peu de réaction dans les régions situées au-dessus et au-dessous du plan focal. La **Figure 5-2**(b) montre les mécanismes d'excitation du TPA.

5.1.3 Incorporation de nanocristaux dans un photopolymère

Les polymères sont attrayants non seulement par leurs possibilités technologiques, mais aussi pour leurs propriétés optiques. Comme les polymères sont des matériaux de mise en solution, ils peuvent facilement agir comme des matrices de différents composés de nanoparticules pour leur conférer des propriétés supplémentaires [45]. Récemment, la solution de polymères-QDs ayant d'excellentes propriétés optiques et une inertie chimique a été démontrée par un simple mélange de polymères photosensibles et de composants QDs dans des proportions raisonnables [52-54]. L'incorporation de points quantiques semi-conducteurs colloïdaux dans les polymères est apparue comme une technologie alternative pour former des nanocomposites. De cette façon, les QDs pourraient être simplement introduits dans des dispositifs à l'état solide après la création du motif polymère. Et un nanocomposite polymère contenant des nanocristaux semi-conducteurs donne un matériau flexible qui combine les propriétés actives des nanocristaux avec les possibilités technologiques des matrices polymères [45,55]. Il a été démontré que les QDs intégrés ont des propriétés optiques similaires à celles des QDs libres [56]. Par conséquent, un nanocomposite QD-polymère est un matériau potentiel à utiliser dans de futurs dispositifs optiques photoniques intégrés.

5.1.4 Nanoémetteurs plasmoniques hybrides

Notre groupe a également proposé d'intégrer les nanoémetteurs basés sur des structures polymères contenant des QDs à différentes structures plasmoniques. Nous souhaitons en effet appliquer les nano-émetteurs basés sur des polymères QDs sur différents systèmes.

Nanoémetteurs polymérisés couplés à des nanofils d'argent:

Les SP sont des ondes électromagnétiques de surface qui se propagent dans une direction parallèle à l'interface métal/diélectrique [64]. Les nanofils d'argent (Ag-NW) sont des nanostructures métalliques qui supportent des SP de propagation qui peuvent être lancés ou détectés aux extrémités du nanofil [65,66]. Ici, nous utilisons une

méthode encore plus rapide et plus simple pour intégrer les QDs près des structures plasmoniques avec une position hautement contrôlée. Notre méthode est basée sur une technique d'écriture directe au laser basée sur le TPP. Le schéma du système nanoplasmonique hybride basé sur des QDs et un nanofil d'argent est présenté à la **Figure 5-3**(a). La **Figure 5-3**(b) montre une image MEB typique d'un nanofil d'argent. Les Ag-NW monocristallins cultivés chimiquement sont caractérisés par des surfaces lisses sans défauts et des extrémités facettées, comme le montre l'encart (i) de la **Figure 5-3**(b). En focalisant un laser de 514 nm sur l'extrémité Ag-NW, les SP pourraient être excités par diffusion, générant ainsi une large gamme de vecteurs d'ondes hautes dans le plan qui correspondent à la fonction de dispersion des SP à cette longueur d'onde. Et les SPs ont la sélectivité de polarisation, montrée dans l'encadré (ii) et (iii) de la **Figure 5-3**(b). Les résultats présentés ci-dessus montrent également la possibilité de la technique d'écriture directe par laser basée sur le TPP pour l'intégration de nanoémetteurs sur des puces photoniques à nanostructures complexes.

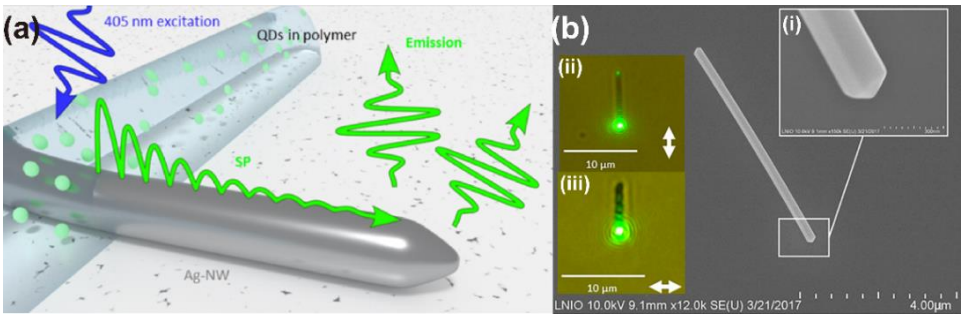

Figure 5-3 schéma conceptuel du couplage entre des points quantiques contenant une structure polymère et des plasmons de surface (SP) supportés par un nanofil d'argent (Ag-NW); (b) Image MEB d'un nanofil d'argent typique sur un substrat de Si. Encadré: (i) Zoom sur les détails à l'extrémité du nanofil, (ii) et (iii) SPs excités/non excités avec la polarisation du laser d'excitation parallèle/perpendiculaire à l'axe. (Image prise à partir de [60])

Emetteur unique polymérisé couplé à une nanoparticule métallique:

Une approche simple de polymérisation à deux photons basée sur le plasmon a été proposée pour intégrer les nanoémetteurs sur les nanoparticules métalliques

correspondantes. Ici, nous avons poursuivi ce TPP à base de plasmon pour les nanodisques, les nanostars et les nanocubes, comme le montre la **Figure 5-4**. La plupart des nanoémetteurs hybrides signalés ne contiennent qu'une seule couleur de sortie. En plasmonique hybride impliquant des émetteurs, le changement de la couleur d'émission nécessite le changement des colorants. La procédure de fabrication comprend deux étapes. La première étape consistait à polymériser le long de l'axe X pour positionner les QDs verts dans la direction X. La seconde a consisté à recouvrir l'échantillon avec les QDs rouges. La **Figure 5-4**(a) montre l'image MEB des émetteurs à base de nanodisques (d = 90 nm) avec deux points quantiques différents. La signature du positionnement spatial sélectif des QDs est représentée par les images de fluorescence en champ lointain de l'émetteur à base de nanodisques (**Figure 5-4** (b)). La technique de fabrication du TPP à base de plasmon est également applicable à des nano-étoiles, comme le montre la **Figure 5-4**(c) et (d). Là encore, la longueur d'onde dominante peut être sélectionnée en faisant tourner la polarisation de la lumière incidente. Un autre exemple que nous avons poursuivi est celui des nanocubes d'or déposés sur un substrat de verre revêtu d'oxyde d'indium-étain (ITO). La **Figure 5-4**(e) montre l'image MEB de l'émetteur à base de nanocubes obtenue avec une lumière incidente parallèle à la diagonale du cube à 45° par rapport aux axes x, y. La **Figure 5-4**(f) montre l'intensité de son PL en fonction de l'angle de polarisation incident. Le niveau PL varie rapidement en fonction de la direction de polarisation de l'excitation, ce qui donne les états "on" et "off", appelés respectivement "état 1" et "état 0". Ce contrôle du niveau PL permet donc de nouvelles perspectives dans le domaine de la nanoplasmonique hybride.

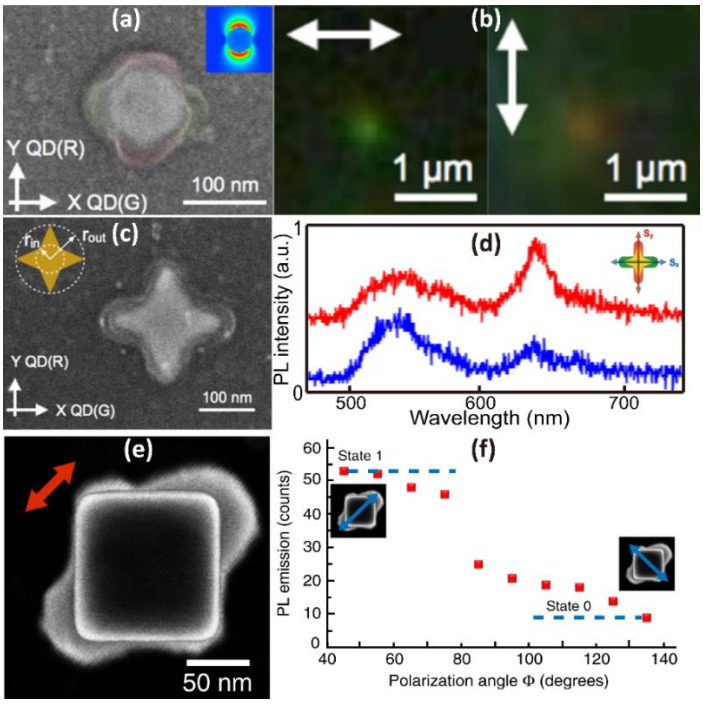

Figure 5-4 (a) Image MEB du nanodisque après la deuxième exposition qui piège les QDs rouges le long de l'axe Y (l'intensité du champ proche plasmonique de l'émission dipolaire pour la deuxième exposition est indiquée dans l'encadré); (b) Image de fluorescence en champ lointain des émetteurs à base de nanodisques sous illumination avec la polarisation de l'axe X et la polarisation de l'axe Y; (c) Image MEB de l'émetteur à base de nanostar; (d) Spectres de fluorescence collectés avec la polarisation de la lumière bleue d'excitation le long de l'axe X (bleu) et de l'axe Y (rouge); (e) Image MEB de l'émetteur à base de nanocube; (f) Intensité du PL en fonction de l'angle de polarisation de la lumière d'excitation. (Image reproduite de [39,61])

En diminuant la concentration des QDs dans la solution de polymère originale, un seul QD ou quelques QD peuvent être piégés à l'intérieur des lobes de polymère de l'émetteur hybride à base de nanocubes, ce qui étend la possibilité de l'émetteur hybride au régime de photon unique. La **Figure 5-5**(a) montre l'image AFM d'un émetteur hybride à base de nanocubes d'or. La **Figure 5-5**(b) montre le résultat de la mesure de la fonction d'autocorrélation $g^{(2)}$ correspondante. À un retard nul, $g^{(2)}(0)$ est d'environ 0,35, ce qui est inférieur à 0,5. C'est la signature d'une émission de photons unique [88]. Ce résultat ouvre la voie aux nano-émetteurs accordables commandés par la polarisation et même aux émetteurs de photons uniques

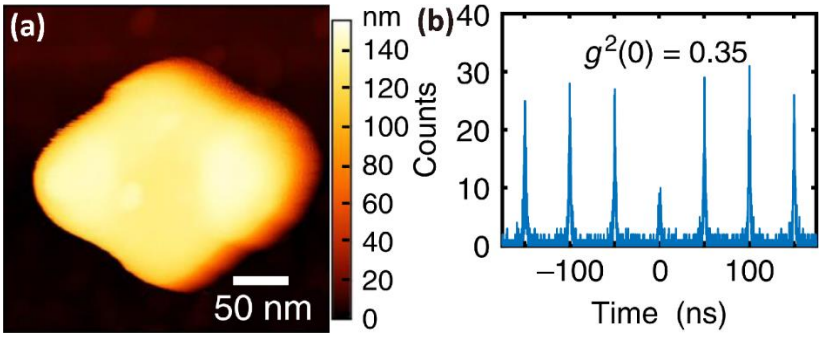

Figure 5-5 (a) AFM d'un nanoémetteur hybride basé sur un nanocube. Les lobes du polymère contiennent un seul ou quelques QD; (b) Mesure de la fonction d'autocorrélation $g^{(2)}$ (0) = 0,35

5.1.5 Guides d'ondes à échange d'ions à base de verre (IEWs)

Le verre est un matériau optique bien connu et les plaquettes de verre sont naturellement oxydées et plus économiques que les plaquettes de silicium. Les guides d'ondes en verre présentent plusieurs avantages, notamment leur faible coût, leur compatibilité avec les fibres optiques commerciales et leur faible perte de propagation. Par conséquent, le guide d'ondes à base de verre est un candidat parfait pour la plate-forme photonique intégrée dans notre travail. Dans notre situation, les guides d'ondes enterrés en surface avec une distribution d'indice de réfraction à gradient en section transversale ont été choisis. Ils sont particulièrement indiqués pour la détection, car la lumière guidée près de la surface peut interagir efficacement par couplage évanescent ou hybride avec les structures situées au-dessus [89,90]. Le processus de fabrication de base est illustré à la **Figure 5-6**(a). Après avoir échangé les ions Na^+ contenus dans une matrice de verre par des ions Ag^+ à l'aide d'un masque, le guide d'ondes à ions échangés à indice de réfraction gradué est créé sur le verre de substrat de surface. La **Figure 5-6**(b) donne une vue en coupe de la distribution de l'indice de réfraction d'un guide d'onde à échange d'ions. Les dimensions de la largeur et de la profondeur de diffusion se situent toutes deux autour de 2 μm. La position située au centre de la surface du guide d'ondes a l'indice de réfraction maximal n = 1,57. Tous les échantillons d'IEWs ont été fabriqués et offerts par la coopération TEEM PHOTONIS. Le faible contraste d'indice de

réfraction entre le noyau et le substrat de verre permet un faible confinement de la lumière, ce qui peut être avantageux pour la polymérisation avec les ondes évanescentes liées à la surface.

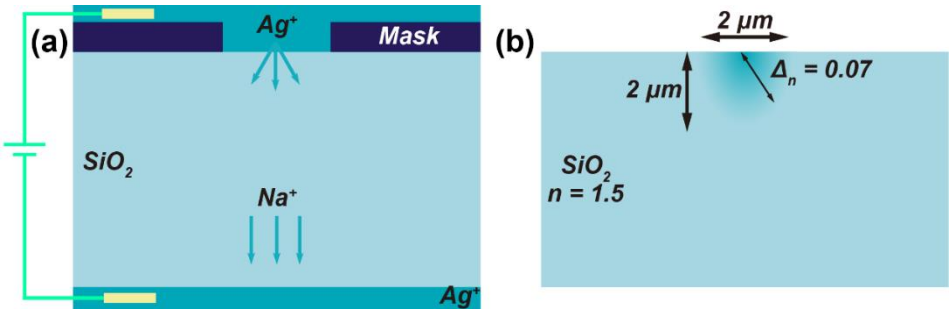

Figure 5-6 (a) Procédé de fabrication d'un guide d'ondes à échange d'ions, un champ thermique externe est appliqué pour faciliter la migration des ions Ag^+ dans le verre. Pendant ce temps, les ions Na^+ échangés se déplacent dans la cathode; (b) Vue en coupe de la distribution de l'indice de réfraction d'un guide d'onde échangeur d'ions.

5.2 Nano-émetteurs polymérisés par ondes évanescentes guidées (GEM)

Deux grandes expériences de photopolymérisation sont proposées. Dans un cas, la résine polymère est coulée directement sur la surface d'un guide d'ondes et absorbe l'énergie de l'onde évanescente de surface pour déclencher le processus de photopolymérisation. Dans l'autre cas, une couche diélectrique (TiO_2) à indice de réfraction élevé est prédéposée sur la surface du guide d'ondes pour transférer la lumière guidée dans la couche de TiO_2. La résine polymère est ensuite déposée par-dessus et le processus de photopolymérisation est déclenché par l'énergie lumineuse qui se trouve à la surface du TiO_2.

5.2.1 Dispositif expérimental basé sur le GEM

Notre dispositif expérimental maison utilisé pour la mise en œuvre de la photopolymérisation comprend deux lasers, comme le montre la **Figure 5-7**. Ici, un laser d'excitation vert de 532 nm est utilisé pour se coupler à nos guides d'ondes, ce qui

donne une onde évanescente de surface qui est ensuite fortement absorbée par la résine polymère et déclenche le processus de photopolymérisation. Un laser rouge supplémentaire de 640 nm, longueur d'onde à laquelle la résine polymère n'est pas sensible, est utilisé pour l'alignement du couplage laser par le bord de la fibre avant de passer au laser vert pour la fabrication. Deux lasers sont ainsi focalisés dans un séparateur à fibre optique à l'aide de lentilles d'objectif, puis connectés à une fibre monomode conique, comme le montre l'encart de la **Figure 5-7**. L'extrémité de la fibre conique réduit la zone de mode afin d'obtenir un meilleur couplage au guide d'onde [100]. Comme pour la mesure de la puissance laser de sortie du cœur de la sortie du guide d'ondes, une lentille d'objectif 20× est approchée de l'extrémité du guide d'ondes correspondant afin d'étendre le faisceau laser de sortie et d'observer le couplage. En outre, un trou d'épingle est utilisé pour séparer la lumière du noyau, puis mesurée avec un instrument de mesure de puissance derrière l'échantillon. La lumière transmise est envoyée dans une lentille d'objectif sur l'échantillon et transférée à une caméra CCD pour l'observation.

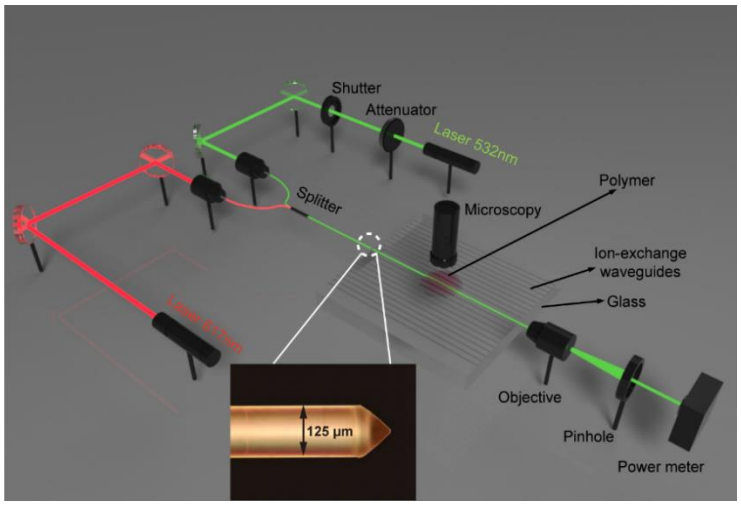

Figure 5-7 Installation expérimentale pour les ondes évanescentes guidées.

L'encadré montre les détails de la pointe de fibre conique.

5.2.2 Optimisation de la stabilité de l'installation

L'efficacité du couplage de la lumière entre la fibre conique et le guide d'ondes est sensible aux vibrations mécaniques de l'installation. Il est donc nécessaire d'optimiser le couplage laser et la stabilité mécanique de l'installation avant de passer de la source laser au laser vert.

Premièrement, nous avons réduit la longueur de la partie aérienne de la fibre *l* de 3 cm à 1 cm, comme le montre la **Figure 5-8**(a). Comme l'échantillon d'IEW et la fibre sont fixés sur les étages, le couplage bout à bout n'est facilement affecté que par la position de la partie aérienne de la fibre en raison du poids de la fibre.

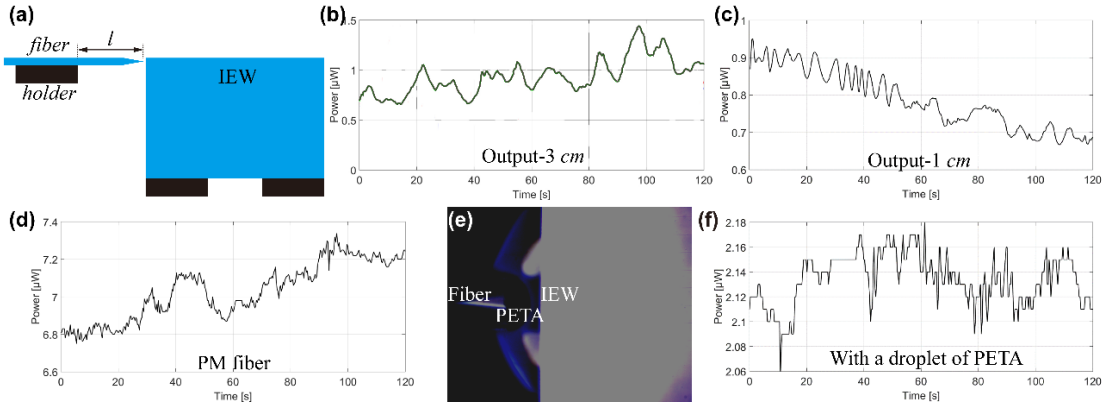

Figure 5-8 (a) Etape de couplage bout à bout. La fibre et l'échantillon d'IEW sont tous deux fixés sur des étages mobiles; Puissance laser de sortie mesurée avec une partie aérienne à 3 cm (b) et 1 cm (c); (d) Puissance laser de sortie mesurée avec une fibre PM; (e) Ajout d'une gouttelette de PETA fixée entre la fibre et l'IEW; (f) Puissance laser de sortie mesurée avec une gouttelette de PETA.

Ici, un laser de 640 nm a été couplé dans un guide d'ondes et nous avons mesuré la puissance de sortie du laser Pout en fonction du temps, comme le montre la **Figure 5-8**(b) et (c). Afin de comparer la stabilité avant et après la réduction *l*, les erreurs mesurées sont calculées par l'équation **(5-1)** ci-dessous, et la E_{out} diminue de 83,6% à 37%.

$$E_{out}=\frac{P_{max}-P_{min}}{P_{average}} \quad (5\text{-}1)$$

Où P_{max} et P_{mi} sont respectivement les puissances de sortie maximale et minimale du laser que nous avons pu mesurer en 120 *s*. $P_{average}$ est la valeur moyenne calculée.

La deuxième source potentielle de vibrations provient du type de fibre utilisé. Les fibres optiques à maintien de la polarisation (PM) sont le candidat parfait pour préserver la polarisation du laser en cours de propagation [101]. Comme le montre la **Figure 5-8**(d), l'erreur calculée E_{out} est de 8,39%, ce qui est bien inférieur à l'utilisation des fibres SM coniques standard (37% dans la **Figure 5-8**(c)). Cela indique qu'une puissance laser de sortie plus stable peut être obtenue en utilisant des fibres à maintien de la polarticipation.

Une autre approche a été envisagée pour augmenter la stabilité de la condition de couplage en utilisant l'huile d'immersion comme milieu intermédiaire entre la fibre et le guide d'onde, comme le montre la **Figure 5-8**(e). Ici, une gouttelette de résine polymère PETA sans points quantiques ni photoinitiateurs a été placée dans l'espace entre une pointe de fibre clivée et un bord de guide d'onde correspondant. L'indice de réfraction de la résine polymère PETA est presque le même que celui de la fibre de verre et de notre noyau de guide d'onde. Dans cette configuration, la réflexion de la lumière peut être ignorée en raison d'un indice de réfraction très proche. Un autre avantage de cet inter-moyen est d'augmenter l'ouverture numérique (N.A). du guide d'onde et de la fibre afin d'obtenir plus de lumière laser couplée dans nos guides d'onde [102]. Comme le montre la **Figure 5-8**(f), l'erreur de sortie laser mesurée E_{out} a encore diminué pour atteindre 5,62%, soit environ 15 fois plus que la stabilité obtenue en utilisant la fibre avec une pointe aérienne trop longue (83,6% dans la **Figure 5-8**(b)).

5.2.3 Caractérisation de la transmission de la lumière

La caractérisation des propriétés de transmission de la lumière de notre IEW est nécessaire pour comprendre la photopolymérisation qui se produit au sommet. Comme le montre la **Figure 5-9**(a-c), la lumière de sortie est élargie par une lentille d'objectif et le spot de sortie du laser rouge observé est beaucoup plus brillant que le spot de sortie

du laser vert. Les lasers vert et rouge peuvent être couplés dans la IEW, comme le montre la **Figure 5-9**(d) et (e). L'intensité de la couleur de la fuite de lumière des guides d'ondes peut être mesurée par la caméra CCD montée au-dessus de la lentille de l'objectif d'observation, comme le montre la **Figure 5-9**(f) et (g). Les intensités lumineuses sont tombées à *1/10* de la valeur à la position initiale pour la lumière verte et à *1/5* pour la lumière rouge, ce qui donne des constantes d'atténuation de -10 *dB/cm* et -7 *dB/cm*, respectivement.

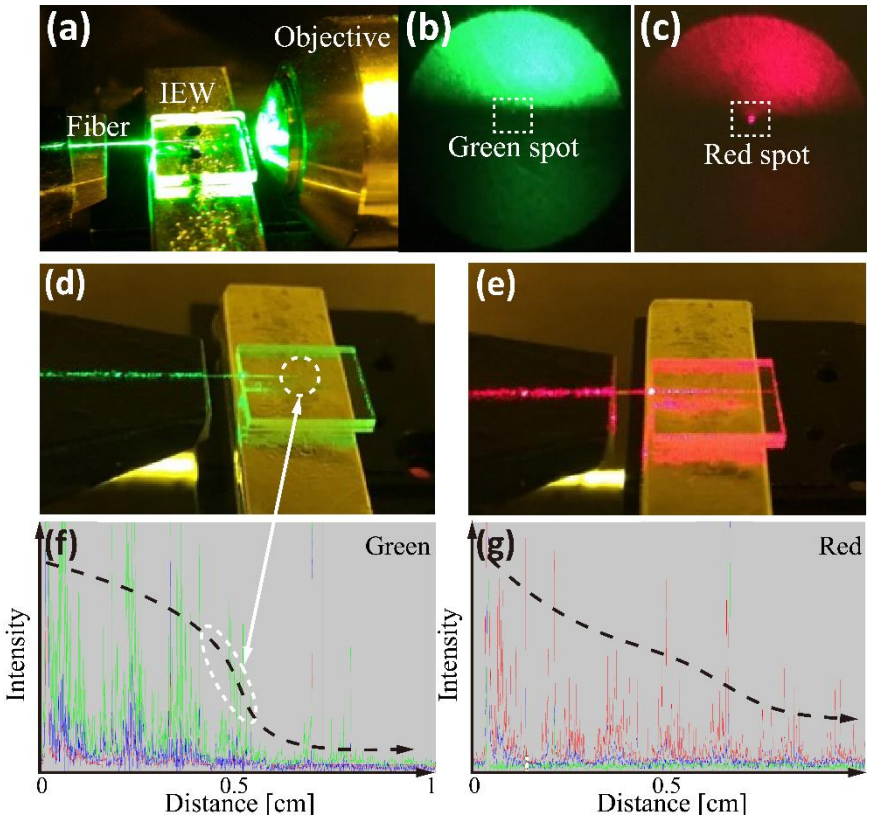

Figure 5-9 (a) Objectif de microscope collecteur pour élargir la distribution de la lumière de sortie; Point vert (b) et point rouge (c) de sortie; Laser vert (d) et laser rouge (e) couplés à l'IEW; Distribution de l'intensité des couleurs des images CCD pour le laser vert (f) et le laser rouge (g) se propageant le long des guides d'ondes.

5.2.4 Crêtes polymériques sur les IEW

Nous discutons d'abord de nos capacités à contrôler la taille de notre résine polymère sans points quantiques dispersés à l'intérieur en changeant le laser d'excitation couplé et le temps d'exposition. Ensuite, une résine polymère incorporée avec des QDs est utilisée pour créer des crêtes de QDs dont les émissions ont également été enregistrées par notre système de mesure PL maison.

Crêtes de polymères sans QDs:

Une petite gouttelette de polymère sans QDs a été coulée sur la surface de l'IEW à la surface des guides d'ondes fabriqués avant d'ajuster le couplage d'entrée du laser rouge. Ici, en contrôlant le temps d'exposition, nous avons obtenu des crêtes de différentes dimensions, comme le montre l'image AFM de la **Figure 5-10**, la largeur de la crête varie de 1,8 à 3,33 μm, ce qui est comparable à la largeur du cœur du guide d'ondes (2 μm). Et la hauteur des crêtes augmente de 23 à 255 nm.

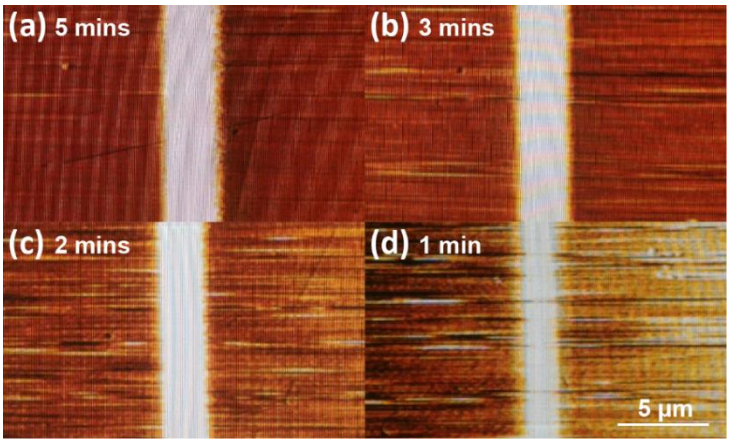

Figure 5-10 Images de mesure AFM de crêtes polymères réalisées avec le mélange R_1 pendant 5 min (a), 3 min (b), 2 min (c) et 1 min (d).

Crêtes de polymères avec QDs:

Une deuxième expérience a été réalisée afin de créer des crêtes de polymère incrustées de points quantiques. La **Figure 5-11**(a) montre la crête de polymère minimale obtenue à 1 min et 15 *nW*, la largeur et la hauteur mesurées sont de 1,81 μm et 16,33 nm (**Figure 5-11** (b)). La **Figure 5-11**(c) montre la crête la plus grande obtenue à 5 min et 15 *nW*, dont la largeur est de 2,69 μm et la hauteur de 84,4 nm (**Figure 5-11**

(d)). En particulier, la crête de 16,33 nm de hauteur est un résultat important, car elle est à peine plus grande que le diamètre moyen de nos points quantiques, qui est généralement d'environ 15 nm. À l'avenir, notre technique pourra donc être utilisée pour fabriquer des guides d'ondes polymères contenant une seule couche de nano-émetteurs.

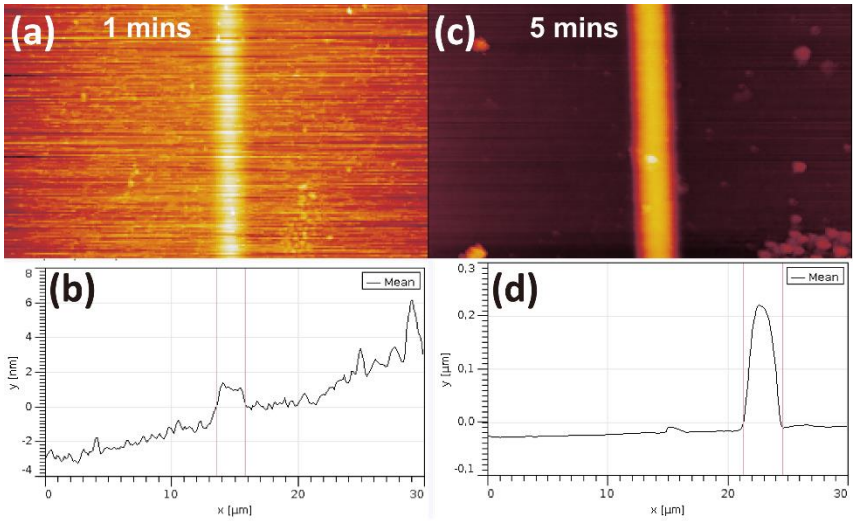

Figure 5-11 Résultats des mesures AFM des crêtes polymères faites par le mélange R_2 avec des temps d'exposition de 1 min (a-b) et 5 min (c-d).

5.2.5 Crêtes polymères sur la couche de TiO_2 des IEW

La longueur des crêtes polymérisées dépend de la dimension de la photorésine étalée sur la surface. Il est nécessaire de confiner la lumière dans un volume à l'échelle nanométrique et donc non seulement en hauteur, mais aussi en longueur et en largeur. Sur la base de nos travaux précédents [92], la présence de TiO_2 assure un confinement optimal de la lumière et un couplage efficace avec le guide d'onde en verre IEW situé en dessous. Il pourrait s'agir d'une nouvelle méthode d'intégration potentielle pour des applications dans le contexte de la photonique intégrée.

Ici, le dioxyde de titane (TiO_2) a été choisi en raison de sa propagation de la lumière à faible perte et de sa capacité à supporter la lumière visible monomode et multimode [107-109]. En raison de la proximité de l'IEW et de la couche de TiO_2, l'onde évanescente du mode de propagation de l'IEW est capable d'exciter les modes de la

dalle de TiO_2 [110]. La **Figure 5-12**(a) montre les distributions de la lumière de propagation en coupe transversale pour une IEW avec une couche de TiO_2. Ici, la hauteur h de la couche de TiO_2 a été fixée à 180 nm, et la largeur w a été fixée à 2 µm. Une source de mode à 532 nm (mode TM) a été utilisée comme source de lumière dans cette simulation. La distance entre deux positions voisines ayant des intensités lumineuses maximales est définie comme la "longueur de battement (BL)" [115].

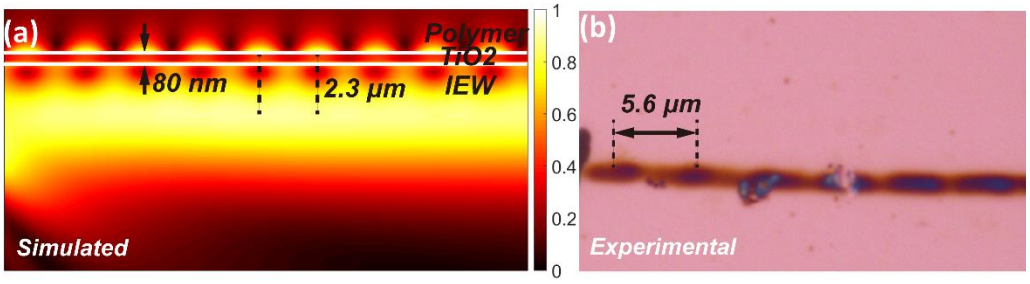

Figure 5-12 (a) La vue latérale de la distribution de la lumière du TiO_2 a couvert les IEW avec une TM fondamentale couplée aux IEW propageant la lumière à 532 nm. La ligne blanche représente le profil du champ électrique; (b) chaîne de QD-polymère fabriquée par l'expérience GEW sur la couche de TiO_2 déposée sur les IEW. Les lignes blanches représentent les contours de la couche de TiO_2.

Ensuite, une plaque de TiO_2 d'une hauteur de 83 nm a été déposée sur des IEW, et nous avons couplé le mode TM du laser vert dans un guide d'ondes IE pour déclencher le processus de photopolymérisation. Après avoir retiré la photorésine non exposée, une chaîne de QD-polymère est apparue, comme le montre l'encadré de la **Figure 5-12**(b). Les épaisseurs mesurées du pic et de la vallée de cette chaîne QD-polymère étaient d'environ (h_p = 64 ± 2 nm, h_v = 45 ± 2 nm). Il est intéressant de noter que nous avons trouvé que la période de la chaîne de QD-polymère est de 5,6 µm, ce qui est différent de notre valeur simulée (BL = 2,3 µm alors que h = 80 nm). Cela est probablement dû à la distribution d'incertitude de l'épaisseur effective et de l'indice de réfraction (côté

croisé) de cette structure hybride. Nos travaux précédents ont également été réalisés pour analyser ce phénomène [120].

5.3 Nanoémetteurs polymérisés par écriture directe au laser - Polymérisation à deux photons (DLW-TPP)

Dans ce chapitre, le procédé d'écriture directe par laser basé sur la polymérisation à deux photons est utilisé afin de réduire la dimension des structures polymères incrustées de points quantiques, ce qui ouvre une nouvelle voie pour l'intégration déterministe d'émetteurs quantiques sur des dispositifs photoniques.

5.3.1 Technique d'écriture directe au laser basée sur le TPP

Le processus standard DLW-TPP est exécuté avec une imprimante Nanoscribe Professional GT (**Figure 5-13**(a)) qui est alimentée par un laser femtoseconde dans le proche infrarouge à 780 nm, fonctionnant avec une durée d'impulsion de ~100 fs et une fréquence de répétition de 80 MHz et une puissance moyenne maximale de $P_{max} \approx 20$ mW (mesurée après l'objectif de focalisation) [122 123]. La photoréserve est coulée au goutte-à-goutte sur une lamelle de verre transparent de 22×22×0.17 mm^3 montée sur des étages de traduction piézoélectrique x-y-z imagées par un objectif de microscope optique haute résolution 100× à huile d'immersion, comme le montre la **Figure 5-13**(b). Dans cette configuration DLW-TPP classique, une distance de travail typique de l'objectif d'immersion dans l'huile est inférieure à 170 μm, Il est nécessaire de développer une configuration DLW-TPP capable de transférer des nanocomposites de QD-polymère sur des substrats optiques plus épais, dans notre travail, des substrats en verre à base d'IEW. La création d'un espace mince entre un substrat et une lamelle de couverture est une approche prometteuse pour utiliser des substrats plus épais par système d'écriture laser. Comme le montre la **Figure 5-13**(c). Les micro-fils sont placés parallèlement à la surface de la lamelle de couverture. La résine photopolymère (monomère PETA) contenant des points quantiques CdSe/ZnS colloïdaux est placée

dans l'espace grâce. Ensuite, le laser est focalisé à l'interface entre le liquide polymère et le substrat pendant le processus de structuration (**Figure 5-13**(d)). Après la photopolymérisation, la partie non exposée du liquide photopolymère est ensuite éliminée dans une solution d'acétone, ce qui donne un nanocomposite de QD-polymère sur le substrat épais.

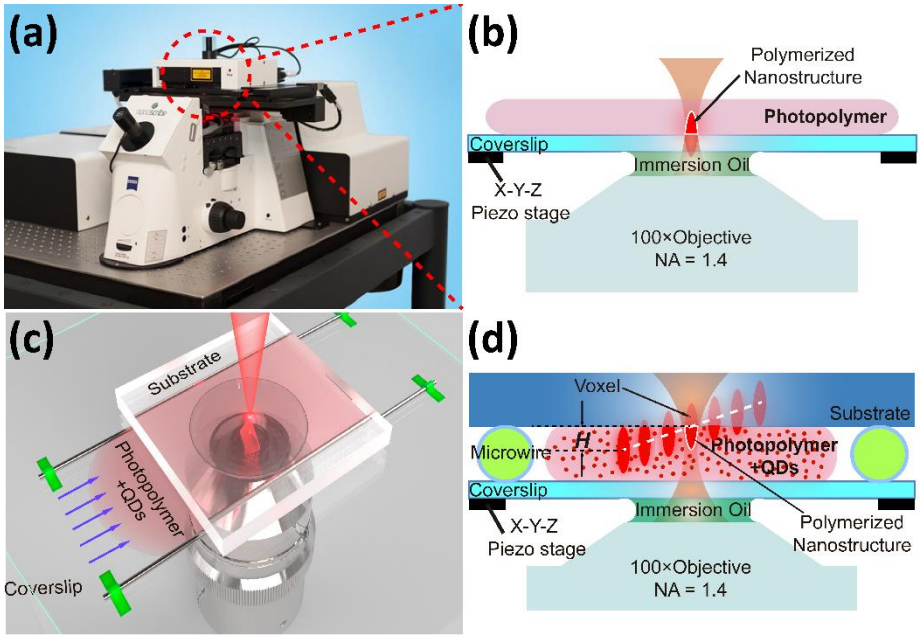

Figure 5-13 (a) Plate-forme d'impression Nanoscribe Professional GT; (b) Principe d'impression laser conventionnel basé sur la polymérisation de deux photons; Illustration 3D (c) et principe de base (d) de la plate-forme DLW-TPP développée.

5.3.2 Étude des paramètres d'impression sur les substrats en verre

Nous étudions systématiquement la dépendance de la taille des nanostructures de QD-polymère par un réseau fabriqué de 6 × 5 voxels (avec des pas de 1 μm) sur des substrats de silice tout en ajustant la puissance d'impression laser *P*, l'exposition *T* et la hauteur focale *H*. La **Figure 5-14**(a) montre l'image MEB des voxels de nanostructures de QD-polymère avec différents *P* et *T*, tandis que la **Figure 5-14**(b) montre un réseau de voxels de QD-polymère pour étudier la possibilité de réduire davantage la taille des voxels en ajustant soigneusement *H*. Les dépendances de la taille des voxels sur *P*, *T* et *H* sont montrées dans la **Figure 5-14**(c-e), respectivement. Il est évident que le diamètre

et la hauteur des voxels peuvent être contrôlés avec une grande précision spatiale. La dimension des structures de voxels peut être réduite à ~ 17 nm de hauteur et ~ 125 nm de diamètre (avec P = 10 mW, T = 1 ms)

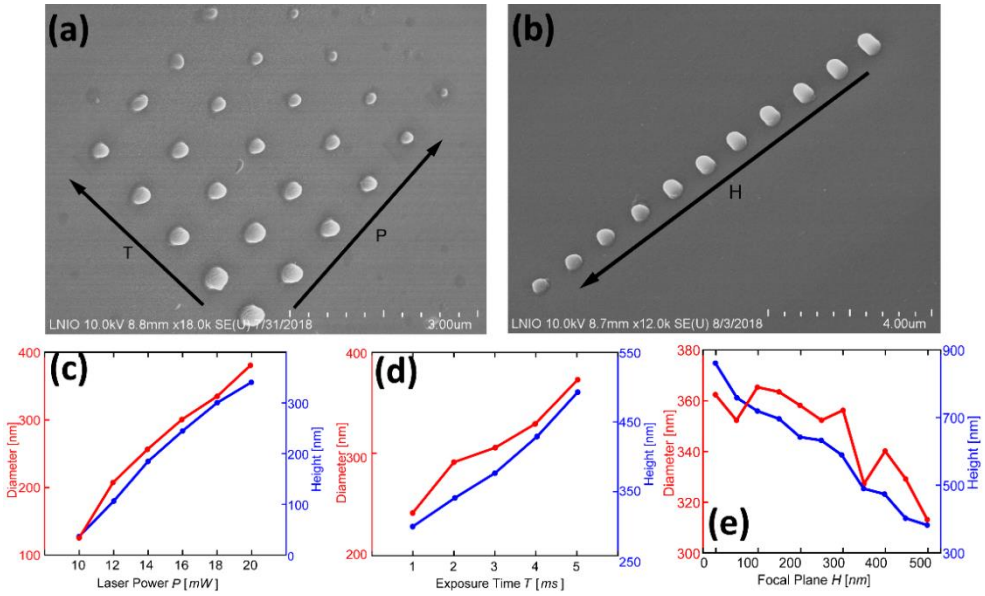

Figure 5-14 Caractérisation des voxels de QD-polymère. (a) Image MEB d'un réseau de voxels en modifiant la puissance du laser P (10 - 20 mW avec un pas de 2 mW) et le temps d'exposition T (1 - 5 ms avec un pas de 1 ms), la valeur par défaut H dans cet échantillon est de 0 nm; (b) Image MEB d'un réseau de structures de voxels simples en ajustant la hauteur focale du laser H (0 - 450 nm avec un pas de 50 nm, le long de la flèche noire); (c-e) Dépendance de la hauteur et du diamètre des structures de voxels simples en fonction de P, T et H respectivement. T = 5 ms pour (c), P = 20 mW pour (d), H = 20 mW et P = 5 ms pour (e).

En raison de l'importance dans la définition de la propriété de fluorescence des QDs, nous avons mesuré la photoluminescence émise par chaque voxel. Ici, nous avons augmenté la distance entre les voxels de 1 µm à 5 µm, afin d'éviter l'illumination par les voxels voisins. La **Figure 5-15**(a) montre l'imagerie microscopique d'un réseau de voxels individuels. La source d'excitation est une LED bleue (450 nm) dans un champ

de vision de ≈ 30 × 10 μm2. La lumière émise a été filtrée par un filtre passe-long (LPF) de 530 nm et enregistrée par une caméra CCD à multiplication d'électrons. Les points lumineux (**Figure 5-15**(b)) de différentes intensités sont clairement visibles et correspondent à l'émission de QDs des voxels, comme le montre la **Figure 5-15**(c) and (d). Le contraste entre les deux images révèle la lumière émise par les QDs à l'intérieur des voxels polymères. Il s'avère que les QDs peuvent être piégés dans les structures polymériques.

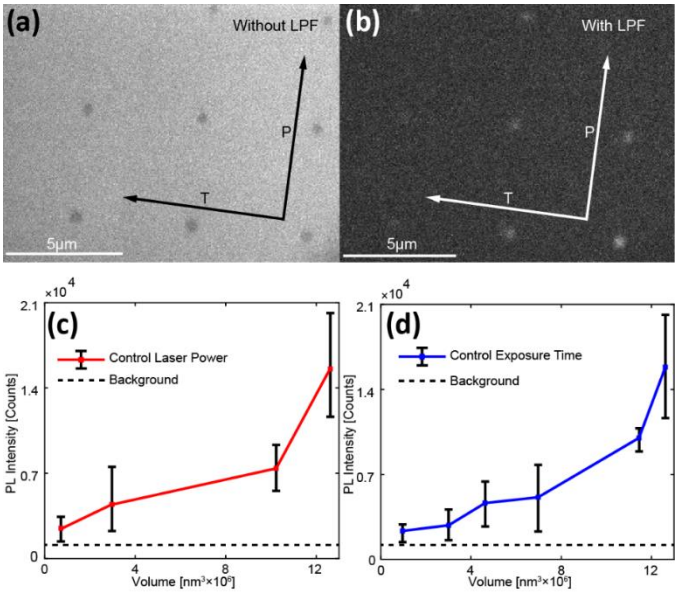

Figure 5-15 Images CDD de la matrice de voxels éclairées par une LED de 404 nm sans (a) et avec (b) un LPF de 530 nm; Relation entre l'émission de QDs et le volume de voxels en ajustant *P* (c) et *T* (d). Les lignes pointillées représentent l'émission de fond.

5.3.3 Nanoémetteurs intégrés aux IEW

Grâce à la technique d'écriture laser optimisée, nous avons réussi à créer des composites QD-polymère à l'échelle nanométrique au centre d'une surface IEW. En excitant les nanoémetteurs intégrés avec un laser externe, nous avons obtenu l'émission à l'extrémité du guide d'ondes qui a montré la preuve d'une émission des QDs couplée au guide d'ondes.

Fabrication de nanocomposites à base de QD-polymère sur des IEWs:

Sur la base des paramètres d'impression empiriques, nous avons fabriqué des nanocomposites à base de QD-polymère sur des IEW. Comme le montre les **Figure 5-16**(a) et (b), trois voxels de nanoparticules de QD-polymère (temps d'exposition de 3 *ms*, 2 *ms* et 1 *ms*) ont été créés sur différents guides d'ondes. La puissance du laser d'impression utilisé pour la photopolymérisation était de 20 *mW*. La **Figure 5-16**(c) et son encart montrent les détails du voxel avec un temps d'exposition de 1 *ms*. Il s'agit des voxels créés pour la mesure de la diffusion. Nous aurions pu créer un voxel plus petit avec une puissance laser d'impression plus faible. Cependant, étant donné que la quantité des QDs diminuerait, entraînant une intensité d'émission des QDs plus faible, il nous aurait été plus difficile de mesurer avec notre système d'expérimentation actuel présenté dans la sous-section suivante.

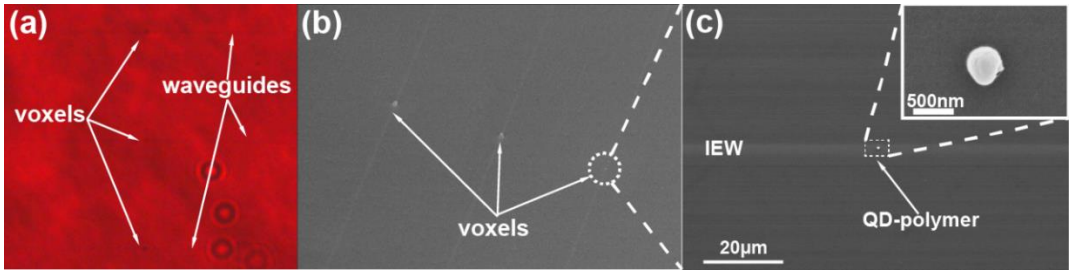

Figure 5-16 Intégration de trois voxels QD-polymère sur différents guides d'ondes comme le montrent l'image microscopique (a) et les images MEB (b, c).

Dispositif de mesure PL couplé à une puce à fibres optiques:

Un dispositif de mesure de la photoluminescence construit à la maison a été utilisé pour détecter l'émission de points quantiques couplée à l'IEW, comme le montre la **Figure 5-17**(a). La fibre monomode d'entrée est alignée à l'extrémité de la facette correspondante du guide d'ondes avec un laser continu de 640 nm pour optimiser le couplage fibre-IEW. Une fois que la fibre d'entrée est correctement alignée, l'échantillon est excité par le haut simultanément en commutant le laser d'excitation à

532 nm par l'intermédiaire d'un objectif de microscope 60×. L'émission QDs couplée aux IEW est collectée et détectée par un spectromètre à réseau refroidi par CCD. L'émission QDs en champ lointain peut également être collectée par une fibre multimode et dirigée à travers un filtre passe-haut de 540 nm vers un autre spectromètre portable commercial.

Le pré-alignement de la fibre et du guide d'ondes nous permet de mesurer l'émission des QDs de la facette du guide d'ondes. La **Figure 5-17**(b) montre l'étage expérimental de couplage fibre-guide d'onde de l'échantillon, la ligne de lumière rouge sur la surface de l'échantillon IEWs indique le laser de 640 nm qui se propage, ce qui indique une efficacité de couplage. La **Figure 5-17**(c) montre l'image microscopique agrandie pour le carré pointillé jaune de la **Figure 5-17**(b). Aucune lumière diffusée entre la fibre et l'IEW n'est observée lorsque le mode fibre optique et le mode guide d'ondes à échange d'ions se chevauchent bien. À la position des voxels de QD-polymère sur le guide d'onde intégré loin de la facette d'entrée du guide d'onde, on observe une tache lumineuse claire due au laser de guidage diffusé par la structure. Cela nous aide à optimiser l'alignement fibre-guide d'onde.

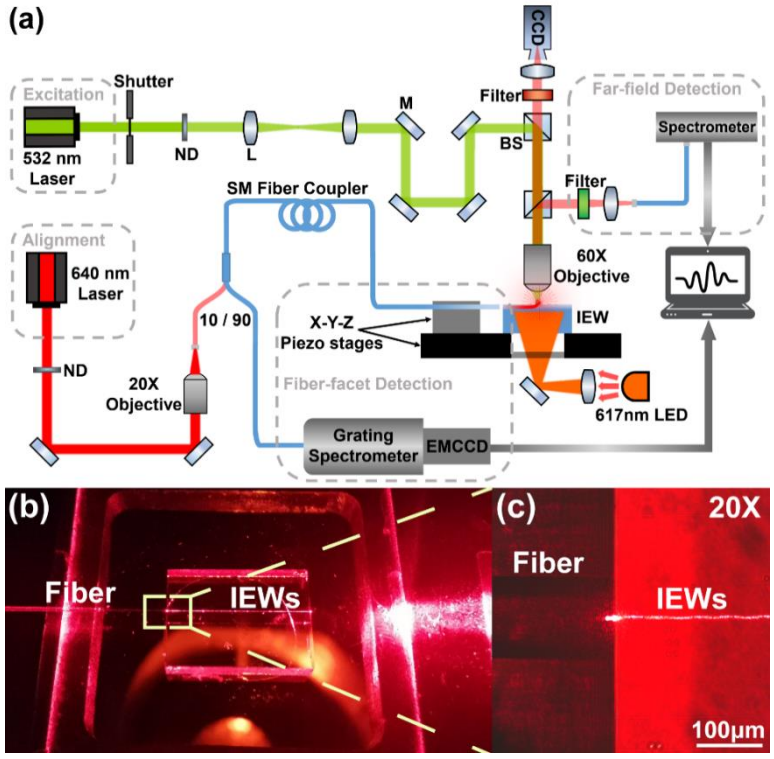

Figure 5-17 (a) Etape expérimentale de couplage fibre-IEWs. (b) Pointe de la fibre couplée avec le bord des IEWs. (c) Partie agrandie du carré jaune en pointillés en (b).

Mesures des émissions des QDs couplées à l'IEW:

La **Figure 5-18**(a) montre le schéma de cette application. Il y a deux façons de détecter l'émission des QDs. Tout d'abord, nous vérifions l'émission des QDs par détection en champ lointain. Le voxel représenté sur la **Figure 5-16**(c) a été utilisé pour la mesure PL. Une émission significative de QDs en champ lointain a été observée dans la **Figure 5-18**(b) (spot d'émission rouge, filtré par un filtre passe-haut de 540 nm). Les résultats montrent la preuve de la présence de points quantiques à l'intérieur des nanostructures de polymère et de leur haute qualité d'émission. Le spectre enregistré montre un pic apparent à 588,5 nm avec un FWHM d'environ 43,1 nm, ce qui est indicatif de nos signatures d'émission de type CdSe/ZnS QDs, comme le montre la **Figure 5-18**(c).

Ensuite, nous avons mesuré l'émission des QDs couplés à un guide d'onde par détection couplée à une fibre. Le résultat montre le spectre extrait qui donne lieu à un pic de luminescence étroit à 591,1 nm avec une FWHM d'environ 8 nm, comme le montre la **Figure 5-18**(d). La longueur d'onde à l'intensité maximale est en très bon accord avec le spectre en champ lointain. Les spectres de haute intensité entre 500 et 560 nm représentent le laser d'excitation à 532 nm. L'émission spectrale large entre 600-700 nm provient de la fluorescence des substrats de la substrats IEWs.

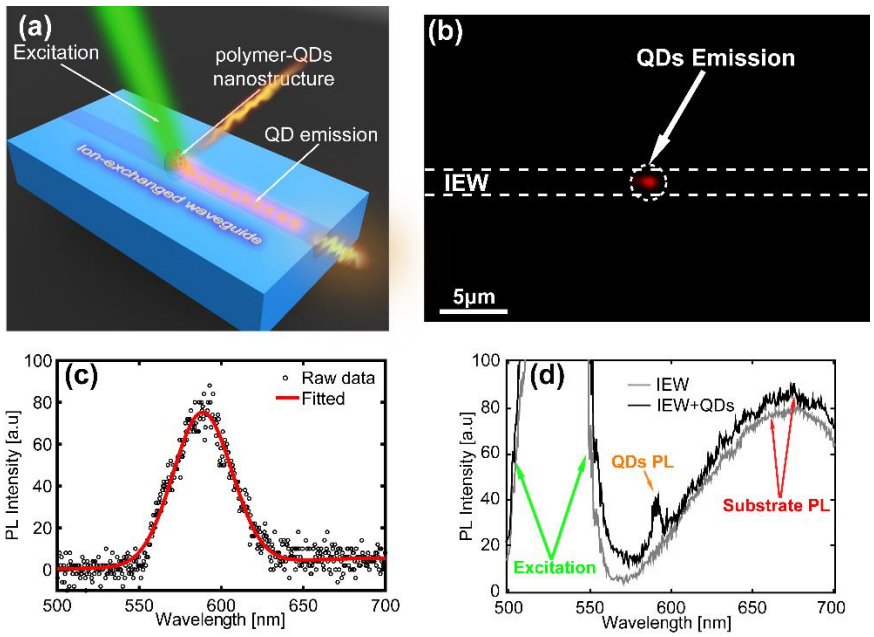

Figure 5-18 (a) Schéma des nano-émetteurs des QDs intégrés dans un guide d'onde; (b) Image CCD de l'émission des QDs (point rouge), la ligne blanche en pointillés représente les contours du guide d'onde; (c) Spectre de l'émission de points quantiques en champ lointain pour une nanostructure unique de QD-polymère sur IEW avec un ajustement gaussien (ligne rouge); (d) Spectre extrait normalisé recueilli à partir de la facette du guide d'onde par une fibre monomode. Ligne noire pour une nanostructure de QD-polymère placée sur une DEI, ligne grise pour une DEI sans QDs.

5.3.4 Émissions de fond du substrat des IEW

On peut remarquer que nous n'avons pas utilisé de laser bleu pour exciter les structures des QD-polymère. C'est parce qu'il existe une forte émission émise par les guides d'ondes eux-mêmes. La **Figure 5-19** montre le spectre d'émission couplé aux guides d'ondes obtenu par l'excitation des QDs avec un laser bleu. Ici, nous avons organisé des mesures de PL en excitant directement les DEI sans aucun voxel de QD-polymère intégré à un laser bleu (404 nm). Il est clair que le pic à 404 nm représente le laser d'excitation, ce qui est également indiqué par une image CCD capturée, comme le

montre l'encart (i) de la **Figure 5-19**, et qu'un autre pic étroit se situe à environ 550 nm, que nous supposons provenir de l'émission d'ions en forme d'éclats introduits dans les IEW au cours du processus d'échange thermique d'ions. En outre, nous avons également trouvé plusieurs articles dans la littérature qui décrivent une émission similaire d'ions argent [145-147]. En outre, une émission à large bande est également observée entre 600 nm et 800 nm, et nous l'avons attribuée à l'émission du matériau en verre. Afin de confirmer cela, nous avons organisé la mesure PL pour le substrat de verre pur, le spectre est montré dans l'encart (ii) de la **Figure 5-19**. Apparemment, l'intensité commence à diminuer à partir d'environ 650 nm, ce qui a une tendance similaire à l'émission des échantillons d'IEW.

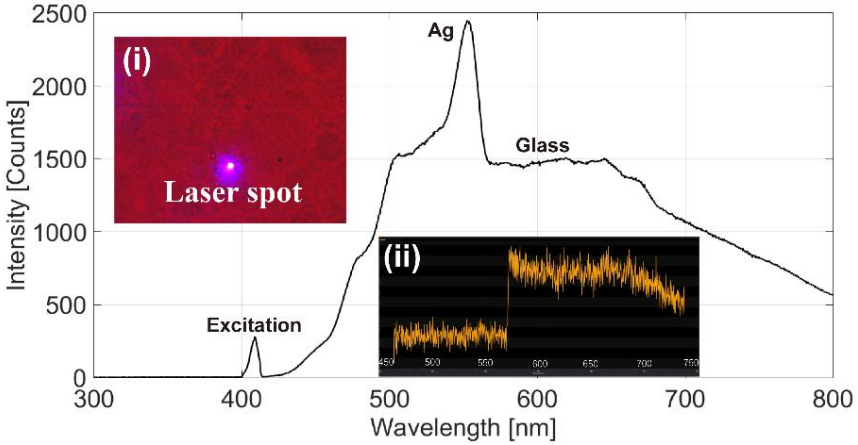

Figure 5-19 La moyenne de 10 spectres PL mesurés. L'encadré (i) montre le spot laser et (ii) montre l'émission d'un substrat en verre pur avec un filtre a été réglé pour filtrer l'émission en dessous de 560 nm.

5.4 Expériences supplémentaires en vue de travaux futurs

Bien que nous ayons démontré la possibilité et la faisabilité en créant des nanocomposites à base de QD-polymère directement sur les IEW au chapitre 3, il existe encore certains problèmes à résoudre, notamment:

iv- La réduction de la fluorescence du bruit des IEW (6.4.1);

v- Comment optimiser l'efficacité du couplage des QDs aux guides d'ondes en utilisant la couche de SiC (6.4.2);

vi- Comment positionner les nanoémetteurs par fonctionnalisation de surface et la technique DLW-TPP (6.4.3).

Ces questions influencent grandement la possibilité d'utiliser la technique DLW-TPP pour nos travaux futurs et certaines solutions partielles ont été mises en œuvre, comme on peut le voir dans les paragraphes suivants.

5.4.1 Réduire l'émission d'ions argent des guides d'ondes

Comme déjà mentionné au chapitre 3, les ions d'argent diffusés à l'intérieur des guides d'ondes à échange d'ions (IEW) à base de verre peuvent émettre de la lumière lorsqu'on utilise un laser à excitation bleue. Il est nécessaire de réduire l'émission de lumière des ions d'argent sous l'éclairage d'un laser bleu. Pour ce faire, nous avons voulu comparer les spectres en excitant une position fixe au centre et sur la surface du guide d'ondes avant et après une irradiation laser à longue durée d'exposition. Un laser bleu (404 nm) a été utilisé comme faisceau d'excitation et focalisé sur la surface du guide d'ondes. Une fibre en queue de cochon a été connectée directement à notre spectromètre à réseau refroidi (PI Acton SP2300), comme le montre la **Figure 5-20**(a). L'échantillon IEW a été déplacé dans les directions *x* et *y* (20×20 μm^2, 5 min par balayage) par les étages piézoélectriques situés en dessous. Nous avons pigé nos IEW avec des fibres de maintien de la polarisation (PM-panda, SM-630), comme le montre la **Figure 5-20**(b), qui a été réalisée à Teem Photonics par Muhammad Ahmed. La **Figure 5-20**(c) montre les spectres PL mesurés à partir des positions dans la zone de balayage avant et après l'illumination laser. L'intensité du PL diminue de moitié après un seul balayage (environ 5 minutes). Pour des temps de balayage plus longs, l'intensité du PL diminue lentement. Une intensité PL plus faible a pu être obtenue après un balayage plus long de l'échantillon (10 min et 15 min qui ont également été tracés en rouge et vert sur la **Figure 5-20**(c).

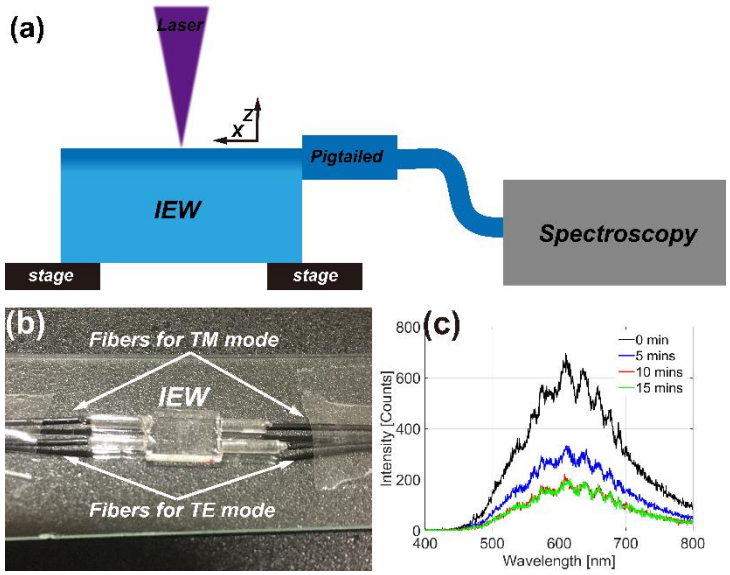

Figure 5-20 (a) IEW avec fibres PM; (b) Schéma du dispositif de mesure; (c) Spectres mesurés avant et après le balayage laser.

5.4.2 Dépôt de la couche de SiC sur les IEW comme alternative au TiO_2

Le carbure de silicium (SiC) est un autre matériau ayant un indice de réfraction élevé et pourrait être un autre bon candidat pour obtenir une plus grande efficacité de couplage [152]. Dans cette sous-section, nous présentons les premiers résultats des mesures PL pour les émissions des QDs des IEWs couverts par la couche de SiC.

Microscopie confocale à balayage laser (CLSM) pour les mesures de PL:

Nous avons développé notre système de mesure PL couplé à une puce à fibre optique qui possède deux canaux de détection afin de détecter l'émission des QDs à l'extrémité supérieure du champ lointain et de l'IEW. Le schéma du dispositif de mesure est présenté à la **Figure 5-21**. L'échantillon a été monté sur un étage piézoélectrique et le laser d'excitation a été modulé temporellement par un modulateur acousto-optique. L'échantillon et la fibre couplée en bout ont été fixés sur une platine piézoélectrique x-y, ce qui a permis de réaliser le balayage de l'échantillon et d'obtenir les images PL. Ici, deux photodiodes d'avalanche (APD) ont été réglées pour enregistrer l'émission qui a été mesurée depuis le haut (champ lointain) et depuis le côté de l'IEW indépendamment

pour convertir les signaux lumineux en signaux AC. Après que les signaux aient été traités et extraits à l'aide d'un amplificateur à verrouillage, les signaux provenant uniquement des émissions des QDs détectées ont ensuite été envoyés au système informatique et convertis en images PL.

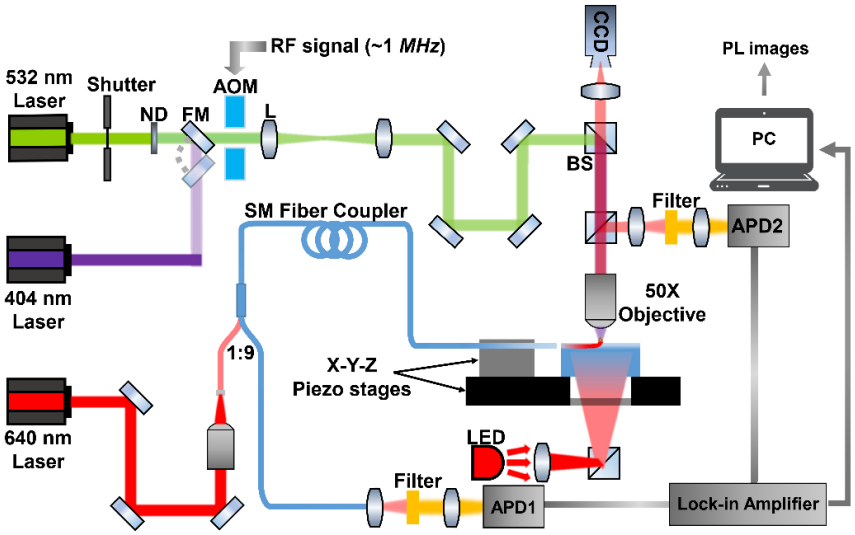

Figure 5-21 installation de mesure d'images PL à balayage laser avec un laser à excitation modulée.

Détection de l'émission des QDs de la couche de SiC couverte par les IEWs:

La **Figure 5-22**(a) montre la couche de SiC de 50 nm déposée sur un échantillon d'IEW, et nous avons fabriqué des lignes de QD-polymère près du bord de la couche de SiC et à travers les IEW. Un laser CW de 640 nm a été couplé à l'IE, et il est évident qu'il y a plus de lumière diffusée depuis la partie droite recouverte de SiC que depuis la partie gauche sans couche de SiC. Cela signifie que plus la lumière se propageant dans l'IEW a été convertie en couche de SiC, comme le montre la **Figure 5-22**(b).

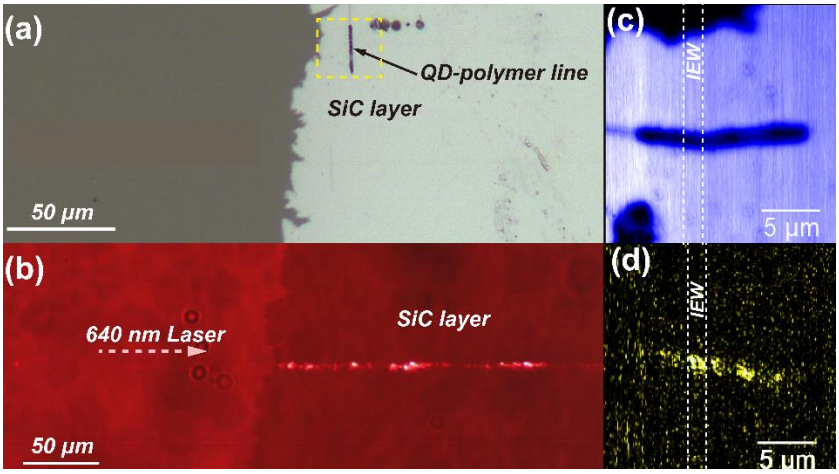

Figure 5-22 (a) Couche de SiC déposée sur la surface de l'IEW; (b) Comparaison de la lumière diffusée par la surface de l'IEW et la couche de SiC. (c) Détection d'un laser d'excitation réfléchi par l'échantillon; (d) Détection de l'émission des QDs couplés à des IEW à partir de la raie de QD-polymère.

En balayant l'échantillon dans le plan x-y avec les étages piézo, nous avons effectué la mesure PL pour la ligne de QD-polymère. La **Figure 5-22**(c) montre les images enregistrées correspondantes de la réflexion laser. Les lignes pointillées blanches représentent les contours des IEW croisés. L'indice de réfraction de la couche de SiC est beaucoup plus élevé que celui du polymère et du verre, de sorte que la réflexion laser de la couche de SiC est également plus élevée, ce qui donne une zone très lumineuse. Le résultat le plus important est le signal de l'émission des QDs couplés à un guide d'ondes, comme le montre la **Figure 5-22**(d). Bien que le signal détecté soit faible, nous sommes encore en mesure d'obtenir l'image PL qui montre que le signal de la position de l'IEW est beaucoup plus élevé que celui de la zone en dehors de l'IEW. C'est la preuve que l'émission des QDs a été couplée à la partie inférieure de l'IEW et se propage le long de l'IEW. Nous mentionnons qu'il s'agit du résultat de mesure préliminaire, il reste encore un long travail à faire pour optimiser les conditions de couplage et améliorer les détections.

5.4.3 Structures photopolymérisées attachées avec des QDs fonctionnalisés

Dans le cadre de notre autre projet, nous travaillons actuellement sur une autre façon de combiner les points quantiques avec le polymère, c'est-à-dire en fonctionnalisant et en modifiant les propriétés chimiques de la surface des points quantiques afin qu'ils s'attachent au polymère plutôt que d'être à l'intérieur de celui-ci. Pour notre besoin spécifique, nous avons fabriqué diverses structures polymères telles que des carrés, des lignes et des points qui ont ensuite été greffés avec des QDs fonctionnalisés sur nos IEW, comme le montre la **Figure 5-23**(a-c). Sous l'éclairage d'une LED bleue (450 nm), une émission significative des QDs de ces structures a pu être observée. La grande surface du carré de polymère et la grande quantité des QDs dans le carré nous permettent de mesurer le spectre PL moyen, comme le montre la **Figure 5-23**(d). Les pics à environ 450 nm et 590 nm représentent respectivement l'excitation de la LED bleue et l'émission des QDs. Nous avons également effectué la mesure PL (le dispositif de mesure a été décrit au chapitre 3) pour l'émission des QDs couplée à un guide d'ondes. Comme indiqué dans la **Figure 5-23**(e) pour une raie de QD-polymère, un faible pic est apparu à 590 nm, ce qui montre la preuve de l'émission des QDs couplée à un guide d'onde.

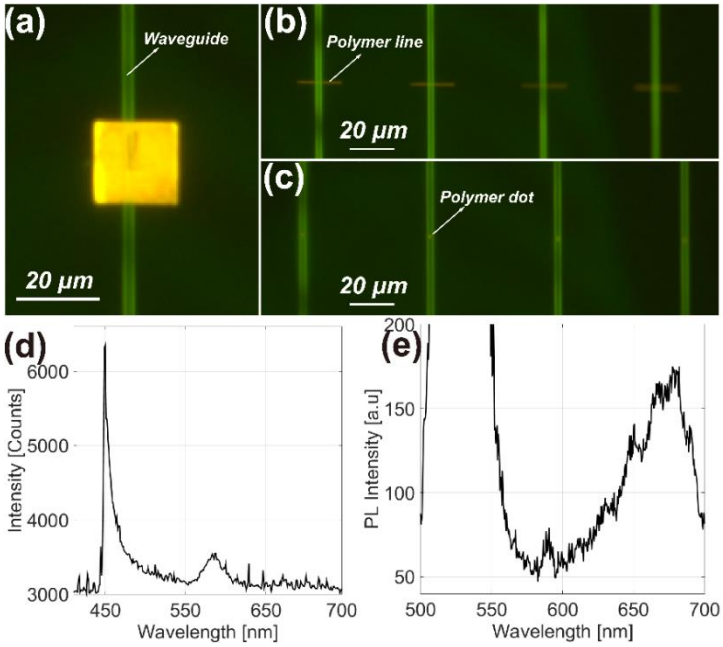

Figure 5-23 Structures polymérisées attachées par des points quantiques fonctionnalisés. (a) Carrés. (b) Lignes. (c) Points; (d) Spectre PL mesuré en champ lointain pour le carré; (e) Spectre PL mesuré couplé à un guide d'onde pour une raie typique de polymère.

5.5 Conclusion générale

La méthode d'intégration basée sur la photopolymérisation offre un moyen simple de créer des nanoémetteurs sur des substrats photoniques dont les positions sont hautement contrôlées. Les nanoémetteurs photopolymérisés peuvent être intégrés sur la puce photonique préfabriquée/présélectionnée et fonctionnent comme des sources de lumière non classiques pour les dispositifs quantiques, et il est prévu de les appliquer à des dispositifs photoniques plus commerciaux.

Nous avons d'abord passé en revue la principale méthode d'intégration pour la mise en caisse des nanoémetteurs sur différents dispositifs photoniques. Cependant, le processus de fabrication compliqué et long de ces méthodes limite leurs applications. Le concept des nanoémetteurs basé sur des nanostructures polymères contenant des QDs est proposé, qui est créé par la réaction de photopolymérisation. Deux exemples (réalisés simultanément à mes travaux de doctorat) de nanoémetteurs polymérisés à

base de plasmon couplés respectivement à des nanofils d'argent et des nanocubes d'or montrent la faisabilité de cette méthode pour son application aux nanosystèmes plasmoniques hybrides. Dans le cadre de ce travail de doctorat, nous avons montré les avantages des guides d'ondes optiques à échange d'ions (IEWs) en verre et nous présentons l'objectif de cette thèse qui est de réaliser des nanoémetteurs intégrés sur les substrats optiques à base d'IEW en verre par un processus de photopolymérisation.

Nous avons ensuite procédé à la photopolymérisation induite par un laser vert couplé à une IEW. Nous avons analysé le problème de l'instabilité de la puissance de sortie du laser des IEWs et avons constaté que la longueur de la pointe de la fibre aérienne, les types de fibres et la propagation de la lumière des IEWs sont les trois principaux paramètres pouvant affecter la stabilité de la plate-forme expérimentale. L'instabilité de la puissance de sortie a été réduite de 15 fois après l'optimisation du dispositif d'expérimentation. Des arêtes en polymère avec et sans points quantiques ont été fabriquées et caractérisées, les résultats montrent la capacité de contrôler leurs dimensions en ajustant la puissance du laser d'excitation et le temps d'exposition. Une couche de TiO_2 a été déposée sur la surface des IEWs pour obtenir la chaîne de crêtes de QD-polymère, qui est causée par le comportement de battement des modes de propagation des IEW et de la couche de TiO_2.

Afin de fabriquer les nanocomposites de QD-polymère sur le substrat des IEWs, nous avons développé la plateforme d'écriture laser directe basée sur le TPP avec une configuration "sandwich". En optimisant le processus de nettoyage après la photopolymérisation, la quantité de points quantiques restant en dehors des voxels de QD-polymère diminue de 43%. Nous avons démontré qu'en ajustant la puissance du laser d'impression et le temps d'exposition, le volume des voxels de QD-polymère imprimés peut être contrôlé à l'échelle nanométrique, ce qui entraîne une différence dans les quantités des QDs à l'intérieur de ces voxels, qui sont vérifiées par les résultats des mesures PL. En outre, en ajustant la hauteur focale du laser d'impression, la taille typique du voxel pourrait être réduite à 17 nm de hauteur et 125 nm de diamètre, ce qui

ne contient probablement que 4-5 QDs selon nos calculs et la couche unique de QD fabriquée.

Plus important encore, nous avons réussi à fabriquer un seul voxel de QD-polymère directement sur un IEW grâce à la plate-forme DLW-TPP développée. Une émission significative en champ lointain a pu être observée et le spectre PL montre que l'émission provient des QDs à l'intérieur du voxel. De plus, nous avons démontré l'émission des QDs couplés à l'IEW en détectant à l'extrémité d'un guide d'onde couplé à une fibre malgré le faible signal de détection. L'écart du spectre PL entre le lointain et le couplé à l'IEW s'explique par les dissimilitudes des conditions de mesure PL, ce qui a été prouvé par nos résultats simulés.

D'autres expériences ont été menées en vue de développements futurs concernant l'intégration des émetteurs de noms dans les structures basées sur les IEW. En éclairant les IEW plus longtemps, nous sommes en mesure de réduire l'émission des IEW eux-mêmes, ce qui permet d'identifier l'émission des QDs pour les nanocomposites de QD-polymère plus petits. Nous avons également démontré que le dépôt d'une couche de SiC sur la surface des IEW peut favoriser le couplage de la lumière entre les IEW et les nanocomposites de QD-polymère grâce aux images PL balayées par laser. Nous avons démontré les propriétés d'émission de lumière, y compris l'émission en champ lointain et l'émission couplée aux IEW, pour les nanostructures polymères avec des QD attachés. Enfin, nous avons également réalisé la première intégration de composites QD-polymère près des structures plasmoniques en nœud papillon par la plateforme DLW-TPP.

Il reste encore beaucoup de travail à faire pour atteindre notre objectif final, qui est la réalisation de nano-émetteurs intégrés sur des structures photoniques complexes basées sur des IEW. De nombreuses questions telles que l'efficacité du couplage entre les QDs et les IEW, le processus d'impression laser et le contrôle PL doivent être explorées. Les résultats présentés dans ce travail fournissent en fait une expérience expérimentale primaire pour nos travaux futurs, et alimentent également une référence

solide pour d'autres recherches dans les domaines de l'optique guidée, des réactions de photopolymérisation, des techniques d'impression laser 3D et des mesures de photoluminescence.

Bibliography

1. J.-C. Weeber, K. Hammani, G. Colas-des-Francs, A. Bouhelier, J. Arocas, A. Kumar, F. Eloi, S. Buil, X. Quélin, and J.-P. Hermier, "Colloidal quantum dot integrated light sources for plasmon mediated photonic waveguide excitation," ACS Photonics **3**, 844–852 (2016).
2. H. Siampour, S. Kumar, and S. I. Bozhevolnyi, "Chip-integrated plasmonic cavity-enhanced single nitrogen-vacancy center emission," Nanoscale **9**, 17902–17908 (2017).
3. H. Siampour, S. Kumar, and S. I. Bozhevolnyi, "Nanofabrication of plasmonic circuits containing single photon sources," Acs Photonics **4**, 1879–1884 (2017).
4. C. Pin, S. Ishida, G. Takahashi, K. Sudo, T. Fukaminato, and K. Sasaki, "Trapping and Deposition of Dye–Molecule Nanoparticles in the Nanogap of a Plasmonic Antenna," ACS omega **3**, 4878–4883 (2018).
5. I.-C. Huang, R. Jensen, O. Chen, J. Choy, T. Bischof, M. Bawendi, and M. Loncar, "Optical trapping of a colloidal quantum dot," in *CLEO: QELS_Fundamental Science* (Optical Society of America, 2015), pp. FF2C-5.
6. O. Bitton, S. N. Gupta, and G. Haran, "Quantum dot plasmonics: from weak to strong coupling," Nanophotonics **8**, 559–575 (2019).
7. P. Zhang, G. Song, and L. Yu, "Optical trapping of single quantum dots for cavity quantum electrodynamics," Photonics Res. **6**, 182–185 (2018).
8. Y. Cui, M. T. Björk, J. A. Liddle, C. Sönnichsen, B. Boussert, and A. P. Alivisatos, "Integration of colloidal nanocrystals into lithographically patterned devices," Nano Lett. **4**, 1093–1098 (2004).
9. M. J. Gordon and D. Peyrade, "Separation of colloidal nanoparticles using capillary immersion forces," Appl. Phys. Lett. **89**, 53112 (2006).

10. Y. Xia, Y. Yin, Y. Lu, and J. McLellan, "Template-assisted self-assembly of spherical colloids into complex and controllable structures," Adv. Funct. Mater. **13**, 907–918 (2003).
11. K. Santhosh, O. Bitton, L. Chuntonov, and G. Haran, "Vacuum Rabi splitting in a plasmonic cavity at the single quantum emitter limit," Nat. Commun. **7**, ncomms11823 (2016).
12. P. Schnauber, A. Singh, J. Schall, S. I. Park, J. D. Song, S. Rodt, K. Srinivasan, S. Reitzenstein, and M. Davanco, "Indistinguishable photons from deterministically integrated single quantum dots in heterogeneous GaAs/Si3N4 quantum photonic circuits," Nano Lett. **19**, 7164–7172 (2019).
13. L. Elsinger, R. Gourgues, I. E. Zadeh, J. Maes, A. Guardiani, G. Bulgarini, S. F. Pereira, S. N. Dorenbos, V. Zwiller, and Z. Hens, "Integration of colloidal PbS/CdS quantum dots with plasmonic antennas and superconducting detectors on a silicon nitride photonic platform," Nano Lett. **19**, 5452–5458 (2019).
14. P. Schnauber, J. Schall, S. Bounouar, T. Höhne, S.-I. Park, G.-H. Ryu, T. Heindel, S. Burger, J.-D. Song, and S. Rodt, "Deterministic integration of quantum dots into on-chip multimode interference beamsplitters using in situ electron beam lithography," Nano Lett. **18**, 2336–2342 (2018).
15. D. Yoo, K. L. Gurunatha, H.-K. Choi, D. A. Mohr, C. T. Ertsgaard, R. Gordon, and S.-H. Oh, "Low-power optical trapping of nanoparticles and proteins with resonant coaxial nanoaperture using 10 nm gap," Nano Lett. **18**, 3637–3642 (2018).
16. M. Davanco, J. Liu, L. Sapienza, C.-Z. Zhang, J. V. D. M. Cardoso, V. Verma, R. Mirin, S. W. Nam, L. Liu, and K. Srinivasan, "Heterogeneous integration for on-chip quantum photonic circuits with single quantum dot devices," Nat. Commun. **8**, 889 (2017).

17. I. E. Zadeh, A. W. Elshaari, K. D. Jöns, A. Fognini, D. Dalacu, P. J. Poole, M. E. Reimer, and V. Zwiller, "Deterministic integration of single photon sources in silicon based photonic circuits," Nano Lett. **16**, 2289–2294 (2016).
18. J.-H. Kim, S. Aghaeimeibodi, C. J. K. Richardson, R. P. Leavitt, D. Englund, and E. Waks, "Hybrid integration of solid-state quantum emitters on a silicon photonic chip," Nano Lett. **17**, 7394–7400 (2017).
19. J. Goffard, D. Gérard, P. Miska, A.-L. Baudrion, R. Deturche, and J. Plain, "Plasmonic engineering of spontaneous emission from silicon nanocrystals," Sci. Rep. **3**, 1–7 (2013).
20. G. M. Akselrod, M. C. Weidman, Y. Li, C. Argyropoulos, W. A. Tisdale, and M. H. Mikkelsen, "Efficient nanosecond photoluminescence from infrared PbS quantum dots coupled to plasmonic nanoantennas," Acs Photonics **3**, 1741–1746 (2016).
21. A. A. Lyamkina, K. Schraml, A. Regler, M. Schalk, A. K. Bakarov, A. I. Toropov, S. P. Moshchenko, and M. Kaniber, "Monolithically integrated single quantum dots coupled to bowtie nanoantennas," Opt. Express **24**, 28936–28944 (2016).
22. H. Sugimoto and M. Fujii, "Broadband dielectric–metal hybrid nanoantenna: Silicon nanoparticle on a mirror," ACS Photonics **5**, 1986–1993 (2018).
23. S. Yashima, H. Sugimoto, H. Takashina, and M. Fujii, "Fluorescence enhancement and spectral shaping of silicon quantum dot monolayer by plasmonic gap resonances," J. Phys. Chem. C **120**, 28795–28801 (2016).
24. T. S. Mentzel, D. D. Wanger, N. Ray, B. J. Walker, D. Strasfeld, M. G. Bawendi, and M. A. Kastner, "Nanopatterned electrically conductive films of semiconductor nanocrystals," Nano Lett. **12**, 4404–4408 (2012).
25. W. Xie, R. Gomes, T. Aubert, S. Bisschop, Y. Zhu, Z. Hens, E. Brainis, and D. Van Thourhout, "Nanoscale and single-dot patterning of colloidal quantum dots," Nano Lett. **15**, 7481–7487 (2015).

26. M. S. Alias, Y. Yang, T. K. Ng, I. Dursun, D. Shi, M. I. Saidaminov, D. Priante, O. M. Bakr, and B. S. Ooi, "Enhanced etching, surface damage recovery, and submicron patterning of hybrid perovskites using a chemically gas-assisted focused-ion beam for subwavelength grating photonic applications," J. Phys. Chem. Lett. **7**, 137–142 (2016).
27. B. J. Black and S. K. Mohanty, "Fiber-optic spanner," Opt. Lett. **37**, 5030–5032 (2012).
28. T. Junno, K. Deppert, L. Montelius, and L. Samuelson, "Controlled manipulation of nanoparticles with an atomic force microscope," Appl. Phys. Lett. **66**, 3627–3629 (1995).
29. Y. Tanaka and K. Sasaki, "Selection and transfer of individual plasmon-resonant metal nanoparticles," Appl. Phys. Lett. **96**, 53117 (2010).
30. A. W. Schell, G. Kewes, T. Schröder, J. Wolters, T. Aichele, and O. Benson, "A scanning probe-based pick-and-place procedure for assembly of integrated quantum optical hybrid devices," Rev. Sci. Instrum. **82**, 73709 (2011).
31. B. H. Kim, M. S. Onses, J. Bin Lim, S. Nam, N. Oh, H. Kim, K. J. Yu, J. W. Lee, J.-H. Kim, and S.-K. Kang, "High-resolution patterns of quantum dots formed by electrohydrodynamic jet printing for light-emitting diodes," Nano Lett. **15**, 969–973 (2015).
32. S. J. P. Kress, P. Richner, S. V Jayanti, P. Galliker, D. K. Kim, D. Poulikakos, and D. J. Norris, "Near-field light design with colloidal quantum dots for photonics and plasmonics," Nano Lett. **14**, 5827–5833 (2014).
33. P. Richner, P. Galliker, T. Lendenmann, S. J. P. Kress, D. K. Kim, D. J. Norris, and D. Poulikakos, "Full-spectrum flexible color printing at the diffraction limit," ACS Photonics **3**, 754–757 (2016).
34. L. Lan, J. Zou, C. Jiang, B. Liu, L. Wang, and J. Peng, "Inkjet printing for electroluminescent devices: emissive materials, film formation, and display prototypes," Front. Optoelectron. **10**, 329–352 (2017).

35. R. Suntivich, I. Drachuk, R. Calabrese, D. L. Kaplan, and V. V Tsukruk, "Inkjet printing of silk nest arrays for cell hosting," Biomacromolecules **15**, 1428–1435 (2014).

36. S. J. P. Kress, F. V Antolinez, P. Richner, S. V Jayanti, D. K. Kim, F. Prins, A. Riedinger, M. P. C. Fischer, S. Meyer, and K. M. McPeak, "Wedge waveguides and resonators for quantum plasmonics," Nano Lett. **15**, 6267–6275 (2015).

37. R. Pandey, "Photopolymers in 3D printing applications Supervisor (Arcada): Mirja Andersson," 27–28 (2014).

38. J. V Crivello and E. Reichmanis, "Photopolymer materials and processes for advanced technologies," Chem. Mater. **26**, 533–548 (2013).

39. X. Zhou, J. Wenger, F. N. Viscomi, L. Le Cunff, J. Béal, S. Kochtcheev, X. Yang, G. P. Wiederrecht, G. Colas des Francs, and A. S. Bisht, "Two-Color Single Hybrid Plasmonic Nanoemitters with Real Time Switchable Dominant Emission Wavelength," Nano Lett. **15**, 7458–7466 (2015).

40. W. K. Bae, J. Kwak, J. Lim, D. Lee, M. K. Nam, K. Char, C. Lee, and S. Lee, "Multicolored light-emitting diodes based on all-quantum-dot multilayer films using layer-by-layer assembly method," Nano Lett. **10**, 2368–2373 (2010).

41. K. D. Sattler, *Handbook of Nanophysics: Principles and Methods* (CRC press, 2010).

42. J. Lalevée and J.-P. Fouassier, *Photopolymerisation Initiating Systems* (Royal Society of Chemistry, 2018), Vol. 29.

43. J. Moughames, S. Jradi, T. M. Chan, S. Akil, Y. Battie, A. E. Naciri, Z. Herro, S. Guenneau, S. Enoch, and L. Joly, "Wavelength-scale light concentrator made by direct 3D laser writing of polymer metamaterials," Sci. Rep. **6**, 33627 (2016).

44. M. V Kovalenko, L. Manna, A. Cabot, Z. Hens, D. V Talapin, C. R. Kagan, V. I. Klimov, A. L. Rogach, P. Reiss, and D. J. Milliron, "Prospects of nanoscience with nanocrystals," (2015).

45. I. S. Alvarez, "Active photonic devices based on colloidal semiconductor nanocrystals and organometallic halide perovskites," Eur. Phys. J. Appl. Phys. **75**, 30001 (2016).

46. R. Abargues, K. Abderrafi, E. Pedrueza, R. Gradess, J. Marqués-Hueso, J. L. Valdés, and J. Martínez-Pastor, "Optical properties of different polymer thin films containing in situ synthesized Ag and Au nanoparticles," New J. Chem. **33**, 1720–1725 (2009).

47. M. A. Reilly, C. Marinelli, C. N. Morgan, R. V Penty, I. H. White, M. Ramon, M. Ariu, R. Xia, and D. D. C. Bradley, "Rib waveguide dye-doped polymer amplifier with up to 26 dB optical gain at 625 nm," Appl. Phys. Lett. **85**, 5137–5139 (2004).

48. D. Amarasinghe, A. Ruseckas, G. A. Turnbull, and I. D. W. Samuel, "Organic semiconductor optical amplifiers," Proc. IEEE **97**, 1637–1650 (2009).

49. I. J. Kramer and E. H. Sargent, "Colloidal quantum dot photovoltaics: a path forward," ACS Nano **5**, 8506–8514 (2011).

50. R. Gradess, R. Abargues, A. Habbou, J. Canet-Ferrer, E. Pedrueza, A. Russell, J. L. Valdés, and J. P. Martínez-Pastor, "Localized surface plasmon resonance sensor based on Ag-PVA nanocomposite thin films," J. Mater. Chem. **19**, 9233–9240 (2009).

51. I. De Leon and P. Berini, "Amplification of long-range surface plasmons by a dipolar gain medium," Nat. Photonics **4**, 382 (2010).

52. A. H. Ip, S. M. Thon, S. Hoogland, O. Voznyy, D. Zhitomirsky, R. Debnath, L. Levina, L. R. Rollny, G. H. Carey, and A. Fischer, "Hybrid passivated colloidal quantum dot solids," Nat. Nanotechnol. **7**, 577 (2012).

53. B. S. Mashford, M. Stevenson, Z. Popovic, C. Hamilton, Z. Zhou, C. Breen, J. Steckel, V. Bulovic, M. Bawendi, and S. Coe-Sullivan, "High-efficiency quantum-dot light-emitting devices with enhanced charge injection," Nat. Photonics **7**, 407 (2013).

54. J. Rodriguez-Viejo, K. F. Jensen, H. Mattoussi, J. Michel, B. O. Dabbousi, and M. G. Bawendi, "Cathodoluminescence and photoluminescence of highly luminescent CdSe/ZnS quantum dot composites," Appl. Phys. Lett. **70**, 2132–2134 (1997).

55. N. Tomczak, D. Jańczewski, M. Han, and G. J. Vancso, "Designer polymer–quantum dot architectures," Prog. Polym. Sci. **34**, 393–430 (2009).

56. M. J. Smith, C. H. Lin, S. Yu, and V. V Tsukruk, "Composite Structures with Emissive Quantum Dots for Light Enhancement," Adv. Opt. Mater. 1801072 (2018).

57. J. Z. Manapat, Q. Chen, P. Ye, and R. C. Advincula, "3D printing of polymer nanocomposites via stereolithography," Macromol. Mater. Eng. **302**, 1600553 (2017).

58. S. Maruo, O. Nakamura, and S. Kawata, "Three-dimensional microfabrication with two-photon-absorbed photopolymerization," Opt. Lett. **22**, 132–134 (1997).

59. H. C. Ishikawa-Ankerhold, R. Ankerhold, and G. P. C. Drummen, "Advanced fluorescence microscopy techniques-FRAP, FLIP, FLAP, FRET and FLIM," Molecules **17**, 4047–4132 (2012).

60. A. Broussier, A. Issa, L. O. Le Cunff, T. H. Nguyen, X. Q. Dinh, S. Blaize, J. Plain, S. Jradi, C. Couteau, and R. Bachelot, "Hybrid plasmonic nanosystem with controlled position of nanoemitters," Appl. Phys. Lett. **114**, 163106 (2019).

61. D. Ge, S. Marguet, A. Issa, S. Jradi, T. H. Nguyen, M. Nahra, J. Béal, R. Deturche, H. Chen, and S. Blaize, J. Plain, C. Fiorini, L. Douillard, O. Soppera, X. Q. Dinh, C. Dang, X. Yang, T. Xu, B. Wei, XW. Sun, C. Couteau, R. Bachelot, "Hybrid plasmonic nano-emitters with controlled single quantum emitter positioning on the local excitation field," Nat. Commun. **11**, 1–11 (2020).

62. D. Bouchet, E. Lhuillier, S. Ithurria, A. Gulinatti, I. Rech, R. Carminati, Y. De Wilde, and V. Krachmalnicoff, "Correlated blinking of fluorescent emitters mediated by single plasmons," Phys. Rev. A **95**, 33828 (2017).

63. V. N. Pustovit, A. M. Urbas, and T. V Shahbazyan, "Energy transfer in plasmonic systems," J. Opt. **16**, 114015 (2014).

64. D. Andrews, G. Scholes, and G. Wiederrecht, *Comprehensive Nanoscience and Technology* (Academic Press, 2010).

65. H. Wei and H. Xu, "Nanowire-based plasmonic waveguides and devices for integrated nanophotonic circuits," Nanophotonics **1**, 155–169 (2012).

66. M. Song, J. Dellinger, O. Demichel, M. Buret, G. C. Des Francs, D. Zhang, E. Dujardin, and A. Bouhelier, "Selective excitation of surface plasmon modes propagating in Ag nanowires," Opt. Express **25**, 9138–9149 (2017).

67. M. Pfeiffer, K. Lindfors, C. Wolpert, P. Atkinson, M. Benyoucef, A. Rastelli, O. G. Schmidt, H. Giessen, and M. Lippitz, "Enhancing the optical excitation efficiency of a single self-assembled quantum dot with a plasmonic nanoantenna," Nano Lett. **10**, 4555–4558 (2010).

68. J. Bellessa, C. Bonnand, J. C. Plenet, and J. Mugnier, "Strong coupling between surface plasmons and excitons in an organic semiconductor," Phys. Rev. Lett. **93**, 36404 (2004).

69. L. Qiang, W. Hong, and X. Hong-Xing, "Remote excitation and remote detection of a single quantum dot using propagating surface plasmons on silver nanowire," Chinese Phys. B **23**, 97302 (2014).

70. A. V Akimov, A. Mukherjee, C. L. Yu, D. E. Chang, A. S. Zibrov, P. R. Hemmer, H. Park, and M. D. Lukin, "Generation of single optical plasmons in metallic nanowires coupled to quantum dots," Nature **450**, 402–406 (2007).

71. G. Lamri, A. Movsesyan, E. Figueiras, J. B. Nieder, J. Aubard, P.-M. Adam, C. Couteau, N. Felidj, and A.-L. Baudrion, "Photochromic control of a plasmon–quantum dots coupled system," Nanoscale **11**, 258–265 (2019).

72. H. Ditlbacher, A. Hohenau, D. Wagner, U. Kreibig, M. Rogers, F. Hofer, F. R. Aussenegg, and J. R. Krenn, "Silver nanowires as surface plasmon resonators," Phys. Rev. Lett. **95**, 257403 (2005).

73. M. T. Hill and M. C. Gather, "Advances in small lasers," Nat. Photonics **8**, 908–918 (2014).

74. G. M. Akselrod, C. Argyropoulos, T. B. Hoang, C. Ciracì, C. Fang, J. Huang, D. R. Smith, and M. H. Mikkelsen, "Probing the mechanisms of large Purcell enhancement in plasmonic nanoantennas," Nat. Photonics **8**, 835–840 (2014).

75. E. Cohen-Hoshen, G. W. Bryant, I. Pinkas, J. Sperling, and I. Bar-Joseph, "Exciton–plasmon interactions in quantum dot–gold nanoparticle structures," Nano Lett. **12**, 4260–4264 (2012).

76. R. Bardhan, N. K. Grady, J. R. Cole, A. Joshi, and N. J. Halas, "Fluorescence enhancement by Au nanostructures: nanoshells and nanorods," ACS Nano **3**, 744–752 (2009).

77. T. V Shubina, A. A. Toropov, V. N. Jmerik, D. I. Kuritsyn, L. V Gavrilenko, Z. F. Krasil'nik, T. Araki, Y. Nanishi, B. Gil, and A. O. Govorov, "Plasmon-induced Purcell effect in InN/In metal-semiconductor nanocomposites," Phys. Rev. B **82**, 73304 (2010).

78. E. M. Purcell, "Spontaneous emission probabilities at radio frequencies," in *Confined Electrons and Photons* (Springer, 1995), p. 839.

79. R. Carminati, A. Cazé, D. Cao, F. Peragut, V. Krachmalnicoff, R. Pierrat, and Y. De Wilde, "Electromagnetic density of states in complex plasmonic systems," Surf. Sci. Rep. **70**, 1–41 (2015).

80. A. F. Koenderink, "On the use of Purcell factors for plasmon antennas," Opt. Lett. **35**, 4208–4210 (2010).

81. J. Barthes, G. C. Des Francs, A. Bouhelier, J.-C. Weeber, and A. Dereux, "Purcell factor for a point-like dipolar emitter coupled to a two-dimensional plasmonic waveguide," Phys. Rev. B **84**, 73403 (2011).

82. C. Deeb, C. Ecoffet, R. Bachelot, J. Plain, A. Bouhelier, and O. Soppera, "Plasmon-based free-radical photopolymerization: effect of diffusion on nanolithography processes," J. Am. Chem. Soc. **133**, 10535–10542 (2011).

83. C. Deeb, R. Bachelot, J. Plain, A.-L. Baudrion, S. Jradi, A. Bouhelier, O. Soppera, P. K. Jain, L. Huang, and C. Ecoffet, "Quantitative analysis of localized surface plasmons based on molecular probing," ACS Nano **4**, 4579–4586 (2010).

84. H. I. El Ahrach, R. Bachelot, A. Vial, G. Lerondel, J. Plain, P. Royer, and O. Soppera, "Spectral degeneracy breaking of the plasmon resonance of single metal nanoparticles by nanoscale near-field photopolymerization," Phys. Rev. Lett. **98**, 107402 (2007).

85. C. Gruber, A. Hirzer, V. Schmidt, A. Trügler, U. Hohenester, H. Ditlbacher, A. Hohenau, and J. R. Krenn, "Imaging nanowire plasmon modes with two-photon polymerization," Appl. Phys. Lett. **106**, 81101 (2015).

86. K. Ueno, S. Juodkazis, T. Shibuya, Y. Yokota, V. Mizeikis, K. Sasaki, and H. Misawa, "Nanoparticle plasmon-assisted two-photon polymerization induced by incoherent excitation source," J. Am. Chem. Soc. **130**, 6928–6929 (2008).

87. C. Deeb, X. Zhou, J. Plain, G. P. Wiederrecht, R. Bachelot, M. Russell, and P. K. Jain, "Size dependence of the plasmonic near-field measured via single-nanoparticle photoimaging," J. Phys. Chem. C **117**, 10669–10676 (2013).

88. T. Roger, S. Vezzoli, E. Bolduc, J. Valente, J. J. F. Heitz, J. Jeffers, C. Soci, J. Leach, C. Couteau, and N. I. Zheludev, "Coherent perfect absorption in deeply subwavelength films in the single-photon regime," Nat. Commun. **6**, 1–5 (2015).

89. E. Jordan, F. Geoffray, A. Bouchard, E. Ghibaudo, and J.-E. Broquin, "Development of Tl+/Na+ ion-exchanged single-mode waveguides on silicate glass for visible-blue wavelengths applications," Ceram. Int. **41**, 7996–8001 (2015).

90. J. Martínez, A. Ródenas, A. Stake, M. Traveria, M. Aguiló, J. Solis, R. Osellame, T. Tanaka, B. Berton, and S. Kimura, "Harsh-Environment-Resistant OH-Vibrations-Sensitive Mid-Infrared Water-Ice Photonic Sensor," Adv. Mater. Technol. **2**, 1700085 (2017).

91. Y. Luo, M. Chamanzar, A. Apuzzo, R. Salas-Montiel, K. N. Nguyen, S. Blaize, and A. Adibi, "On-chip hybrid photonic–plasmonic light concentrator for nanofocusing in an integrated silicon photonics platform," Nano Lett. **15**, 849–856 (2015).

92. J. Beltran Madrigal, "Integration of a single photon source on a planar dielectric waveguide," (2017).

93. R. Freeman and I. Willner, "Optical molecular sensing with semiconductor quantum dots (QDs)," Chem. Soc. Rev. **41**, 4067–4085 (2012).

94. D. V Talapin, J.-S. Lee, M. V Kovalenko, and E. V Shevchenko, "Prospects of colloidal nanocrystals for electronic and optoelectronic applications," Chem. Rev. **110**, 389–458 (2010).

95. M. B. Wilker, K. J. Schnitzenbaumer, and G. Dukovic, "Recent progress in photocatalysis mediated by colloidal ii-vi nanocrystals," Isr. J. Chem. **52**, 1002–1015 (2012).

96. T. Rauch, M. Böberl, S. F. Tedde, J. Fürst, M. V Kovalenko, G. Hesser, U. Lemmer, W. Heiss, and O. Hayden, "Near-infrared imaging with quantum-dot-sensitized organic photodiodes," Nat. Photonics **3**, 332 (2009).

97. B. N. Pal, Y. Ghosh, S. Brovelli, R. Laocharoensuk, V. I. Klimov, J. A. Hollingsworth, and H. Htoon, "'Giant'CdSe/CdS core/shell nanocrystal quantum dots as efficient electroluminescent materials: strong influence of shell thickness on light-emitting diode performance," Nano Lett. **12**, 331–336 (2012).

98. S. Reitzenstein and A. Forchel, "Quantum dot micropillars," J. Phys. D. Appl. Phys. **43**, 33001 (2010).

99. T. Baldacchini, C. N. LaFratta, R. A. Farrer, M. C. Teich, B. E. A. Saleh, M. J. Naughton, and J. T. Fourkas, "Acrylic-based resin with favorable properties for three-dimensional two-photon polymerization," J. Appl. Phys. **95**, 6072–6076 (2004).

100. Z. Liu, C. Guo, J. Yang, and L. Yuan, "Tapered fiber optical tweezers for microscopic particle trapping: fabrication and application," Opt. Express **14**, 12510–12516 (2006).

101. J. Noda, K. Okamoto, and Y. Sasaki, "Polarization-maintaining fibers and their applications," J. Light. Technol. **4**, 1071–1089 (1986).

102. J. J. Cargille, "Immersion oil and the microscope," NY Microsc. Soc., Yearb. **9**, (2008).

103. A. D. Yablon, *Optical Fiber Fusion Splicing* (Springer Science & Business Media, 2005), Vol. 103.

104. T. Kaino, "Optical absorption of polymers Encyclopedia of Polymeric Materials," (2014).

105. M. Schmid, D. Ludescher, and H. Giessen, "Optical properties of photoresists for femtosecond 3D printing: refractive index, extinction, luminescence-dose dependence, aging, heat treatment and comparison between 1-photon and 2-photon exposure," Opt. Mater. Express **9**, 4564–4577 (2019).

106. G. E. Lio, J. B. Madrigal, X. Xu, Y. Peng, S. Pierini, C. Couteau, S. Jradi, R. Bachelot, R. Caputo, and S. Blaize, "Integration of nanoemitters onto photonic structures by guided evanescent-wave nano-photopolymerization," J. Phys. Chem. C **123**, 14669–14676 (2019).

107. C. C. Evans, C. Liu, and J. Suntivich, "Low-loss titanium dioxide waveguides and resonators using a dielectric lift-off fabrication process," Opt. Express **23**, 11160–11169 (2015).

108. M. Häyrinen, M. Roussey, V. Gandhi, P. Stenberg, A. Säynätjoki, L. Karvonen, M. Kuittinen, and S. Honkanen, "Low-loss titanium dioxide strip waveguides fabricated by atomic layer deposition," J. Light. Technol. **32**, 208–212 (2013).

109. S. S. Djordjevic, K. Shang, B. Guan, S. T. S. Cheung, L. Liao, J. Basak, H.-F. Liu, and S. J. B. Yoo, "CMOS-compatible, athermal silicon ring modulators clad with titanium dioxide," Opt. Express **21**, 13958–13968 (2013).

110. W.-P. Huang, "Coupled-mode theory for optical waveguides: an overview," JOSA A **11**, 963–983 (1994).

111. J. D. Jackson, "Classical Electrodynamics 3rd ed John Wiley & Sons," Inc., NewYork, NY (1999).

112. M. L. Povinelli, M. Lončar, M. Ibanescu, E. J. Smythe, S. G. Johnson, F. Capasso, and J. D. Joannopoulos, "Evanescent-wave bonding between optical waveguides," Opt. Lett. **30**, 3042–3044 (2005).

113. M. Z. Alam, J. Meier, J. S. Aitchison, and M. Mojahedi, "Propagation characteristics of hybrid modes supported by metal-low-high index waveguides and bends," Opt. Express **18**, 12971–12979 (2010).

114. R. Halir, P. J. Bock, P. Cheben, A. Ortega-Moñux, C. Alonso-Ramos, J. H. Schmid, J. Lapointe, D. Xu, J. G. Wangüemert-Pérez, and Í. Molina-Fernández, "Waveguide sub-wavelength structures: a review of principles and applications," Laser Photon. Rev. **9**, 25–49 (2015).

115. K. Gut, A. Zakrzewski, and T. Pustelny, "Sensitivity of Polarimetric Waveguide Interferometer for Different Wavelengths.," Acta Phys. Pol. A. **118**, (2010).

116. F. Aloui, L. Lecamp, P. Lebaudy, and F. Burel, "Refractive index evolution of various commercial acrylic resins during photopolymerization.," Express Polym. Lett. **12**, (2018).

117. M. Elie, S. Gaillard, and J. L. Renaud, "Light-Emitting Electrochemical Cells: Concepts, Advances and Challenges; Costa, RD, Ed," (2017).

118. O. V Yaroshchuk and L. O. Dolgov, "Electro-optics and structure of polymer dispersed liquid crystals doped with nanoparticles of inorganic materials," Opt. Mater. (Amst). **29**, 1097–1102 (2007).

119. M. Vahid, T. Fei, S. Dewang, C. Yoonsung, O. Burcu, Y. Kosala, H. Michael, K. Dong-Joo, K. Helen, and K. K. Lee, "Simulation of the refractive index of Ga doped ZnO nanoparticles embedded in PEDOT:PSS using effective medium approximations," J. Nanoence Nanotechnol. **16**, 7358–7362 (2016).

120. W. Geng, "Coupling nanostructures towards integrated nanophotonics devices," (2015).

121. I. Aharonovich, D. Englund, and M. Toth, "Solid-state single-photon emitters," Nat. Photonics **10**, 631–641 (2016).

122. K. Obata, A. El-Tamer, L. Koch, U. Hinze, and B. N. Chichkov, "High-aspect 3D two-photon polymerization structuring with widened objective working range (WOW-2PP)," Light Sci. Appl. **2**, e116 (2013).

123. Y. Peng, S. Jradi, X. Yang, M. Dupont, F. Hamie, X. Q. Dinh, X. W. Sun, T. Xu, and R. Bachelot, "3D Photoluminescent Nanostructures Containing Quantum Dots Fabricated by Two-Photon Polymerization: Influence of Quantum Dots on the Spatial Resolution of Laser Writing," Adv. Mater. Technol. **4**, 1800522 (2019).

124. T. Bückmann, N. Stenger, M. Kadic, J. Kaschke, A. Frölich, T. Kennerknecht, C. Eberl, M. Thiel, and M. Wegener, "Tailored 3D mechanical metamaterials made by dip-in direct-laser-writing optical lithography," Adv. Mater. **24**, 2710–2714 (2012).

125. C. S. Rout, A. Govindaraj, and C. N. R. Rao, "High-sensitivity hydrocarbon sensors based on tungsten oxide nanowires," J. Mater. Chem. **16**, 3936–3941 (2006).

126. K. Walsh, J. Norville, and Y.-C. Tai, "Photoresist as a sacrificial layer by dissolution in acetone," in *Technical Digest. MEMS 2001. 14th IEEE International Conference on Micro Electro Mechanical Systems (Cat. No. 01CH37090)* (IEEE, 2001), pp. 114–117.

127. A. K. Doolittle, "technology of solvents and plasticizers," (1954).

128. Q. Li, B. Chen, and B. Xing, "Aggregation kinetics and self-assembly mechanisms of graphene quantum dots in aqueous solutions: cooperative effects of pH and electrolytes," Environ. Sci. Technol. **51**, 1364–1376 (2017).

129. H.-B. Sun and S. Kawata, "Two-photon photopolymerization and 3D lithographic microfabrication," in *NMR• 3D Analysis• Photopolymerization* (Springer, 2004), pp. 169–273.

130. H.-B. Sun, M. Maeda, K. Takada, J. W. M. Chon, M. Gu, and S. Kawata, "Experimental investigation of single voxels for laser nanofabrication via two-photon photopolymerization," Appl. Phys. Lett. **83**, 819–821 (2003).

131. X. Zhou, Y. Hou, and J. Lin, "A review on the processing accuracy of two-photon polymerization," AIP Adv. **5**, 30701 (2015).

132. B. Poon, D. Rittel, and G. Ravichandran, "An analysis of nanoindentation in linearly elastic solids," Int. J. Solids Struct. **45**, 6018–6033 (2008).

133. T. Guélon, J.-D. Mathias, and P. Stoodley, "Advances in biofilm mechanics," in *Biofilm Highlights* (Springer, 2011), pp. 111–139.

134. P. Prabhakaran, W. J. Kim, K.-S. Lee, and P. N. Prasad, "Quantum dots (QDs) for photonic applications," Opt. Mater. Express **2**, 578–593 (2012).

135. K. Aoki, D. Guimard, M. Nishioka, M. Nomura, S. Iwamoto, and Y. Arakawa, "Coupling of quantum-dot light emission with a three-dimensional photonic-crystal nanocavity," Nat. Photonics **2**, 688 (2008).

136. S. Jun, E. Jang, J. Park, and J. Kim, "Photopatterned semiconductor nanocrystals and their electroluminescence from hybrid light-emitting devices," Langmuir **22**, 2407–2410 (2006).

137. P. O. Anikeeva, J. E. Halpert, M. G. Bawendi, and V. Bulovic, "Quantum dot light-emitting devices with electroluminescence tunable over the entire visible spectrum," Nano Lett. **9**, 2532–2536 (2009).

138. A. W. Snyder and J. Love, *Optical Waveguide Theory* (Springer Science & Business Media, 2012).

139. J. Cui, A. P. Beyler, I. Coropceanu, L. Cleary, T. R. Avila, Y. Chen, J. M. Cordero, S. L. Heathcote, D. K. Harris, and O. Chen, "Evolution of the single-nanocrystal photoluminescence linewidth with size and shell: Implications for

exciton–phonon coupling and the optimization of spectral linewidths," Nano Lett. **16**, 289–296 (2016).

140. W. van der Stam, M. de Graaf, S. Gudjonsdottir, J. J. Geuchies, J. J. Dijkema, N. Kirkwood, W. H. Evers, A. Longo, and A. J. Houtepen, "Tuning and probing the distribution of Cu+ and Cu2+ trap states responsible for broad-band photoluminescence in CuInS2 nanocrystals," ACS Nano **12**, 11244–11253 (2018).
141. P. J. Whitham, A. Marchioro, K. E. Knowles, T. B. Kilburn, P. J. Reid, and D. R. Gamelin, "Single-particle photoluminescence spectra, blinking, and delayed luminescence of colloidal CuInS2 nanocrystals," J. Phys. Chem. C **120**, 17136–17142 (2016).
142. A. J. Fischer, P. D. Anderson, D. D. Koleske, and G. Subramania, "Deterministic placement of quantum-size controlled quantum dots for seamless top-down integration," ACS Photonics **4**, 2165–2170 (2017).
143. J. B. Madrigal, R. Tellez-Limon, F. Gardillou, D. Barbier, W. Geng, C. Couteau, R. Salas-Montiel, and S. Blaize, "Hybrid integrated optical waveguides in glass for enhanced visible photoluminescence of nanoemitters," Appl. Opt. **55**, 10263–10268 (2016).
144. J. N. Farahani, D. W. Pohl, H.-J. Eisler, and B. Hecht, "Single quantum dot coupled to a scanning optical antenna: a tunable superemitter," Phys. Rev. Lett. **95**, 17402 (2005).
145. R. Talebi, "Investigating multicolour photochromic behaviour of AgCl and AgI thin films loaded with silver nanoparticles," Phys. Chem. Chem. Phys. **20**, 5734–5743 (2018).
146. I. A. Demichev, A. I. Sidorov, and N. V Nikonorov, "The influence of the conditions of ion exchange in CuSO 4: Na 2 SO 4 melt on the optical properties of surface layers of silicate glass," Opt. Spectrosc. **119**, 234–237 (2015).

147. M. Koneracká, A. Antošová, V. Závišová, G. Lancz, Z. Gažová, K. Šipošováa, A. Juríková, K. Csach, J. Kováč, and N. Tomašovičová, "Characterization of Fe 3 O 4 Magnetic Nanoparticles Modified with Dextran and Investigation of Their Interaction with Protein Amyloid Aggregates.," Acta Phys. Pol. A. **118**, (2010).

148. P. Anger, P. Bharadwaj, and L. Novotny, "Enhancement and quenching of single-molecule fluorescence," Phys. Rev. Lett. **96**, 113002 (2006).

149. L. Fabbrizzi and A. Poggi, "Sensors and switches from supramolecular chemistry," Chem. Soc. Rev. **24**, 197–202 (1995).

150. A. Han, X. Liu, G. D. Prestwich, and L. Zang, "Fluorescent sensor for Hg2+ detection in aqueous solution," Sensors Actuators B Chem. **198**, 274–277 (2014).

151. N. Pandey, M. S. Mehata, N. Fatma, and S. Pant, "Efficient fluorescence quenching of 5-aminoquinoline: Silver ion recognition study," J. Lumin. **205**, 475–481 (2019).

152. A. O'Neill, O. Vavasour, S. Russell, F. Arith, J. Urresti, and P. Gammon, "Dielectrics in Silicon Carbide Devices: Technology and Application," Adv. Silicon Carbide Electron. Technol. II Core Technol. Silicon Carbide Device Process. **69**, 63 (2020).

List of communications

Journals:

- **Xu X**, A Broussier, T Ritacco, M Nahra, F Geoffray, A Issa, S Jradi, R Bachelot, C Couteau, S Blaize, "Towards the integration of nanoemitters by direct laser writing on optical glass waveguides," *Photonic Research*. 8, 1541-1550 (2020)
- G E Lio, J B Madrigal, **Xu X**, Peng Y, S Pierini, C Couteau, S Jradi, R Bachelot, R Caputo, S Blaize, "Integration of nanoemitters onto photonic structures by guided evanescent-wave nano-photopolymerization," *The Journal of Physical Chemistry C*, 123(23), 14669-14676 (2019)
- T Ritacco, **Xu X**, A Broussier, A Issa, G E Lio, M Giocondo, R Bachelot, S Blaize, C Couteau, and S Jradi, "3D Photo-Luminescent Crypto-Images by One-Photon and Two-Photon Polymerization," (Under submission)
- A Issa, A Broussier, D Ge, **Xu X**, C Couteau, S Blaize, R Bachelot, S Jradi, "Ligand exchange protocol for Quantum Dots dispersion into photopolymer," (Under submission)

International conferences:

- **Xu X**, J B Madrigal, A Broussier, G E Lio, F Geoffray, A Issa, S Jradi, R Bachelot, C Couteau, S Blaize, "Quantum emitters based on polymeric structures embedded with quantum dots fabricated via photo-polymerization." In Advanced Fabrication Technologies for Micro/Nano

Optics and Photonics XIII (Vol. 11292, p. 112920O). International Society for Optics and Photonics. San Francsico, USA, 2020, oral presentation.

- **Xu X**, A Broussier, M Nahra, F Geoffray, A Issa, S Jradi, R Bachelot, C Couteau, S Blaize, "Integration of nanoemitters to optical glass-based waveguides by two photon polymerization." NanoGe Online Meetup conference: Nanocrystals in Additive Manufacturing, 2020, poster presentation.
- **Xu X**, A Issa, A Broussier, H Muhammad, F Geoffray, S Jradi, C Couteau, S Blaize, "Single photon conversion between site-controlled quantum dots and photonic optical waveguides." 10th IQFA'X Colloquium Quantum Engineering, from Fundamental Aspects to Applications, CNRS Headquarters, Paris, France, 2019, poster presentation.
- **Xu X**, T Ritacco, A Broussier, S Pierini, F Geoffray, F Gardillou, G Souhaite, A Issa, S Jradi, R Bachelot, C Couteau, S Blaize, " Integration of Luminescent Nanostructures to Optical Waveguides by Two Photon Polymerization," CLEO/Europe-EQEC, Munich, Germany, 2019, poster presentation.
- **Xu X**, T Ritacco, A Broussier, F Geoffray, G Souhaite, A Issa, S Jradi, R Bachelot, C Couteau, S Blaize, " Positioning of Quantum Dots by Two Photon Polymerization," Workshop Nano-Optics, Nano-Spectroscopy & Nano-Fabrication, Eberhard Karls University Tübingen, Germany, 2019, oral presentation.
- **Xu X**, A Broussier, S Pierini, F Geoffray, F Gardillou, G Souhaité, A Issa, S Jradi, R Bachelot, C Couteau, S Blaize, "Integration of Luminescent Nanostructures to Optical Waveguides by Two Photon Polymerization." 15th International Conference on Near-field Optics, Nanophotonics and related Techniques (NFO-15), Troyes, France, 2018, poster presentation.

Xiaolun XU

Doctorat : Matériaux, Mécanique, Optique, Nanotechnologie

Année 2020

Nanoémetteurs intégrés sur des guides d'ondes en verre par photopolymérisation

Les nano-émetteurs et les nanosources de lumière sont des éléments essentiels pour les dispositifs photoniques. L'une des principales exigences est la capacité d'intégrer des nano-émetteurs sur des emplacements de puces optiques spécifiques. De nombreuses approches ont été explorées pour la réalisation pratique de dispositifs photoniques évolutifs. Cependant, ces méthodes présentent certaines limites, comme des opérations compliquées, des coûts de fabrication élevés et de multiples étapes de fabrication. Cette thèse vise à explorer la faisabilité de l'intégration de nanoémetteurs basés sur des nanocomposites de polymères à points quantiques sur des substrats optiques à base de guides d'ondes en verre à échange d'ions par un processus de photopolymérisation. Nous avons fabriqué les crêtes de polymère à points quantiques de taille contrôlée sur les guides d'ondes en effectuant la photopolymérisation directe induite par le laser vert couplé au guide d'ondes avec une puissance laser et un temps d'exposition contrôlés. Nous avons réussi à fabriquer un nanocomposite de polymère à points quantiques uniques directement sur un guide d'ondes à échange d'ions grâce à la technique d'impression laser développée, basée sur la polymérisation à deux photons. L'émission couplée au guide d'ondes des points quantiques à l'intérieur du nanocomposite a été démontrée par les résultats de nos mesures de photoluminescence. Ce travail fournit une expérience expérimentale primaire pour nos travaux futurs.

Mots clés : optique intégrée – nanophotonique – guides d'ondes optiques – photopolymérisation – photoluminescence.

Integrated Nanoemitters on Glass-based Waveguides by Photopolymerization

Nanoemitters and nanosources of light are crucial elements for photonic devices. one of the key requirements is the ability to integrate nanoemitters onto specific optical chip locations. Many approaches have been explored for the practical realization of scalable photonic devices. However, these methods have some limitations such as complicated operations, high manufacturing costs, and multiple fabricating steps. This thesis aims to explore the feasibility of integrating nanoemitters based on quantum dots-polymer nanocomposites onto glass ion-exchanged waveguides-based optical substrates by photopolymerization process. We fabricated the size-controlled quantum dots-polymer ridges on top of waveguides by conducting the direct photopolymerization induced by the waveguide-coupled green laser with controlled laser power and exposure time. We succeeded in fabricating a single quantum dots-polymer nanocomposite directly on an ion-exchanged-waveguide by the developed laser printing technique based on two photon polymerization. The waveguide-coupled emission from the quantum dots inside the nanocomposite was demonstrated by our photoluminescence measurement results. This work provides primary experimental experience for our future work.

Keywords: integrated optics – nanophotonics – optical wave guides – photopolymerization – photoluminescence.

Thèse réalisée en partenariat entre :